

---

# Mechanochemical Synthesis, Phase Transformation and Surface Functionalization of Metal Oxides

---

## Dissertation

zur Erlangung des Grades des Doktors der Naturwissenschaften  
der Naturwissenschaftlich-Technischen Fakultät  
der Universität des Saarlandes

vorgelegt von

Dennis Becker

Saarbrücken

2020



Tag des Kolloquiums: 21.08.2020

Dekan: Prof. Dr. Guido Kickelbick

Berichterstatter: Prof. Dr. Guido Kickelbick

Priv. Doz. Dr. Guido Falk

Vorsitz: Prof. Dr. Gregor Jung

Akad. Mitarbeiter: Dr. Carsten Präsang



Die vorliegende Arbeit entstand im Zeitraum von März 2016 bis September 2019 an der Universität des Saarlandes im Arbeitskreis *Anorganische Festkörperchemie* unter der Anleitung von Herrn Prof. Dr. Guido Kickelbick.



*“Da steh ich nun, ich armer Tor!  
Und bin so klug als wie zuvor.”*

Faust – Johann Wolfgang von Goethe



# Danksagung

Einen großen Dank möchte ich Prof. Dr. Guido Kickelbick aussprechen, der mir die Möglichkeit gegeben hat diese Arbeit durchzuführen. Vielen Dank für die großen Freiheiten in meinem Thema und die Unterstützung bei wissenschaftlichen Fragestellungen insbesondere bei der Publikation der Ergebnisse in wissenschaftlichen Fachzeitschriften. PD Dr. Guido Falk danke ich für die wissenschaftliche Begleitung dieser Arbeit und seine Bereitschaft ein Zweitgutachten zu erstellen.

Mein besonderer Dank gilt Dr. Robert Haberkorn, der mich bei meiner Arbeit stets tatkräftig sowohl in handwerklichen als auch wissenschaftlichen Fragestellungen unterstützt hat. Insbesondere für die stete Bereitschaft mir im Bereich der Pulverdiffraktion und Rietveldverfeinerung zur Seite zu stehen und mir dort sein Wissen zu vermitteln, aber auch für die vielen nichtwissenschaftlichen und freundschaftlichen Diskussionen und Gespräche möchte ich mich bedanken.

Ich möchte mich bei all meinen langjährigen Kolleginnen und Kollegen im Arbeitskreis bedanken auf deren Unterstützung ich sowohl in wissenschaftlichen als auch handwerklichen und organisatorischen Dingen immer zählen konnte. Danke an Nils, Jessica, Thomas, Achim, Nadja, Sandra, Christina O., Dennis M., Patrick, Bastian, Max, Mana, Michael K., Svenja, Ralf, Kristina, Jonas, Christina H., Susanne L., Susanne H., Christel, Traudel, Sylvia, Stefan und Matthias für die tolle und freundschaftliche Arbeitsatmosphäre und all die Hilfe, der ich in Einzelaufzählungen kaum gerecht werden könnte.

Ich danke meinen Eltern für die immerwährende Unterstützung meinen Weg zu gehen und mir all dies zu ermöglichen.

Vielen Dank Bianca, dass du während all dieser Zeit für mich da warst, mich motiviert hast und mir den nötigen Rückhalt und Ausgleich zu meiner Arbeit gegeben hast.



# Zusammenfassung

Die hochenergetische Kugelmahlung wurde genutzt um Synthesen, Strukturveränderungen und Oberflächenfunktionalisierungen im Bereich anorganischer Oxide durchzuführen. Die Mahlung erlaubt den Erhalt nanokristalliner oder amorpher Materialien, sowie die Bildung von Hochdruck- und Hochtemperaturphasen und Defekten. Die entstehenden Phasen können aufgrund dieser Veränderungen als Materialien für Li-Ionen Batterien interessant sein.

Vermahlungen wurden für die Verbindungen  $\text{Li}_2\text{TiO}_3$ ,  $\text{Li}_4\text{Ti}_5\text{O}_{12}$ ,  $\text{Mn}_3\text{O}_4$  und  $\text{LiMn}_2\text{O}_4$  durchgeführt. Strukturelle Veränderungen konnten mittels XRD und Rietveldanalysen erfasst werden, die für Titanate durch  $^6\text{Li}$  Festkörper-NMR ergänzt wurden. Die Oberflächenfunktionalisierung konnte mittels IR Spektroskopie nachgewiesen werden.  $\alpha\text{-Li}_2\text{TiO}_3$  und  $\text{Mn}_3\text{O}_4$  wurden erstmals mechanochemisch aus monovalenten Oxiden erhalten. Für  $\beta\text{-Li}_2\text{TiO}_3$  und  $\text{Li}_4\text{Ti}_5\text{O}_{12}$  wurde ein mechanisch induzierter Übergang zu einer kubischen Phase beobachtet. Für  $\text{LiMn}_2\text{O}_4$  wurde der Übergang zu einer orthorhombischen und tetragonalen Phase mit Kationenunordnung beobachtet. Der Abbau zu  $\text{Mn}_2\text{O}_3$  und einer unbekannt Phase wurde durch in situ Oberflächenfunktionalisierung mit Phenylphosphonsäure im Mahlprozess verhindert.

Es konnte gezeigt werden, dass die durch Mahlung verursachten Linienverbreiterungen nicht nur durch Kristallitgrößeneffekte bedingt sind. Mehrere Strukturmodelle wurden etabliert mit denen die komplexen Veränderungen der Reflexmuster und Linienbreiten in Rietveldverfeinerungen erfasst werden können.



## Abstract

High energy ball milling was used to induce syntheses, structure changes and surface functionalizations in the field of inorganic oxide materials. Milling facilitates the formation of nanocrystalline or amorphous materials, as well as the formation of high pressure and high temperature phases and defects. Based on these properties, the products may be interesting as materials for Li-ion batteries.

Milling experiments have been conducted using  $\text{Li}_2\text{TiO}_3$ ,  $\text{Li}_4\text{Ti}_5\text{O}_{12}$ ,  $\text{Mn}_3\text{O}_4$  and  $\text{LiMn}_2\text{O}_4$ . Structural changes were determined by XRD and Rietveld analysis. In the case of titanates, the studies were complemented by  $^6\text{Li}$  solid-state NMR spectroscopy. The surface functionalization was proven via IR spectroscopy. For the first time,  $\alpha\text{-Li}_2\text{TiO}_3$  and  $\text{Mn}_3\text{O}_4$  were synthesized by a mechanochemical route from monovalent oxides. In the case of  $\beta\text{-Li}_2\text{TiO}_3$  and  $\text{Li}_4\text{Ti}_5\text{O}_{12}$  a mechanical induced transformation to a cubic phase was observed. In the case of  $\text{LiMn}_2\text{O}_4$  a transformation to an orthorhombic and tetragonal phase with a cation disorder has been observed. The decomposition to  $\text{Mn}_2\text{O}_3$  and an unknown phase was prevented by an in situ surface functionalization with Phenylphosphonic acid in the milling process.

It has been shown that the milling induced line broadening is not only caused by crystallite size effects alone. Multiple structure models have been established to accommodate the complex changes of the reflection patterns and line profiles in the Rietveld refinements.



# Contents

<b>Zusammenfassung</b>	<b>xi</b>
<b>Abstract</b>	<b>xiii</b>
<b>Part I Introduction</b>	<b>1</b>
<b>1 Mechanochemistry</b>	<b>3</b>
1.1 A Brief History . . . . .	3
1.2 Tools for Mechanochemistry . . . . .	4
1.2.1 Mortar and Pestle . . . . .	4
1.2.2 Planetary Ball Mills . . . . .	5
1.3 Theoretical Aspects . . . . .	7
1.4 Applications . . . . .	9
1.4.1 Size Reduction – A Top-Down Approach . . . . .	9
1.4.2 Mechanochemical Syntheses . . . . .	10
1.4.3 Mechanical Induced Phase Transformations . . . . .	11
1.4.4 Mechanochemical Surface Functionalization . . . . .	11
<b>2 Metal Oxides</b>	<b>13</b>
2.1 Lithium Ion Battery Materials . . . . .	13
2.2 Lithium Titanium Oxides . . . . .	15
2.2.1 Structures and Properties . . . . .	15
2.2.2 Synthesis Methods . . . . .	18
2.3 Lithium Manganese Oxides . . . . .	19
2.3.1 Structures and Properties . . . . .	19
2.3.2 Synthesis Methods . . . . .	21
<b>3 Powder X-Ray diffraction</b>	<b>23</b>
3.1 Rietveld Refinement . . . . .	23
3.2 Line Profile Analysis . . . . .	25
3.3 Multi-Fraction Models . . . . .	27
<b>4 Research Goals</b>	<b>29</b>
<b>5 References</b>	<b>31</b>

<b>Part II</b>	<b>Results and Discussion</b>	<b>41</b>
<b>6</b>	<b>Mechanochemical Induced Structure Transformations in Lithium Titanates: A Detailed PXRD and <math>^6\text{Li}</math> MAS NMR Study</b>	<b>45</b>
6.1	Published Article . . . . .	47
6.2	Supplementary Information . . . . .	64
<b>7</b>	<b>Mechanochemical Synthesis of <math>\text{Mn}_3\text{O}_4</math> Nanocrystals and their Lithium Inter- calation Capability</b>	<b>71</b>
7.1	Published Article . . . . .	73
7.2	Supplementary Information . . . . .	77
<b>8</b>	<b>Reactive Milling Induced Structure Changes in Phenylphosphonic acid Func- tionalized <math>\text{LiMn}_2\text{O}_4</math> Nanocrystals – Synthesis, Rietveld refinement and Ther- mal Stability</b>	<b>81</b>
8.1	Published Article . . . . .	83
8.2	Supplementary Information . . . . .	94
<b>9</b>	<b>Summary and Outlook</b>	<b>99</b>

# List of Figures

1.1	Theophrastus' History of Stones. . . . .	3
1.2	Number of publications per year bearing the keyword "mechanochemistry" . . . . .	4
1.3	Working principle of a planetary ball mill. . . . .	5
1.4	Schematic representation of the forces in a planetary ball mill. . . . .	6
1.5	Typical zirconia grinding vial by <i>Retsch</i> , with 200 zirconia milling balls. . . . .	6
1.6	Schematic of the positions of a milling ball on the surface of the milling vial at different points in time. . . . .	7
1.7	Dependence of the kinetic energy $E_t$ of a ball on the angular velocities $\omega_d$ of the sun disk and $\omega_v$ of the vial. . . . .	8
1.8	Normal pressures in a milling scenario with chrome steel and tungsten carbide milling tools as a function of $\omega_d$ . . . . .	9
1.9	Schematic representation of the formation of dislocations and cracks in a powder particle. . . . .	9
1.10	Schematic representation of the condensation reaction between phenylphosphonic acid and the surface of a metal oxide. . . . .	12
2.1	Working principle of a lithium ion battery. . . . .	13
2.2	Pseudo binary phase diagram of the $\text{Li}_2\text{O}-\text{TiO}_2$ system. . . . .	15
2.3	Structure of $\alpha$ -, $\beta$ - and $\gamma$ - $\text{Li}_2\text{TiO}_3$ . . . . .	16
2.4	Spinel structure of $\text{Li}_4\text{Ti}_5\text{O}_{12}$ . . . . .	17
2.5	Section of the pseudo binary Li-Mn-O phase diagram. . . . .	19
2.6	Crystal structure of cubic and tetragonal spinel $\text{LiMn}_2\text{O}_4$ . . . . .	20
3.1	General features of a PXRD pattern. . . . .	23
3.2	Rietveld plot of the XRD pattern of $\text{Li}_x\text{Mn}_3\text{O}_4$ with a single and a 12 fraction model . . . . .	27
6.1	Table of contents graphic of publication 1 . . . . .	46
7.1	Table of contents graphic of publication 2 . . . . .	72
8.1	Table of contents graphic of publication 3 . . . . .	82



# Abbreviations

<i>bm</i>	ball milling
BuLi	n-butyl lithium
COD	Crystallography Open Database
eq.	molar equivalent
EtOH	ethanol
FWHM	full width at half maximum
<i>GOF</i>	goodness of fit
<i>hebm</i>	high energy ball milling
IB	integral breadth
ICSD	Inorganic Crystal Structure Database
iPrOH	iso-propanol/2-propanol
$L_{Vol}(IB)$	volume weighted ( <i>Vol</i> ) column height ( <i>L</i> ) from integral breadth ( <i>IB</i> )
MA	mechanical alloying
MAS	magic angle spinning ( <i>NMR</i> )
NMR	nuclear magnetic resonance spectroscopy
PPA	phenylphosphonic acid
IR	infrared spectroscopy
(P)ND	(powder) neutron diffraction
(P)XRD	(powder) X-ray diffraction
$R_{exp}$	expected R-factor
$R_{wp}$	weighted profile R-factor
<i>ssr</i>	solid-state reaction
<i>sof</i>	site occupation factor
$Y_i(obs)$	observed ( <i>XRD</i> ) intensity at point <i>i</i>
$Y_i(calc)$	calculated ( <i>XRD</i> ) intensity at point <i>i</i>



# **Part I Introduction**



# 1 Mechanochemistry

## 1.1 A Brief History

The history of mechanochemistry has been excellently described by Takacs [1], and shall be summarized very briefly in the following chapter. The very first documented mechanochemical reaction is attributed to Theophrastus of Eresos, a scholar of Aristotle. Around 300 B.C. he wrote in his book “On Stones” or “De Lapidibus” that rubbing of cinnabar in a copper mortar yields elemental mercury (Equation 1.1) [2, 3].



The translation by Hill [2] is as follows: “This is obtained from native Cinnabar, rubbed with Vinegar in brass Mortar with a brass Pestle.” (Figure 1.1). Even though the ef-

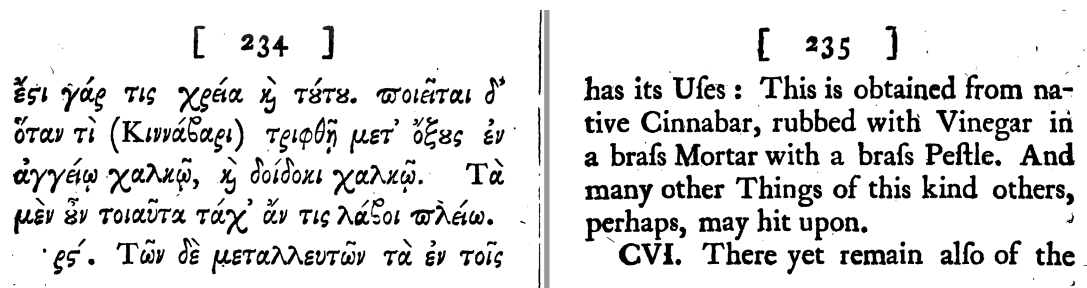
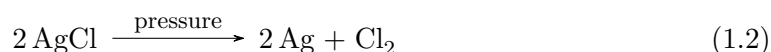


Figure 1.1: Theophrastus' History of Stones. Translation by J. Hill, 1774, London, page 234 - 235 [2]. Original manuscript obtained from books.google.com.

fect of mechanical treatment has been documented that early, it became silent around mechanochemical reactions in the following centuries. The first systematic scientific works have been conducted by M. Carey Lea toward the end of the 17th century. He described the decomposition of silver halogenides (chloride and bromide) by pressing them between sheets of asbestos paper, forming elemental silver and the corresponding halogen (Equation 1.2) [4].



In a later work, the decomposition of several other halogenides like sodium tetrachloroaurate ( $\text{Na}[\text{AuCl}_4]$ ), mercury chlorides and oxides ( $\text{HgCl}_2$ ,  $\text{Hg}_2\text{Cl}_2$ ,  $\text{Hg}_2\text{ClO}$ ,  $\text{HgO}$ ) and silver tartrate, citrate, carbonate, oxalate, arsenate and many more has been observed by simple grinding in a mortar [5]. The word “Mechanochemistry”, as it is used today, was estab-

lished by Ostwald in 1919 in his efforts to systematize chemistry into thermochemistry, electrochemistry, photochemistry and mechanochemistry [1, 6]. Despite this long history of mechanochemistry, it took a long time until it was present as its own important research topic in modern chemistry. A definition in the *IUPAC Compendium of Chemical Terminology* was first added in 1997 and defines a mechanochemical reaction as a “Chemical reaction that is induced by the direct absorption of mechanical energy.” [7]. This slow development is also reflected in the publication history, regarding the keyword “mechanochemistry” (Figure 1.2). There were only few publications until the 1960s. The development of “me-

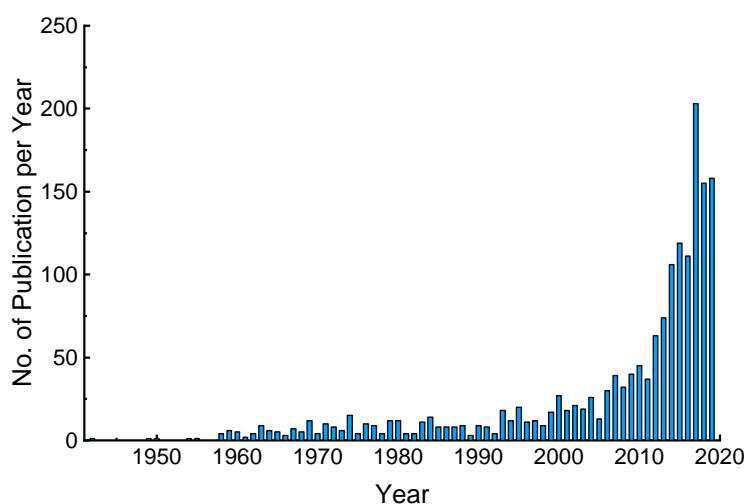


Figure 1.2: Number of publications per year bearing the keyword “mechanochemistry”. Search result by SciFinder, American Chemical Society, accessed 5. September 2019.

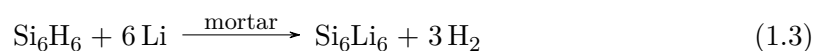
chanical alloying” [8] in the 1970s gave rise to numeral publications, since this allowed to form new alloys, like *Oxide Dispersion-Strengthened* alloys, that could not be obtained before. However, the publication frequency concerning mechanochemical reactions was more or less constant until the mid 1990s. In the years since 2000, mechanochemical reactions have become very prominent. Many reactions can be conducted free of solvents, making mechanochemical synthesis routes ecologically very attractive, while concurrently offering the possibility to obtain products which may not be obtained by other methods [9–12].

## 1.2 Tools for Mechanochemistry

### 1.2.1 Mortar and Pestle

The use of a mortar and pestle is probably one of the most simple ways to induce mechanical energy into a material. These tools are present in nearly every laboratory and are used to grind down coarse grained educt or product powders, homogenize mixtures, break down tablets or minerals or activate the surface of a material for subsequent reactions. These simple tools may already be used to induce mechanochemical reactions.

As already described in the previous chapter, Lea [5] has shown that many mercury and silver compounds decompose under the pressure of a pestle in the mortar. A very interesting observation was the decomposition of mercury chloride ( $\text{HgCl}_2$ ), since it was already known that the compound is stable under static pressure of up to about 70.000 atmospheres. However, rubbing  $\text{HgCl}_2$  in a mortar induces a decomposition. It was concluded, that the shearing stress applied by the movement of the pestle is essential for the decomposition reaction. Although systematic research of mechanochemical reactions with mortar and pestle have been conducted more than 100 years ago, this technique is still applicable in today's time, since it is very easy to perform. Ohashi et al. [13] proposed the mechanochemical lithiation of a layered silane ( $\text{Si}_6\text{H}_6$ ) by grinding it with elemental lithium foil in an agate mortar, inside an argon filled glovebox (Equation 1.3).



The initial educt is a yellow powder. After grinding for several minutes, a greenish color can be observed. The lithium foil disappears completely after grinding for 30 minutes and a dark green powder is obtained. With this mechanochemical reaction a compound is obtained which has not been synthesized by any other reaction method.

### 1.2.2 Planetary Ball Mills

Grinding by hand with a mortar and pestle is quite easy, but the energy input and efficiency is low. A very high, fast and homogeneous energy input can be achieved by using a planetary ball mill. The planetary ball mill has become the most used tool to conduct mechanochemical reactions. A milling vial, containing the educt(s) and the milling balls, rotates around a central point on the "sun wheel". At the same time, the milling vial revolves around itself in the opposite direction, like a planet moves around the sun. A schematic representation is visualized in Figure 1.3. The rotation on the sun wheel leads

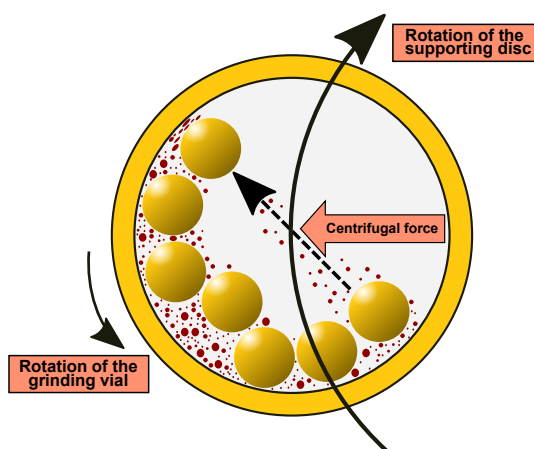


Figure 1.3: Working principle of a planetary ball mill. Yellow circles represent milling balls, small red dots represent the milled powder.

to a centrifugal force, accelerating the material in the vial. Since the vial revolves around itself, the material is continuously brought back to the starting point and the centrifugal force takes effect again. This ball and powder motion allows several forces to take effect, namely impact, friction and shear forces (Figure 1.4). The strength of these forces, especially the impact force, is mainly dependent on rotation speed and diameter of the sun wheel. The force of an accelerated milling ball depends on its weight, which again

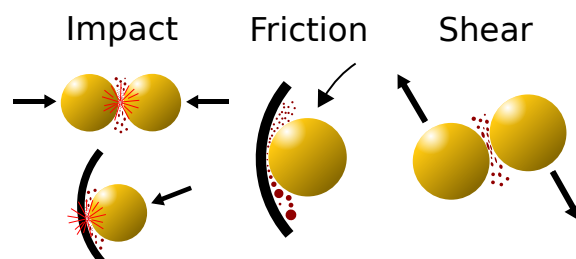


Figure 1.4: Schematic representation of the forces in a planetary ball mill.

is dependent on its density. Typical grinding tool materials are (hardened) steel, agate ( $\text{SiO}_2$ , natural mineral), zirconium oxide ( $\text{ZrO}_2$ , yttrium stabilized) or tungsten carbide (WC, in cobalt matrix), which differ greatly in their density and hardness. A typical zirconia grinding vial is shown in Figure 1.5. There are many more parameters however,



Figure 1.5: Typical zirconia grinding vial by *Retsch*, with 200 zirconia milling balls. The vial has a volume of 45 mL, the balls have a diameter of 5 mm and a weight of approximately 80 g.

that influence the milling process. Milling time and speed, number and size of the milling balls, ball to powder weight ratio, slurry viscosity (in case of wet milling), etc. all affect the outcome of the process. To achieve the highest possible energy input, high milling speeds and very long milling times are necessary. Specialized mills, called “high energy ball mills”, and specialized grinding materials are needed. These are supplied by only a few manufacturers. The most commonly used high energy planetary ball mills in literature are the *AGO-2* mill [14–16], *Retsch PM100* [17, 18] and the *Fritsch Pulverisette* line [12, 19, 20].

### 1.3 Theoretical Aspects

The microscopic effects during the event of a ball-powder collision cannot be directly measured. There are however two widely accepted models to describe the occurring effects, that cause reactions and phase transformations in the milling process. The first model is the so called “Hot Spot model” in which temperatures of several 1000K are assumed to occur in a time frame of  $10^{-4} - 10^{-3}s$  during the event of impact [21–23]. The second model, named “Magma-Plasma model”, is based on the formation of plasmatic states, leading to the emission of smaller pieces of solid matter in an excited state, also in a very short time period [22–24].

In contrast to the microscopic effects, the macroscopic effects in the milling process can be better estimated. Several mathematical models have been established to calculate the movement of the balls in the milling process [25–27]. According to Chattopadhyay et al. [25] the  $x$  and  $y$  position vectors of the ball position at any point  $t$  in time depend on distance  $r_d$  from the center of the rotating disk and the center of the vial (radius of the sun wheel), the radius  $r_v$  of the grinding vial, the angular speed  $\omega_d$  of the sun wheel and the angular speed  $\omega_v$  of the grinding vial in relation to the sun wheel (Equation 1.4 and 1.5 and Figure 1.6).

$$x_1 = r_d \cdot \cos(\omega_d)t + r_v \cdot \cos(\omega_d - \omega_v)t \quad (1.4)$$

$$y_1 = r_d \cdot \sin(\omega_d)t + r_v \cdot \sin(\omega_d - \omega_v)t \quad (1.5)$$

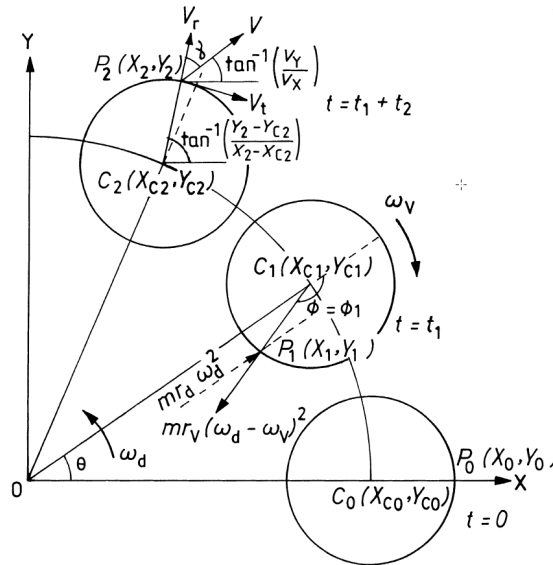


Figure 1.6: Schematic of the positions of a milling ball on the surface of the milling vial at different points in time. Initiation of its motion at  $t = 0$ , detachment at  $t = t_1$  and collision at  $t = t_1 + t_2$ . Reprinted from: P. Chattopadhyay et al., “A mathematical analysis of milling mechanics in a planetary ball mill”, *Mater. Chem. Phys.* **2001**, *68*, 85–94, with permission from Elsevier.

The resulting kinetic energy  $E_t$  of a milling ball may be calculated from its mass  $m_b$  and velocity  $v$  (Equation 1.6); with the velocity being calculated from the first derivative of Equation 1.4 and 1.5.

$$E_t = \frac{1}{2} \cdot m_b \cdot v^2 \quad (1.6)$$

The change of  $E_t$  depending on the angular velocities  $\omega_d$  of the sun disk and  $\omega_v$  of the vial is presented in Figure 1.7<sup>a</sup> [25]. The kinetic energy is primarily correlated to the variation of  $\omega_d$ . An energy of several hundred milli-joules may be achieved for a single milling ball.

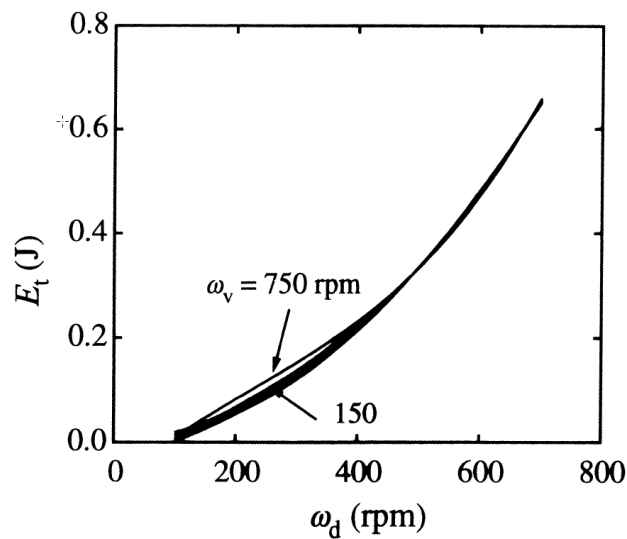


Figure 1.7: Dependence of the kinetic energy  $E_t$  of a ball on the angular velocities  $\omega_d$  of the sun disk and  $\omega_v$  of the vial.<sup>a</sup> Reprinted from: P. Chattopadhyay et al., “A mathematical analysis of milling mechanics in a planetary ball mill”, *Mater. Chem. Phys.* **2001**, 68, 85–94, with permission from Elsevier.

Considering a Hertzian impact condition [28] with a circular area of impact  $a$ , the radial impact force  $F_r$  and the resulting normal pressure  $p_n$  may be obtained from the ball radius  $r_b$ , approach distance  $\delta_r$  of a ball to a surface, elastic modulus  $Y$  and the Poisson’s ratio  $\nu$  (Equation 1.7 and 1.8) [25].

$$F_r = \left(\frac{4}{3}\right) r_b^{1/2} \left(\frac{Y}{1-\nu^2}\right) \delta_r^{3/2} \quad (1.7)$$

$$p_n = \frac{F_r}{\pi a^2} \quad (1.8)$$

<sup>a</sup>Calculations have been based on the use of a Fritsch Pulverisette P5 planetary ball mill with the following milling conditions: (a) chrome steel vials,  $r_v = 75$  mm,  $m_b = 4.2$  g,  $Y = 2.2 \cdot 10^{11}$  GPa and  $\omega_d = 300$  and 260 rpm; (b) WC vials,  $r_v = 75$  mm,  $m_b = 8.4$  g,  $Y = 7.04 \cdot 10^{11}$  GPa and  $\omega_d = 240$  rpm.

The resulting pressures in the case of chrome steel and tungsten carbide milling tools are presented in Figure 1.8 as a function of  $\omega_d$  [25]. Pressures of up to 12 GPa are calculated, which is comparable to the pressure regime achievable with diamond anvil cells (typically up to 20 GPa) [29]. These pressures are high enough to even induce phase transformations in materials.

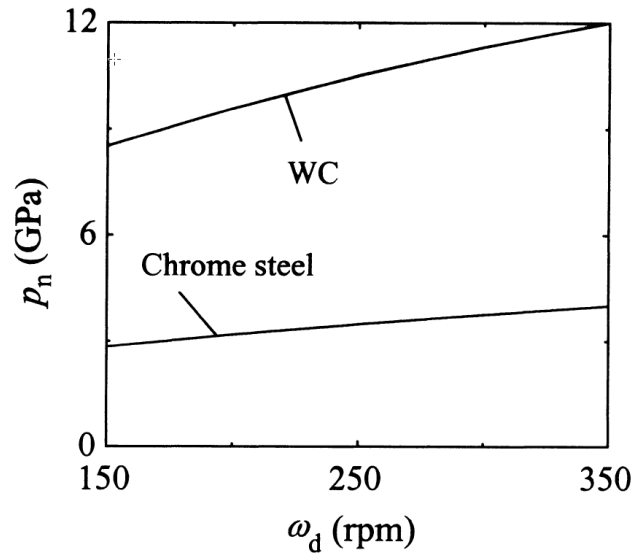


Figure 1.8: Normal pressures in a milling scenario with chrome steel and tungsten carbide milling tools as a function of  $\omega_d$ .<sup>a</sup> Reprinted from: P. Chattopadhyay et al., “A mathematical analysis of milling mechanics in a planetary ball mill”, *Mater. Chem. Phys.* **2001**, *68*, 85–94, with permission from Elsevier.

## 1.4 Applications

### 1.4.1 Size Reduction – A Top-Down Approach

Milling of a powder in a planetary ball mill is usually a *Top-Down* approach, since the coarse grains of a powder are reduced to smaller particles. The collision of an accelerated ball with a much smaller powder particle applies a relatively large force to a very small area, resulting in a very high pressure [26]. Dislocations are formed that initiate cracks in the powder particle, eventually breaking the particle into smaller pieces (Figure 1.9).

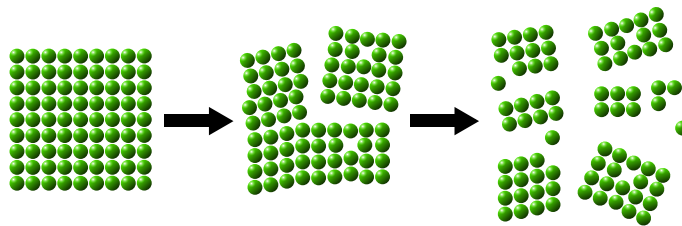


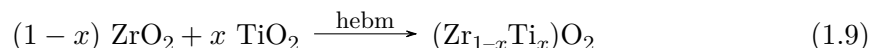
Figure 1.9: Schematic representation of the formation of dislocations and cracks in a powder particle with eventual breakdown to smaller particles.

By applying suitable milling conditions, a size reduction even down to the nanometer scale is possible [30]. Moys [31] has shown that the particle size that may be obtained by milling is limited by the size of the milling balls and the milling time. Small particles can only be obtained by reducing the size of the *grinding zones*, which represent the void volume between the milling balls in an idealized close packing. The smaller this void volume becomes, the smaller the produced particles may be. This can be achieved by using smaller milling balls. However, this reduces the applied energy per volume, since smaller balls have a lower weight and in turn a smaller impact energy. To compensate this effect, the grinding time has to be increased.

### 1.4.2 Mechanochemical Syntheses

Mechanochemical approaches have become important reaction pathways to synthesize (nanocrystalline) materials, that are not obtainable by any other method. A very prominent example is the discovery of “mechanical alloying” (MA) to produce *Oxide Dispersion-Strengthened* alloys, which can not be produced by classical metallurgy [8]. The definition is as follows: “The fundamental process in mechanical alloying to produce metal powders with controlled microstructures is the repeated welding, fracturing, and rewelding of a mixture of powder particles in a dry, highly energetic ball charge.” [8]. MA allows to disperse nano crystalline oxide particles (typically  $\text{Y}_2\text{O}_3$  or  $\text{Al}_2\text{O}_3$ ) in a metal or metal alloy matrix, forming materials with an extremely high temperature stability.

Besides metals and alloys, oxide solid solutions may be obtained by mechanochemical processes. An example is the mechanochemical formation of  $(\text{Zr}_{1-x}\text{Ti}_x)\text{O}_2$  from  $\text{ZrO}_2$  and  $\text{TiO}_2$ , with  $x$  ranging from 0.44 to 0.60 (Equation 1.9) [32]. A typical solid-state synthesis at high temperatures yields solutions in the range  $x = 0.48$  to 0.52 only.



Many oxide materials have been subject to mechanochemical treatment, forming known oxides with low crystallinity, new compounds or structures or inducing effects like ion conductivity [20, 33, 34]. Not only metallic or oxidic compounds may be synthesized by mechanochemical methods. For example, the synthesis of calcium hydride ( $\text{CaH}_2$ ) has been reported by simple milling of elemental calcium with phenylphosphonic acid under argon atmosphere [17]. The classical synthesis for calcium hydride is performed with elemental calcium and hydrogen under pressure and at elevated temperatures up to 500 °C [35].

Even mechanochemical syntheses of organic compounds may be performed. Metal organic frameworks, condensation reactions, coupling reactions or heterogeneous catalysis reactions have been reported, to name only a few [9, 11]. Compared to the classical syntheses in solution, the mechanochemical routes may often be performed without any solvents in a completely dry state. A metal organic framework is for example formed by grinding isonicotinic acid and copper acetate monohydrate for only a few minutes [9].

Additionally, many mechanochemical polymerization reactions have been developed in recent years, allowing to reduce the necessary amount of solvents or even conducting the polymerizations completely free of solvents. This bears the advantage that drawbacks like insolubility and subsequent precipitation of the produced polymers are eliminated. For example, a porous thiophene polymer has been prepared by milling 1,3,5-tris(2-thienyl)benzene with  $\text{FeCl}_3$  for one hour without any solvent [19]. A polycondensation reaction has been conducted by milling a diamine and a dialdehyde and a Suzuki polycondensation has been achieved by using polyphenylenes with minimal amounts of catalyst [12, 36].

### 1.4.3 Mechanical Induced Phase Transformations

As already described in section 1.3, the local microscopic temperature and pressure applied to powder particles in a planetary ball mill are estimated to be in the range of several 1000K and several GPa respectively. These harsh conditions, although short in duration, are sufficient to induce phase transformations to high temperature or high pressure phases. There are several examples of milling induced phase transformations in the area of oxide materials.  $\text{TiO}_2$  with anatase structure for example, reveals a structure change to a high pressure polymorph after milling [37]. Prolonged milling leads to yet another structure change to the rutile structure [37].  $\text{ZrO}_2$  reveals a similar behavior. The cubic high temperature structure of  $\text{ZrO}_2$  normally has to be stabilized by yttrium substitution. Via milling, the monoclinic structure changes to the cubic structure without the need for an ion substitution [38]. Even more complex oxides like  $\text{Li}_2\text{TiO}_3$  undergo a phase transformation. A partial transformation from the monoclinic  $\beta$  to the cubic  $\alpha$  polymorph has been observed after milling in a shaker mill [39]. The cubic  $\alpha$  polymorph is normally obtained from hydrothermal reactions and contains notable amounts of  $\text{OH}^-$  or  $\text{H}_2\text{O}$  molecules [40].

### 1.4.4 Mechanochemical Surface Functionalization

The surface of nano particles is often functionalized with small molecules – like organic phosphonic acids or carboxylic acids – to stabilize particle dispersions by preventing an agglomeration or to change the reaction behavior of the surface in catalytic processes. Examples are the solvent based functionalization of titanium dioxide particles with phosphonates [41] and the synthesis of metal and hematite ( $\text{Fe}_3\text{O}_4$ ) nano particles, which are typically stabilized by oleic acid [42, 43].

The size reduction of powder particles in a milling process also induces the formation of new, reactive surfaces. These freshly formed particle surfaces are able to react in situ in the milling process with small organic molecules, effectively functionalizing the particle surface homogeneously [44]. In this way, the simultaneous formation of titanium dioxide nano particles and an in situ surface functionalization by various organic phosphonic acids has been proposed [18, 45, 46]. The reactive groups on the surface of the particles react in a condensation reaction with the hydroxy groups of the phosphonic acid, forming a

covalent bond. A schematic reaction pathway of phenylphosphonic acid with a metal oxide particle is presented in Figure 1.10. Besides the functionalization with phosphonic acid

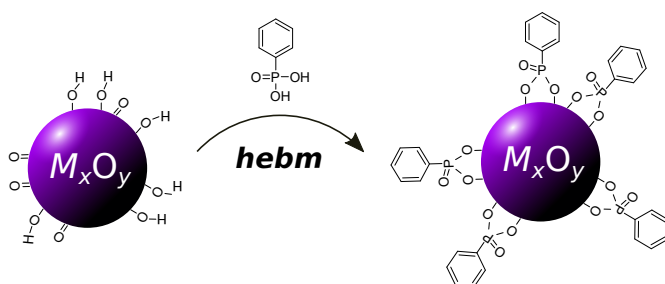


Figure 1.10: Schematic representation of the condensation reaction between phenylphosphonic acid and the surface of a metal oxide  $M_xO_y$ .

and carboxylic acid groups, a mechanochemical functionalization of silicon nano particles with alkyl and alkenyl groups has been reported [47]. The nanoparticles are formed by milling elemental silicon powder in 1-octene or 1-octyne. The alkenes react with the freshly formed surface of these particles by forming stable Si–C bonds.

## 2 Metal Oxides

### 2.1 Lithium Ion Battery Materials

Metal oxides have become prominent materials in the construction of lithium ion batteries, since they can efficiently be used as both cathode and anode materials [48–50]. In a typical charged lithium ion battery the anode is in its reduced state and contains the lithium ions. The cathode is in its oxidized state. The electrodes are separated by a separator containing an electrolyte or by a polymer (Figure 2.1). The performance of such a battery system

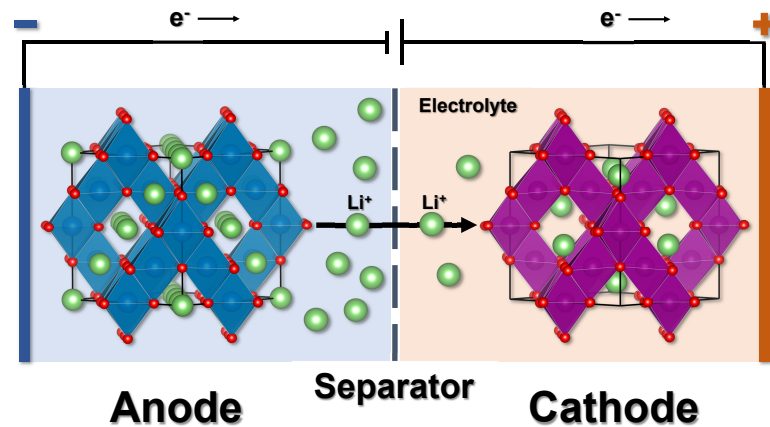


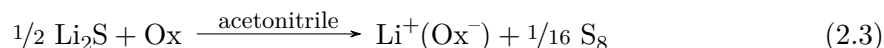
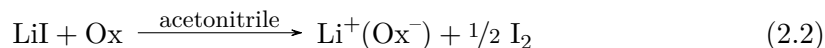
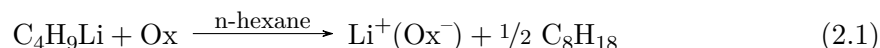
Figure 2.1: Working principle of a lithium ion battery. The charged  $Li_{4+x}Ti_5O_{12}$  anode (left, blue) is in its reduced, lithium rich state. The charged  $LiMn_2O_4$  cathode (right, orange) is in its oxidized, lithium poor state.

is not only dependent on the difference in the working potential of anode and cathode material, but also on the speed of the lithium diffusion and oxidation and reduction reaction on the electrodes. These factors are highly dependent on the structure and particle size of the used materials [50]. The lithium intercalation process itself depends on the structure of the host material. The intercalation puts a strain on the system since the structure becomes deformed – lattice parameters and oxidation state are changing. These factors may block the lithium intercalation at some point. The diffusion speed also depends on the structure, but additionally on the particle, grain or crystallite size. Small scaled or nano scaled materials exhibit much shorter diffusion path lengths and in exchange limit the time required to fully saturate one grain in the intercalation reaction [50, 51]. Therefore, much effort is put into the development of syntheses that produce nanocrystalline electrode materials. Additionally, the post modification, e.g. surface functionalization, of

the produced materials is also a point of interest since this allows to influence effects like surface reactions and phase stability [50].

The most well known and at the same time most important cathode material is lithium cobalt oxide  $\text{LiCoO}_2$ . It was one of the first oxide materials whose lithium intercalation capability has been studied and it was also the first cathode material used in commercial lithium ion batteries [52].  $\text{LiCoO}_2$  has a layered type structure and is able to reversibly deintercalate and intercalate one lithium ion, while changing the oxidation state of cobalt between Co(III) and Co(IV) ( $\text{Li}_{1-x}\text{CoO}_2$ ). Besides layered structure materials, compounds with spinel structure are very attractive [48]. The spinel structure typically offers a 3D ion conductivity and is overall very stable. Spinel  $\text{LiMn}_2\text{O}_4$  has been proposed very early as cathode material [53]. Another spinel type material used in lithium ion batteries is  $\text{Li}_4\text{Ti}_5\text{O}_{12}$ . Because of the very low working voltage based on the Ti(IV)–Ti(III) redox pair, this material is used as an anode material.

Besides the electrochemical characterization, the lithium intercalation capability of materials may also be probed by chemical intercalation. The most commonly used reducing agent is n-butyllithium ( $\text{BuLi}$ ,  $\text{C}_4\text{H}_9\text{Li}$ ), which has been used for lithium intercalation and reduction of several sulfides ( $\text{CuS}$ ,  $\text{TiS}_2$ ,  $\text{MoS}_2$ , ...) and oxides ( $\text{SnO}_2$ ,  $\text{TiO}_2$ ,  $\text{V}_2\text{O}_5$ , ...) [54]. It is commonly handled as a 1.6 or 2.5 molar solution in n-hexane. The general reaction with an oxidizing agent (Ox) is shown in Equation 2.1. Other prominent lithiation agents are  $\text{LiI}$  and  $\text{Li}_2\text{S}$  [55, 56] (?? and ??). Both can be easily weighed as solid powders, however, their use is limited because of some drawbacks. Though also soluble in many aprotic solvents,  $\text{LiI}$  has a much lower reduction potential than  $\text{BuLi}$ . Additionally elemental iodine is formed in the reaction, which may enable additional side reactions.  $\text{Li}_2\text{S}$  has a reduction potential in between  $\text{LiI}$  and  $\text{BuLi}$  allowing it to reduce many cathode materials, however, its low solubility and the formation of elemental sulfur pose a problem in many applications.



Chemical lithiation bears the advantage that structural changes and the resulting phase composition can be evaluated much easier via PXRD measurements than in a complete setup of an electrochemical cell, since only a pure material is used. A battery cell consist of a housing, binder, anode, etc. which all cause additional diffraction signals, making e.g. a structure determination impossible. This advantage has for example been used to investigate the influence of the particle size of  $\text{TiO}_2$  on the degree of lithium intercalation in a reaction with  $\text{BuLi}$  [51]. It has been shown that the diffusion path is restricted to a length of about 10 nm, independent of the particle size. A full lithiation can therefore

only be achieved if the particle size is smaller than 20 nm. Chemical lithium intercalation can also be used to obtain larger quantities of the pure intercalated phase to perform structure refinements or structure solutions, which is very difficult or even impossible with the complex phase mixtures that are typically found in a battery setup. The structures of  $\text{Li}_2\text{Mn}_2\text{O}_4$  and  $\text{LiMn}_3\text{O}_4$  – the lithium intercalation products of spinel  $\text{LiMn}_2\text{O}_4$  and hausmannite  $\text{Mn}_3\text{O}_4$  – were both derived from powder X-ray diffraction and neutron diffraction experiments where the powder samples were obtained by chemical lithium intercalation [53, 57].

## 2.2 Lithium Titanium Oxides

### 2.2.1 Structures and Properties

The phase diagram of  $\text{Li}_2\text{O}-\text{TiO}_2$  is shown in Figure 2.2 and contains the compounds  $\text{Li}_4\text{TiO}_4$ ,  $\text{Li}_2\text{TiO}_3$ ,  $\text{Li}_4\text{Ti}_5\text{O}_{12}$  and  $\text{Li}_2\text{Ti}_3\text{O}_7$  [58–60]. Based on their stability and structure  $\text{Li}_2\text{TiO}_3$  and  $\text{Li}_4\text{Ti}_5\text{O}_{12}$  are the most relevant compounds in this system. The stable struc-

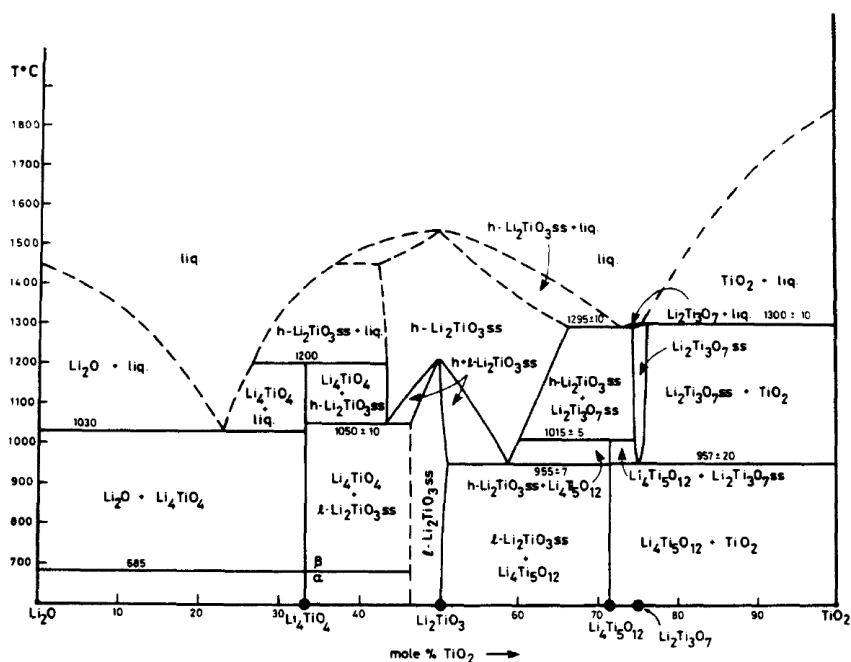


Figure 2.2: Pseudo binary phase diagram of the  $\text{Li}_2\text{O}-\text{TiO}_2$  system. Reprinted from: G. Izquierdo, A. R. West, “Phase equilibria in the system  $\text{Li}_2\text{O}-\text{TiO}_2$ ”, *Mater. Res. Bull.* **1980**, 15, 1655–1660, DOI 10.1016/0025-5408(80)90248-2, with permission from Elsevier.

ture of  $\text{Li}_2\text{TiO}_3$  is a monoclinic layered structure with alternating lithium and titanium layers, denoted as  $\beta\text{-Li}_2\text{TiO}_3$  [61, 62]. Additionally, a high temperature form is known, which is denoted as  $\alpha$ - or  $\gamma\text{-Li}_2\text{TiO}_3$  and crystallizes in the cubic NaCl structure with statistical distribution of lithium and titanium atoms (Figure 2.3) [59, 60, 63]. The cubic structure may also be obtained via a hydrothermal reaction, the product is then denoted

as  $\alpha$ - $\text{Li}_2\text{TiO}_3$ . Since lithium has very low scattering power for X-rays, the accurate refinement of the lithium positions in the structure is difficult via PXRD. Other methods which are more sensitive for lithium have to be considered. One such technique is magic angle spinning (MAS) nuclear magnetic resonance (NMR) spectroscopy. Despite the nucleus spin state of 1, the  $^6\text{Li}$  isotope is well suited to acquire high resolution data, since the quadrupole moment is so small that the spectra are not affected by the otherwise typical quadrupole broadening. On this basis, the lithium distribution in monoclinic  $\beta$ - $\text{Li}_2\text{TiO}_3$  has been investigated by Vijayakumar et al. [64]. It has been shown that the Li1 and Li2 position in the lithium rich layer are magnetically equivalent, forming a single signal. A second signal is attributed to the Li3 position in the Ti layer. Additionally, a third signal is observed which is attributed to lithium atoms in a tetrahedrally coordinated interstitial site.

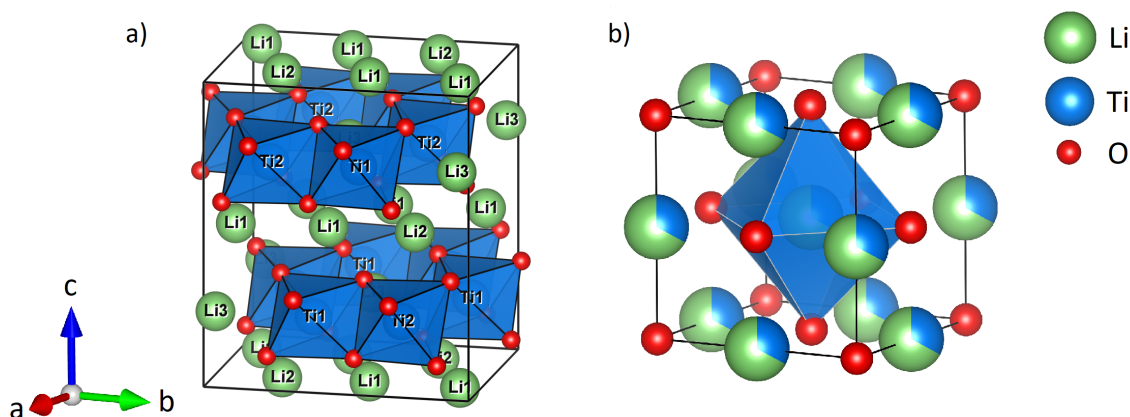


Figure 2.3: Crystal structure of a) monoclinic  $\beta$ - $\text{Li}_2\text{TiO}_3$  with space group  $C2/c$  and b) cubic  $\alpha/\gamma$ - $\text{Li}_2\text{TiO}_3$  with space group  $Fm\bar{3}m$ . Figure reprinted from D. Becker et al., “Mechanochemical Induced Structure Transformations in Lithium Titanates: A Detailed PXRD and  $^6\text{Li}$  MAS NMR Study”, *Inorganics* **2018**, *6*, 117, DOI 10.3390/inorganics6040117 under the terms of the Creative Commons Attribution-NonCommercial License.

The compound  $\text{Li}_2\text{TiO}_3$  is important as a low-activation tritium breeding material [66, 67]. Efforts are made to increase the ion conductivity and reactive surface area, to improve the tritium release. The conductivity of a material can be derived by solid state impedance spectroscopy measurements, where the frequency dependent electrical resistance is obtained. The conductivity is calculated from the reciprocal resistance referred to the sample geometry (contact area of the electrodes and thickness of the sample) [39, 68]. The  $dc$  conductivity is typically compared since this value is independent of the frequency. This value is derived from the plateau which is usually found at lower frequencies. Monoclinic  $\beta$ - $\text{Li}_2\text{TiO}_3$ , that was obtained from a solid state reaction and subsequently milled for two hours, reveals a  $dc$  conductivity of ca.  $10^{-9} \frac{\text{S}}{\text{cm}}$  at room temperature, while the conductivity of the untreated material is about two orders of magnitude lower [39]. The electrochemical activity of hydrothermally prepared  $\text{Li}_2\text{TiO}_3$  has also been a focusing

point. A faster charge transfer kinetics and a higher diffusion rate compared to annealed samples are observed [69]. In both cases the small particle size and disorder in the structure is responsible for the increased conductivity.

The compound  $\text{Li}_4\text{Ti}_5\text{O}_{12}$  crystallizes in the cubic spinel structure, with oxygen atoms forming a cubic close packed array. One eighth of the tetrahedra gaps are occupied by lithium ions, while half of the octahedra gaps are filled with both lithium and titanium atoms. The sum formula may also be written as  $(\text{Li})[\text{Li}_{0.333}\text{Ti}_{1.666}]\text{O}_4$ , where round brackets represent the tetrahedra gap and square brackets represent the octahedra gap (Figure 2.4) [70]. The  $^6\text{Li}$  MAS NMR spectrum of  $\text{Li}_4\text{Ti}_5\text{O}_{12}$  is composed of two slightly overlapping signals in the ration of 3:1, corresponding to the tetrahedrally coordinated lithium on the 8a site and the octahedrally coordinated lithium on the 16d site [71].

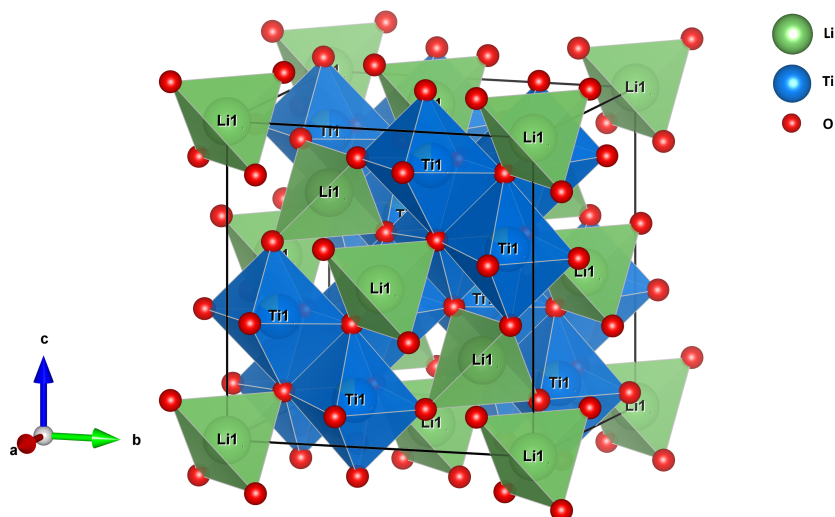


Figure 2.4: Spinel structure of  $\text{Li}_4\text{Ti}_5\text{O}_{12}$  with space group  $Fd\bar{3}m$ . The blue titanium octahedra are partially occupied by lithium (not shown). Figure reprinted from D. Becker et al., “Mechanochemical Induced Structure Transformations in Lithium Titanates: A Detailed PXRD and  $^6\text{Li}$  MAS NMR Study”, *Inorganics* **2018**, *6*, 117, DOI 10.3390/inorganics6040117 under the terms of the Creative Commons Attribution-NonCommercial License.

The Ti(III)/Ti(IV) redox couple has a low potential of ca. 1.5 V vs. elemental lithium, which allows  $\text{Li}_4\text{Ti}_5\text{O}_{12}$  to be used as an anode material. In addition,  $\text{Li}_4\text{Ti}_5\text{O}_{12}$  is well known for its extremely small change in cell volume in the lithium intercalation process, making it a “zero-strain” material [72–76]. This has been shown by in situ and ex situ electrochemical investigations and also by chemical lithium intercalation with BuLi. Up to three lithium atoms can be inserted causing the site occupation to change (Equation 2.4).

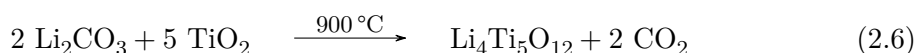


The lithium atoms formerly sitting in the tetrahedra gaps switch to the free octahedra gaps, while the additional inserted lithium atoms also start to occupy the octahedra gaps. The structure changes from spinel type to NaCl type with all octahedra gaps filled.

The electrical and ion conductivity in the fully discharged state is poor. Wilkening et al. [77] have reported a *dc* conductivity value of ca.  $1 \times 10^{-6} \frac{S}{cm}$  at a temperature of 150 °C, for  $\text{Li}_4\text{Ti}_5\text{O}_{12}$  from a typical solid state reaction. The conductivity is slightly increased if the material from a solid state reaction is milled under mild conditions. Iwaniak et al. [68] have reported a *dc* conductivity value of ca.  $1 \times 10^{-7} \frac{S}{cm}$  also at a temperatures of 150 °C. It has been shown that small amounts of Ti(III), introduced either via the substitution of one lithium atom by one magnesium atom ( $\text{Li}_3\text{MgTi}_5\text{O}_{12}$ ), via oxygen defects or via chemical lithiation, largely increase the conductivity to values of about  $10^{-2} \frac{S}{cm}$  at room temperature [71, 77, 78].

### 2.2.2 Synthesis Methods

The aforementioned oxides are typically obtained via solid-state reactions at high temperatures. Coarse grained materials with crystallite sizes above 200 nm are obtained. Monoclinic  $\beta\text{-Li}_2\text{TiO}_3$  may be obtained from  $\text{Li}_2\text{CO}_3$  and  $\text{TiO}_2$  with anatase or rutile structure, at temperatures above 900 °C in air (Equation 2.5) [66, 67, 79]. The cubic  $\gamma$  polymorph can be obtained in the same way, however, temperatures above 1200 °C and fast quenching are necessary [59, 60]. The cubic  $\alpha$  polymorph can be obtained by hydrothermal synthesis from  $\text{LiOH}$  and anatase or rutile in water at temperatures above 140 °C [40, 69, 80, 81].  $\text{Li}_4\text{Ti}_5\text{O}_{12}$  is typically obtained from the same reaction as  $\beta\text{-Li}_2\text{TiO}_3$ , with different stoichiometries of  $\text{Li}_2\text{CO}_3$  and  $\text{TiO}_2$  (Equation 2.6) [70].



To obtain nanosized materials, sintering and crystal growth have to be prevented. Much lower synthesis temperatures, compared to classical solid-state reactions, have to be applied. This may be reached by using extremely well homogenized precursors, effectively shortening diffusion paths. A widely used approach to reduce the sintering temperature is the sol gel technique [82]. For example, nanocrystalline  $\text{Li}_4\text{Ti}_5\text{O}_{12}$  may be obtained by slowly hydrolyzing lithium ethoxide and titanium(IV) *n*-butoxide in absolute ethanol under argon atmosphere [68, 83, 84]. Only moderate sintering temperatures below 600 °C are subsequently necessary to obtain  $\text{Li}_4\text{Ti}_5\text{O}_{12}$ . Materials with crystallite sizes of ca. 10 – 20 nm are typically obtained.

Mechanochemical approaches are generally well-suited to produce nanocrystalline products [10]. However, there are only a few reports of mechanochemical syntheses in the area of lithium titanium oxides. A mechanochemical synthesis to produce cubic  $\alpha\text{-Li}_2\text{TiO}_3$  from  $\text{LiCl}$ ,  $\text{TiO}_2$  and  $\text{NaOH}$  has been developed [85]. The product powder has to be freed of

the formed NaCl matrix with several washing steps and portions of  $\text{LiOH} \cdot \text{H}_2\text{O}$  and  $\text{TiO}_2$  remain as side products. Although broad reflections indicate a small crystallite size, a size determination has not been conducted in this study. Beside this synthesis from simple oxides, a partial phase transformation from the monoclinic  $\beta$  to the cubic  $\alpha$  polymorph has been observed after milling [39]. A complete transformation has not been reported so far.

## 2.3 Lithium Manganese Oxides

### 2.3.1 Structures and Properties

There are many stable manganese oxides and lithium manganese oxides in the Li-Mn-O phase diagram, owed to the many oxidation states of manganese (Figure 2.5). Some examples are  $\text{MnO}$ ,  $\text{Mn}_2\text{O}_3$ ,  $\text{Mn}_3\text{O}_4$  and  $\text{MnO}_2$ , and the lithium containing oxides  $\text{LiMn}_2\text{O}_4$ ,  $\text{LiMnO}_2$  ( $\text{Li}_2\text{Mn}_2\text{O}_4$ ) and  $\text{Li}_2\text{MnO}_3$ . The most important ones used for battery applications are  $\text{Mn}_3\text{O}_4$  and  $\text{LiMn}_2\text{O}_4$ . They both crystallize in the spinel structure and are able

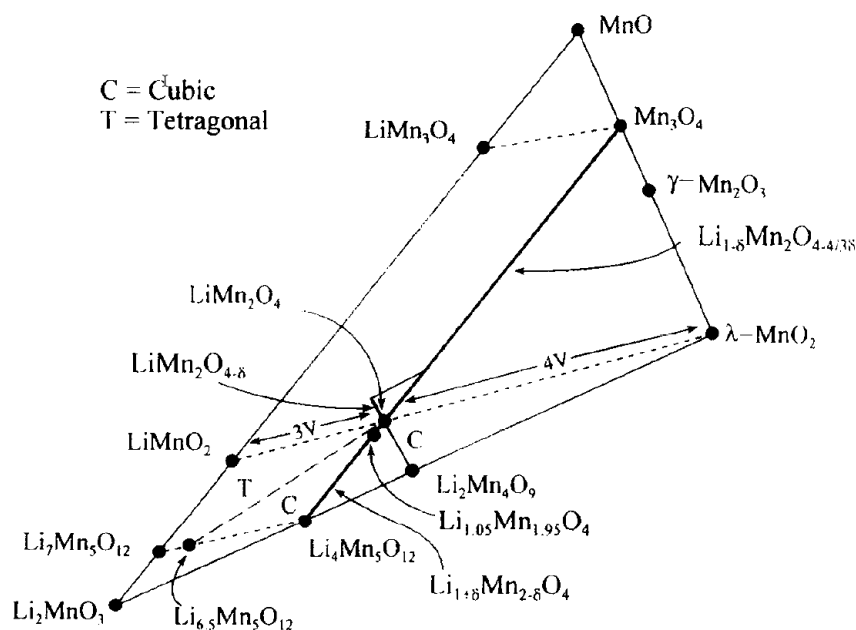
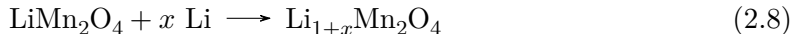
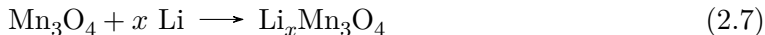


Figure 2.5: Section of the pseudo binary Li-Mn-O phase diagram. Reprinted from: M. Thackeray et al., “The thermal stability of lithium-manganese-oxide spinel phases”, *Mater. Res. Bull.* **1996**, *31*, 133–140, DOI 10.1016/0025-5408(95)00190-5, with permission from Elsevier.

to reversibly intercalate one lithium ion according to Equation 2.7 and 2.8, while providing a maximum voltage of 4 V vs. elemental lithium [53, 57]. This large voltage difference allows to use these materials as cathodes in a battery cell. Additionally,  $\text{Mn}_3\text{O}_4$  reveals a

catalytic activity in decomposing hydrocarbons like methane and nitrogen oxides [87, 88].



$\text{LiMn}_2\text{O}_4$  crystallizes in the ideal cubic spinel structure with space group  $Fd\bar{3}m$ , with Mn(III) and Mn(IV) filling half of the octahedra gaps and Li(I) filling one eighth of the tetrahedra gaps [89]. The structure of  $\text{Mn}_3\text{O}_4$ , also called Hausmannite, is closely related to  $\text{LiMn}_2\text{O}_4$  and can be derived via a symmetry reduction to the space group  $I4_1/amd$ , halving the cell volume [90, 91]. Additionally, the lithium atoms are replaced by manganese. The sum formulas may also be written as  $(\text{Li})[\text{Mn}^{\text{III}}\text{Mn}^{\text{IV}}]\text{O}_4$  and  $(\text{Mn}^{\text{II}})[\text{Mn}_2^{\text{III}}]\text{O}_4$ , where round brackets represent the tetrahedra gap and square brackets represent the octahedra gap. The structures are represented in Figure 2.6. The Jahn-Teller distortion of Mn(III) in  $\text{LiMn}_2\text{O}_4$  is counterbalanced by Mn(IV). In the Hausmannite structure on the other hand, the Jahn-Teller distortion of Mn(III) becomes very dominant, leading to an elongation of the c-axis. Apart from the ideal cubic spinel structure for  $\text{LiMn}_2\text{O}_4$ , a

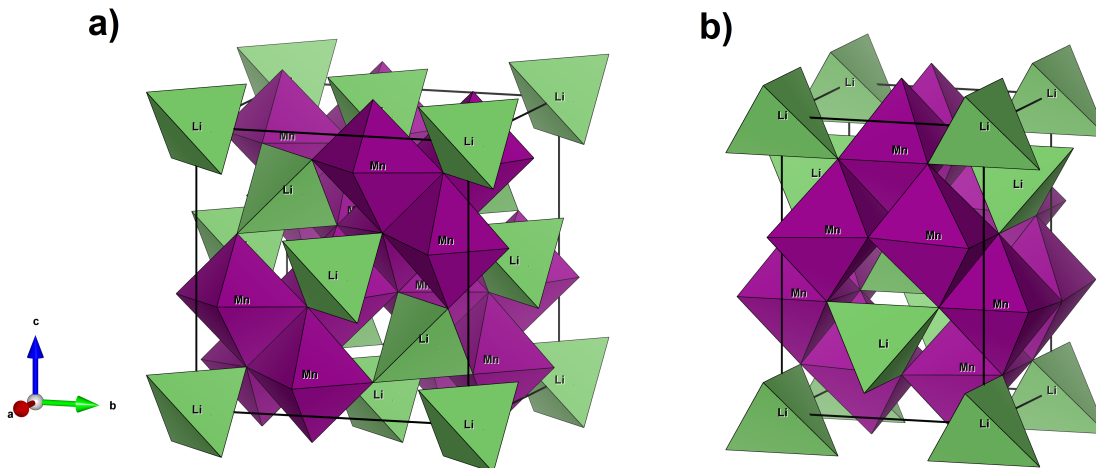


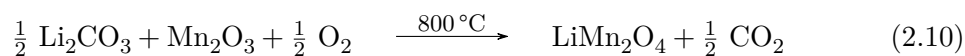
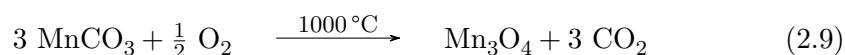
Figure 2.6: Crystal structure of a) cubic spinel  $\text{LiMn}_2\text{O}_4$  with space group  $Fd\bar{3}m$  and b) tetragonal spinel  $\text{LiMn}_2\text{O}_4$  with space group  $I4_1/amd$ . The cubic structure is a  $\sqrt{2} \times \sqrt{2} \times 1$  superstructure of the tetragonal structure. The Hausmannite structure of  $\text{Mn}_3\text{O}_4$  is obtained by substituting the lithium atoms in b) by manganese. The structures were generated with VESTA3 [92].

low temperature phase with lower symmetry is known. At temperatures below 10 °C a transformation to a structure with orthorhombic symmetry with space group  $Fddd$  has been observed [93, 94]. It was later found by synchrotron and powder neutron diffraction (PND) measurements, that the structure may actually be better described by a  $3 \times 3 \times 1$  superstructure of the spinel cell [95]. This structure has also been verified by single crystal diffraction [96]. The phase transformation was reversible in all cases and the cubic spinel structure was obtained again after heating above 25 °C. The orthorhombic structure has

also been obtained by applying static pressures of 2 to 3 GPa [97]. Combined refinements of PND and the resulting pair distribution function (PDF) have revealed that the short-range order at room temperature is actually more closely related to a orthorhombic symmetry, than to a cubic one [98].

### 2.3.2 Synthesis Methods

Most manganese oxides can be synthesized via high temperature solid-state reactions, similar to the previously discussed lithium titanium oxides.  $\text{Mn}_3\text{O}_4$  may be obtained from heating  $\text{MnCO}_3$  to 1000 °C in air, with subsequent quenching (Equation 2.9) [90, 91]. The quenching process is important as the formation of  $\text{Mn}_3\text{O}_4$  and  $\text{Mn}_2\text{O}_3$  depends on the oxygen partial pressure.  $\text{Mn}_3\text{O}_4$  is only stable at temperatures above 1000 °C at the oxygen partial pressure of air. An oxidation process takes place at temperatures below 1000 °C, forming  $\text{Mn}_2\text{O}_3$ . It is therefore not possible to obtain  $\text{Mn}_3\text{O}_4$  at lower sintering temperatures in air.  $\text{LiMn}_2\text{O}_4$  can be obtained by heating  $\text{Li}_2\text{CO}_3$  and “any oxide of manganese” to temperatures between 800 and 900 °C (Equation 2.10) [89]. The products obtained via these high temperature solid-state syntheses are always coarse grained with crystallite sizes above 200 nm.



To obtain nanosized materials, sintering and crystal growth have to be prevented. Much lower synthesis temperatures, compared to classical solid-state reactions, have to be applied. This may be reached by using extremely well homogenized precursors, effectively shortening diffusion paths.  $\text{Mn}_3\text{O}_4$  nanoparticles have been obtained by slowly oxidizing  $\text{Mn}(\text{NO}_3)_2$  with  $\text{H}_2\text{O}_2$  in 1-*n*-butyl-3-methylimidazolium hydroxide ([BMIM]OH), an ionic liquid [99]. The resulting crystallites have a size of about 40 nm. Hydrothermal syntheses are also well suited to produce  $\text{Mn}_3\text{O}_4$  nanoparticles. A  $\text{Mn}(\text{NO}_3)_2$  solution is mixed with a surfactant, such as oleylamine and dodecanol, to produce spherical or rod-like nanoparticles with a size of about 26 nm [100]. Nanocrystalline  $\text{LiMn}_2\text{O}_4$  has been obtained by forming well homogenized gels, similar to a sol-gel process. The gels are formed by dissolving lithium acetate and manganese acetate in ethanol, together with citric acid or tartaric acid as complexation agents. The dried gels are then calcined at 300 °C to obtain crystallites with a size of 15 – 25 nm [101, 102].

As already mentioned in the previous section, mechanochemical approaches are also well-suited to produce nanocrystalline products [10]. However, there are only a few reports of mechanochemical syntheses in the area of manganese oxides and lithium manganese oxides. The mechanochemical synthesis of  $\text{LiMn}_2\text{O}_4$  has been reported by milling of  $\text{LiOH}$ ,  $\text{Li}_2\text{CO}_3$  or  $\text{Li}_2\text{O}$  with  $\text{Mn}_2\text{O}_3$  or  $\text{MnO}_2$  [14–16, 103]. In some cases the reflection pattern of  $\text{LiMn}_2\text{O}_4$  only becomes evident after subsequent heat treatment and no crystallite sizes have been

reported. Besides mechanochemical syntheses, milling of coarse grained spinel  $\text{LiMn}_2\text{O}_4$  has been reported and XRD patterns with severely broadened reflections were obtained [104, 105]. Though the broadening is expected to be due to the reduction of crystallite size and strain that was introduced by milling, the patterns cannot be properly described in refinements with the original structure. A crystallite size cannot be extracted in that case.  $\text{Mn}_3\text{O}_4$  nanoparticles with a size below 100 nm have for example been prepared by a liquid assisted mechanochemical reaction. Pure metals may be milled in distilled water to form the respective metal oxide under formation of hydrogen gas [106]. The drawback of this synthesis is the formation of high pressures of hydrogen, which hinders the use of this method. A similar technique, in which ultrasound is applied to assist the ball milling process, has been developed, forming  $\text{H}_2\text{O}_2$  in situ to oxidize manganese acetate [107]. The final particle size was estimated to be around 30 nm via TEM measurements.

Besides these mechanochemical approaches to form  $\text{Mn}_3\text{O}_4$  directly, there are several studies reviewing the properties of manganese oxides in respect to catalytic activity, thermal stability and magnetism after high energy ball milling. The pure, coarse grained oxides  $\text{MnO}$ ,  $\text{Mn}_3\text{O}_4$ ,  $\text{Mn}_2\text{O}_3$  and  $\text{MnO}_2$  have been reviewed and also mixtures of  $\text{Mn}_3\text{O}_4$  with  $\text{Mn}_2\text{O}_3$  or  $\text{MnO}_2$  and  $\text{Mn}_2\text{O}_3$  with  $\text{MnO}_2$  [108, 109]. A final crystallite size of ca. 20 nm can be obtained if the products are not subject to subsequent heat treatment. Additionally, a ball milling assisted synthesis of  $\text{NiMn}_2\text{O}_4$  has been reported. Pure  $\text{NiO}$  and  $\text{MnO}$  powders were milled and subsequently heat treated [110].

# 3 Powder X-Ray diffraction

## 3.1 Rietveld Refinement

If monochromatic X-rays interact with a periodic crystal, a discrete diffraction pattern is observed. The correlation between wavelength  $\lambda$ , interplanar spacing  $d_{hkl}$  and the diffraction angle  $\theta$  of a local maximum intensity was introduced by Bragg and Bragg [111] and was later called “Bragg’s law” (Equation 3.1).

$$n \cdot \lambda = 2 \cdot d_{hkl} \cdot \sin(\theta) \tag{3.1}$$

This law does not only apply to a perfect single crystal, but also to a powder containing many crystals in random orientation. This allows to obtain  $\theta$  dependent powder patterns containing all  $hkl$ -reflections of the structure in the observed  $\theta$  range, since every  $hkl$ -plane will statistically be in an orientation to fulfill the Bragg condition [112]. A typical powder X-ray diffraction (PXRD) pattern is, however, not only distinguished by the positions of the reflections, but also by the relative intensities of the reflections, their width and shape (Figure 3.1). The integrated intensity  $I_{hkl}$  of a  $hkl$ -reflection is proportional to the square

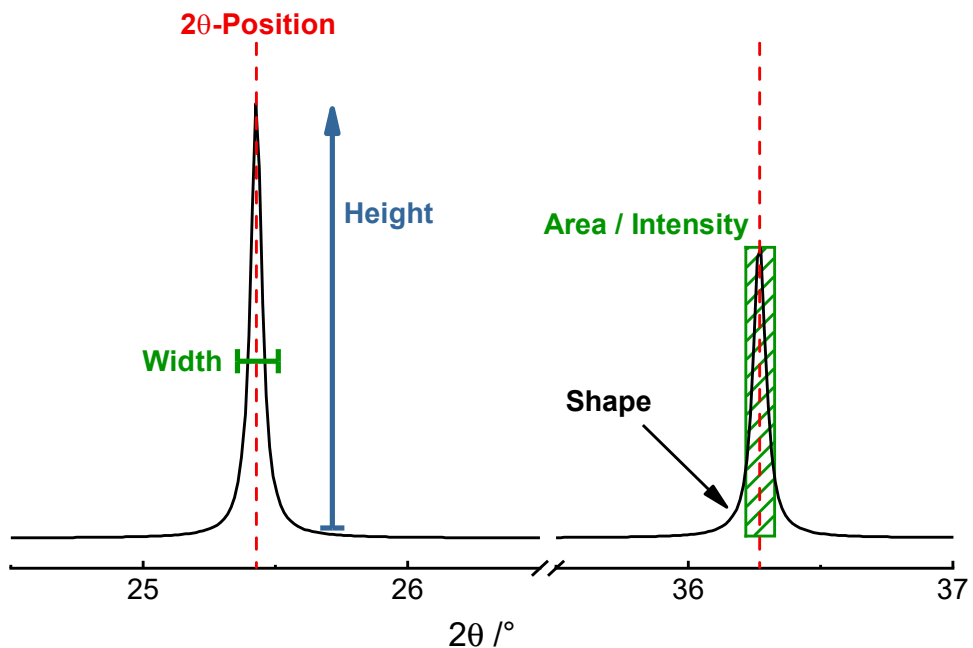


Figure 3.1: General features of a PXRD pattern.

of the corresponding structure factor  $F_{hkl}$  (Equation 3.2). The structure factor depends on the atom types with the atomic form factor  $f$  (which includes the temperature dependence with the atomic displacement factor  $B$ ), the atom positions  $x, y, z$  in the unit cell and the occupation factor  $N$  of the atoms on these positions (Equation 3.3).

$$I_{hkl} \propto |F_{hkl}|^2 \quad (3.2)$$

$$F_{hkl} = \sum_j N_j \cdot f_j \cdot e^{2\pi i(hx_j + ky_j + lz_j)} \quad \text{with } f_j = f_{0,j} \cdot e^{-B_j \left(\frac{\sin(\theta)}{\lambda}\right)^2} \quad (3.3)$$

The intensity of any point in a diffraction pattern of a given structure may be calculated as a sum – scaled by a scaling factor  $s$  – containing the structure factor  $F_K$  (crystal structure dependent), multiplicity factor  $H_K$ , preferred orientation factor  $T_K$ , Lorentz-polarization factor  $LP$ , absorption factor  $A$ , reflection profile function  $\Phi$  and the background  $Y_i(bkg)$  (Equation 3.4, with  $K = hkl$ ) [113].

$$Y_i(calc) = s \cdot \sum_K |F_K|^2 \cdot H_K \cdot T_K \cdot LP \cdot A \cdot \Phi(2\theta_i - 2\theta_K) + Y_i(bkg) \quad (3.4)$$

This relation has been used by Rietveld [114, 115] to refine a crystal structure on the basis of a neutron powder pattern, by correlating the relative intensities to the atomic positions. The basis of the Rietveld method is to describe every observed point  $Y_i(obs)$  of a powder diffraction pattern with a calculated point  $Y_i(calc)$ . The refinement is achieved via minimization of the weighted squares of sums ( $WSS$ ) of the difference of observed and calculated intensities – a least squares process (Equation 3.5). This technique is however not only applicable to neutron, but also to X-ray diffraction data and has, only a short time later, also been applied to X-ray data [116].

$$WSS = \sum_i w_i \cdot |Y_i(obs) - Y_i(calc)|^2 \quad \text{with } w_i = \frac{1}{\sigma^2} [Y_i(obs)] \quad (3.5)$$

Since all atoms or molecules and their respective mass are considered in a Rietveld refinement, the total area of the corresponding reflections may be used to calculate the weight portion of a phase from a multi phase mixture. The weight portion  $W_P$  of a phase  $P$  is calculated from the respective scaling factor  $s_P$ , the number of formula units per unit cell  $Z$ , mass of the formula unit  $M$  and the cell volume  $V$  (Equation 3.6) [117]. This allows to simultaneously conduct structure refinement and quantitative phase analysis.

$$W_P = \frac{s_P(ZMV)_P}{\sum_k s_k(ZMV)_k} \quad (3.6)$$

The quality of a refinement is expressed by a weighted profile R-factor ( $R_{wp}$ ), which is calculated from the square root of the minimized value  $WSS$ , normalized by the sum of the weighted intensities  $Y_i(obs)$  (Equation 3.7). The quality of the obtained data determines

the “best possible”  $R_{wp}$  that can be obtained. This value is called expected R-factor ( $R_{exp}$ ) and depends on the number of data points  $N$  and the number of varied parameters  $P$  (Equation 3.8). Another parameter to quantify the fit quality is the goodness of fit ( $GOF$ ), which is calculated from  $R_{wp}$  and  $R_{exp}$  (Equation 3.9) [118]. In the scenario of a perfect fit this value becomes 1. Values deviating largely from 1 indicate errors in the used refinement model.

$$R_{wp} = \sqrt{\frac{\sum_i w_i \cdot |Y_i(obs) - Y_i(calc)|^2}{\sum_i w_i \cdot |Y_i(obs)|^2}} \quad (3.7)$$

$$R_{exp} = \sqrt{\frac{N - P}{\sum_i w_i \cdot |Y_i(obs)|^2}} \quad (3.8)$$

$$GOF = \frac{R_{wp}}{R_{exp}} \quad (3.9)$$

## 3.2 Line Profile Analysis

In theory, the Bragg condition for any  $d$ -spacing in a perfect sample can only be fulfilled for one specific theta value and strictly monochromatic radiation. An infinitely sharp diffraction line should appear in that case. In reality however, a line broadening is observed. This is due to the imperfection of a real sample and the experimental setup. The broadening caused by the sample arises from its finite crystallite size and local deviations from the average  $d$ -spacing, called micro-strain. The correlation between mean crystallite size  $L$  and reflection width  $b_L$  has been described by Scherrer [119] and was later revised by Patterson [120]. The reflection broadening from the full width at half maximum (FWHM) is inversely proportional to the crystallite size  $L$  and has an angular dependence of  $1/\cos(\theta)$  (Equation 3.10). The constant  $K$  is required to include effects like crystallite shape and size distribution and consequently to correlate the calculated size to a physical crystallite size. The use of the usually unknown factor  $K$  can be omitted by using the integral breadth  $\beta$ .  $K$  becomes 1 in this case, since the integral breadth is independent of the shape and size distribution of the crystallites (Equation 3.11). The micro-strain dependent broadening  $b_S$  is proportional to the lattice strain parameter  $\epsilon_0$  with an angular dependence of  $\tan(\theta)$  (Equation 3.12) [121].

$$b_L = \frac{K \cdot \lambda}{L \cdot \cos(\theta)} \quad (3.10)$$

$$\beta_L = \frac{\lambda}{L \cdot \cos(\theta)} \quad (3.11)$$

$$b_S = 4 \cdot \epsilon_0 \cdot \tan(\theta) \quad (3.12)$$

The earliest attempts to separate size and strain broadening were made by Williamson and Hall [121]. In the case of a purely Lorentzian line shape, the total broadening  $B$  was assumed to be a simple sum of size and strain broadening (Equation 3.13), so that by plotting  $B \cdot \cos(\theta)$  against  $\sin(\theta)$ ,  $b_S$  may be obtained from the slope and  $b_L$  from the intercept on the y-axis (Equation 3.14).

$$B = b_L + b_S \quad (3.13)$$

$$B \cdot \cos(\theta) = \frac{K \cdot \lambda}{L} + 4 \cdot \epsilon_0 \cdot \sin(\theta) \quad (3.14)$$

However, the contribution of instrument and X-ray tube to the total broadening were not considered in this approach. Alexander [122] proposed a convolution based approach to include parts of these effects in crystallite size determination. The fundamental parameters approach was introduced by Cheary and Coelho [123] and interprets the intensity  $Y(2\theta)$  as a convolution of the emission profile  $W$ , instrumental contribution  $G$  and the true physical profile  $S$  (Equation 3.15). The contributions  $W$  and  $G$  may be determined with an ideal sample which is free of strain and has a known homogeneous crystallite and grain size.

$$Y(2\theta) = (W \otimes G) \otimes S \quad (3.15)$$

Besides the consideration of all effects to the line widths, appropriate functions to fit the reflection shape have to be used. To circumvent the limitations in terms of a pure gaussian or lorentzian shape, the “double-voigt approach” has been introduced [124]. This approach allows the simultaneous extraction of crystallite size and strain from the line widths. The convolution based double-voigt approach and fundamental parameters approach are implemented in the Rietveld refinement software TOPAS [125, 126], which is used throughout this thesis.

Line profile shapes that are not only symmetric and isotropic, but much more complex, may arise due to additional effects. Anisotropic line broadening may be caused by variations in the  $d$ -spacing or by anisotropic domain size morphology or crystallite size distributions. Stephens [127] has proposed a method to phenomenologically model anisotropic broadening of reflections. A multi-dimensional distribution of lattice parameters is considered, which is based on few, specific line shape parameters. A model to refine anisotropic broadening due to domain morphology – anisotropic crystallite size – with a physically based geometric description has been proposed by Ectors et al. [128, 129].

### 3.3 Multi-Fraction Models

A distribution of slightly different states in a material, like a variation in the degree of lithiation, may cause a distribution of lattice parameters. This multitude of lattice parameters causes all affected  $hkl$  reflections to be broadened, since the reflections are actually composed of multiple overlapping reflections, or a continuum of reflections, with slightly varying  $d$ -values. The observed diffraction pattern often exhibits reflection profiles that cannot be covered by one single structure model in a Rietveld refinement. If the kind of “defect” causing the distribution is known, a structure model consisting of multiple constrained structures may be deployed. For example, such a “multi-fraction model” has been used by Beck et al. [130] to describe the profile shape of thermally altered chlorovanadato-apatites. The thermal stress causes a chlorine loss, which leads to a contraction of the  $c$ -axis. The chlorine loss is not homogeneous, resulting in a distribution of several  $c$  lattice parameters. The corresponding  $hkl$ -reflections exhibit an asymmetric broadening, which was successfully refined with three constrained fractions of the same structure.

Two other examples, where multi-fraction models are able to accommodate complex line shapes, are the distribution of the degree of lithiation or sodiation in the systems  $AM_{0.5}Fe_{0.5}PO_4$  (with  $A = Li, Na$ ;  $M = Mn, Co$ ) and  $Na_xV_2O_5$ . Haberkorn et al. [131] and Bauer et al. [132] used 11, 34 or even 121 fractions with fixed interpolated lattice parameters to model the different intercalation states, resulting in a distribution of fixed fractions. A distribution of 12 fractions, modeling the system  $Li_xMn_3O_4$  is shown in Figure 3.2 as a general representation (D. Becker, unpublished results). The 12 fraction model (right) is compared to a single fraction refinement (left).

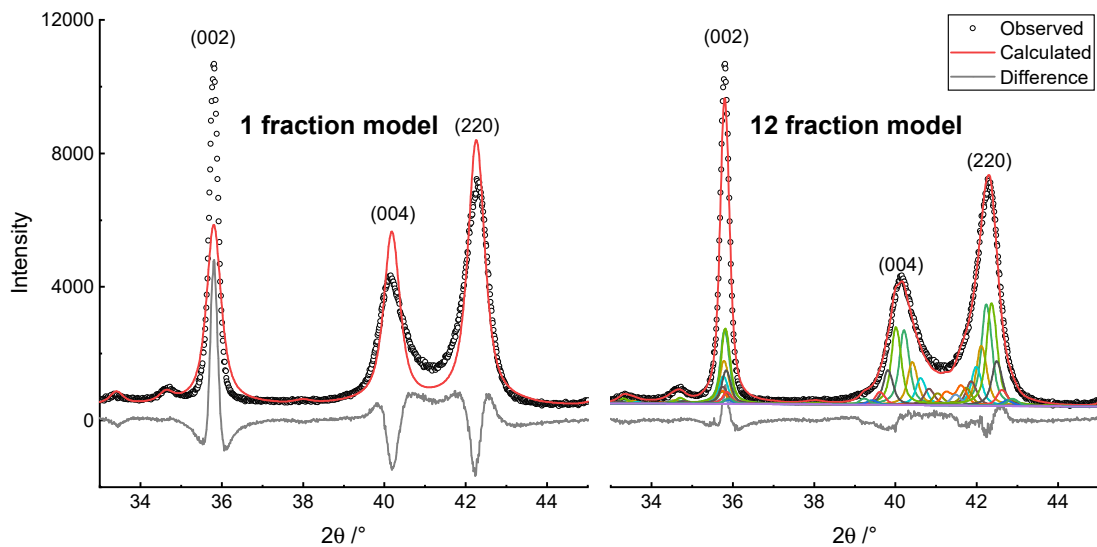


Figure 3.2: Rietveld plot of the XRD pattern of  $Li_xMn_3O_4$  with a single fraction (left) and a 12 fraction model (right). D. Becker, unpublished results.



## 4 Research Goals

### Aim of this work

Mechanochemistry, especially high energy ball milling (*hebm*) in a planetary ball mill, has already been shown to be an effective method to produce nanocrystalline materials and being environmentally friendly at the same time. Most synthetic strategies to produce nanoparticles or nanocrystalline materials involve the use of large amounts of solvents or precursors that are sometimes difficult to prepare or handle. Mechanochemical approaches allow to reduce or even relinquish the use of solvents, performing the milling process completely dry. Since ball milling is a top-down approach, the crystallite size of any crystalline material can be reduced. Additionally, defects may be introduced into the structure. Furthermore, mechanochemistry also offers the possibility to conduct solid-solid reactions and to induce even phase transformations.

Mechanochemical approaches to synthesize or pre-treat metal oxides, that are relevant in battery applications (e.g. as anode or cathode material), have become a focus of research in the last decade, since crystallite size reduction and defect formation may increase the electrochemical performance. However, the features of the resulting powder X-ray diffraction (PXRD) patterns and consequently, effects like strain, disorder and structure changes are seldom regarded.

The aim of this work is to systematically study the effects of high energy ball milling on metal oxides, that are relevant in battery applications, via PXRD and detailed Rietveld refinements. The systems Li-Ti-O and Li-Mn-O have been chosen because several compounds and defined structures exist in these systems that are used as either anode or cathode materials. Studies regarding mechanochemical treatment or mechanochemical syntheses have been reported in some cases, however, few attempts to interpret changes in the structures have been made and even fewer models to conduct accurate Rietveld refinements have been proposed so far. Especially in the case of battery materials, the structure with its defects and the crystallite size play a critical role in the intercalation behavior of the materials. A better understanding of the effects of milling processes on these properties may be of use in future investigations. The potential performance of mechanochemically treated materials may be probed via chemical lithium intercalation and subsequent *ex situ* PXRD. The conductivity can be measured via temperature dependent impedance spectroscopy measurements. Additionally, surface functionalization with organic phosphonic acids and following effects like stabilization have not been reported for lithium manganese oxides.

## Lithium Titanium Oxides

Attempts were made to synthesize  $\text{Li}_2\text{TiO}_3$  from the simple educts  $\text{LiOH}$  and  $\text{TiO}_2$  (rutile and anatase). The optimal synthesis parameters in terms of grinding tool materials, milling speed and milling time shall be reviewed. The quantitative product composition, crystallite size and structure changes can be evaluated by PXRD via Rietveld refinement. Additional information of the local structure can be gained via  $^6\text{Li}$  magic angle spinning (MAS) nuclear magnetic resonance (NMR) spectroscopy. The effects of milling onto the conductivity may be probed via impedance spectroscopy measurements.

## Lithium Manganese Oxides

The mechanochemical synthesis of  $\text{Mn}_3\text{O}_4$  from simple monovalent oxides shall be investigated. A milling map – correlating grinding time, speed and product formation – can be used as a base to find the optimal parameters for the mechanochemical synthesis. The product composition and crystallite size can be evaluated by PXRD via Rietveld refinement. The potential lithium intercalation performance of the nanocrystalline products can be reviewed via chemical lithium intercalation.

Milling of spinel  $\text{LiMn}_2\text{O}_4$  induces line broadening in the respective PXRD patterns which is not only based on simple crystallite size reduction. Structure models to conduct accurate Rietveld refinements shall be developed, allowing to quantify phase composition, phase transformations and additional effects systematically. The thermal stability of the products shall be investigated via *ex situ* and *in situ* PXRD. The effects of adding organic phosphonic acids to the milling process shall be evaluated. An *in situ* surface functionalization is to be expected and may be characterized by infrared spectroscopy. The potential effects like phase stabilization shall be reviewed.

## 5 References

- [1] L. Takacs, “The historical development of mechanochemistry”, *Chem. Soc. Rev.* **2013**, *42*, 7649–7659, DOI 10.1039/c2cs35442j.
- [2] J. Hill, *Theophrastus’s History of stones*, London, **1774**, pp. 234–235.
- [3] L. Takacs, “The First Documented Mechanochemical Reaction?”, *J. Met.* **2000**, 12–13.
- [4] M. C. Lea, “Disruption of the silver haloid molecule by mechanical force”, *Am. J. Sci.* **1892**, *s3-43*, 527–531, DOI 10.2475/ajs.s3-43.258.527.
- [5] M. C. Lea, “III. On endothermic decompositions obtained by pressure. (Second part.) Transformations of energy by shearing stress”, *London Edinburgh Dublin Philos. Mag. J. Sci.* **1894**, *37*, 31–38, DOI 10.1080/14786449408620521.
- [6] W. Ostwald, *Die chemische Literatur und die Organisation der Wissenschaft*. Akad. Verlag. Gesel., **1919**, p. 70.
- [7] A. D. McNaught, A. Wilkinson, *IUPAC Compendium of Chemical Terminology*, Blackwell Scientific Publications, Oxford (1997), **2009**, DOI 10.1351/goldbook.
- [8] P. S. Gilman, J. S. Benjamin, “Mechanical Alloying”, *Annu. Rev. Mater. Sci.* **1987**, *13*, 279–300, DOI 10.1007/BF03258604.
- [9] A. Pichon, A. Lazuen-Garay, S. L. James, “Solvent-free synthesis of a microporous metal-organic framework”, *CrystEngComm* **2006**, *8*, 211–214, DOI 10.1039/b513750k.
- [10] S. L. James, C. J. Adams, C. Bolm, D. Braga, P. Collier, T. Frii c, F. Grepioni, K. D. Harris, G. Hyett, W. Jones, A. Krebs, J. MacK, L. Maini, A. G. Orpen, I. P. Parkin, W. C. Shearouse, J. W. Steed, D. C. Waddell, “Mechanochemistry: Opportunities for new and cleaner synthesis”, *Chem. Soc. Rev.* **2012**, *41*, 413–447, DOI 10.1039/c1cs15171a.
- [11] N. R. Rightmire, T. P. Hanusa, “Advances in organometallic synthesis with mechanochemical methods”, *Dalt. Trans.* **2016**, *45*, 2352–2362, DOI 10.1039/c5dt03866a.
- [12] S. Gr tz, M. Oltermann, E. Troschke, S. Paasch, S. Krause, E. Brunner, L. Borchardt, “Solvent-free synthesis of a porous thiophene polymer by mechanochemical oxidative polymerization”, *J. Mater. Chem. A* **2018**, *6*, 21901–21905, DOI 10.1039/c8ta03684e.

- [13] M. Ohashi, H. Nakano, T. Morishita, M. J. Spencer, Y. Ikemoto, C. Yogi, T. Ohta, “Mechanochemical lithiation of layered polysilane”, *Chem. Commun.* **2014**, *50*, 9761–9764, DOI 10.1039/c4cc03850a.
- [14] N. Kosova, I. Asanov, E. Devyatkina, E. Avvakumov, “State of Manganese Atoms during the Mechanochemical Synthesis of  $\text{LiMn}_2\text{O}_4$ ”, *J. Solid State Chem.* **1999**, *146*, 184–188, DOI 10.1006/jssc.1999.8329.
- [15] N. Kosova, N. Uvarov, E. Devyatkina, E. Avvakumov, “Mechanochemical synthesis of  $\text{LiMn}_2\text{O}_4$  cathode material for lithium batteries”, *Solid State Ionics* **2000**, *135*, 107–114, DOI 10.1016/S0167-2738(00)00288-5.
- [16] N. Kosova, E. Devyatkina, S. Kozlova, “Mechanochemical way for preparation of disordered lithium–manganese spinel compounds”, *J. Power Sources* **2001**, *97-98*, 406–411, DOI 10.1016/S0378-7753(01)00521-3.
- [17] C. Ney, H. Kohlmann, G. Kickelbick, “Metal hydride synthesis through reactive milling of metals with solid acids in a planetary ball mill”, *Int. J. Hydrogen Energy* **2011**, *36*, 9086–9090, DOI 10.1016/j.ijhydene.2011.04.191.
- [18] A. Betke, G. Kickelbick, “Important reaction parameters in the synthesis of phenylphosphonic acid functionalized titania particles by reactive milling”, *New J. Chem.* **2014**, *38*, 1264–1270, DOI 10.1039/C3NJ01291C.
- [19] S. Grätz, L. Borchardt, “Mechanochemical polymerization—controlling a polycondensation reaction between a diamine and a dialdehyde in a ball mill”, *RSC Adv.* **2016**, *6*, 64799–64802, DOI 10.1039/c6ra15677k.
- [20] V. Šepelák, A. Düvel, M. Wilkening, K. D. Becker, P. Heitjans, “Mechanochemical reactions and syntheses of oxides”, *Chem. Soc. Rev.* **2013**, *42*, 7507–7520, DOI 10.1039/c2cs35462d.
- [21] F. P. Bowden, D. Tabor, “The area of contact between stationary and moving surfaces”, *Proc. R. Soc. London. Ser. A. Math. Phys. Sci.* **1939**, *169*, 391–413, DOI 10.1098/rspa.1939.0005.
- [22] P. Baláž, M. Achimovicová, M. Baláž, P. Billik, C. Z. Zara, J. M. Criado, F. Delogu, E. Dutková, E. Gaffet, F. J. Gotor, R. Kumar, I. Mitov, T. Rojac, M. Senna, A. Streletskii, W. C. Krystyna, “Hallmarks of mechanochemistry: From nanoparticles to technology”, *Chem. Soc. Rev.* **2013**, *42*, 7571–7637, DOI 10.1039/c3cs35468g.
- [23] I. Tole, K. Habermehl-Cwirzen, A. Cwirzen, “Mechanochemical activation of natural clay minerals: an alternative to produce sustainable cementitious binders – review”, *Mineral. Petrol.* **2019**, *113*, 449–462, DOI 10.1007/s00710-019-00666-y.
- [24] P. A. Thiessen, K. Meyer, G. Heinicke, *Grundlagen der Tribochemie*, Akademie Verlag, Berlin, **1967**.

- 
- [25] P. Chattopadhyay, I. Manna, S. Talapatra, S. Pabi, “A mathematical analysis of milling mechanics in a planetary ball mill”, *Mater. Chem. Phys.* **2001**, *68*, 85–94.
- [26] A. I. Gusev, A. S. Kurlov, “Production of nanocrystalline powders by high-energy ball milling: Model and experiment”, *Nanotechnology* **2008**, *19*, DOI 10.1088/0957-4484/19/26/265302.
- [27] S. Rosenkranz, S. Breitung-Faes, A. K Wade, “Experimental investigations and modelling of the ball motion in planetary ball mills”, *Powder Technol.* **2011**, *212*, 224–230, DOI 10.1016/j.powtec.2011.05.021.
- [28] H. Hertz, “Ueber die Berührung fester elastischer Körper.”, *J. für die reine und Angew. Math. (Crelles Journal)* **1882**, *1882*, 156–171, DOI 10.1515/crll.1882.92.156.
- [29] A. Jayaraman, “Diamond anvil cell and high-pressure physical investigations”, *Rev. Mod. Phys.* **1983**, *55*, 65–108, DOI 10.1103/RevModPhys.55.65.
- [30] T. Prasad Yadav, R. Manohar Yadav, D. Pratap Singh, “Mechanical Milling: a Top Down Approach for the Synthesis of Nanomaterials and Nanocomposites”, *Nanosci. Nanotechnol.* **2012**, *2*, 22–48, DOI 10.5923/j.nn.20120203.01.
- [31] M. H. Moys, “Grinding to nano-sizes: Effect of media size and slurry viscosity”, *Miner. Eng.* **2015**, *74*, 64–67, DOI 10.1016/j.mineng.2014.11.018.
- [32] L. Kong, J. Ma, W. Zhu, O. Tan, “Phase formation and thermal stability of  $(\text{Zr}_{1-x}\text{Ti}_x)\text{O}_2$  solid solution via a high-energy ball milling process”, *J. Alloys Compd.* **2002**, *335*, 290–296, DOI 10.1016/S0925-8388(01)01844-8.
- [33] M. Obrovac, “Structure and electrochemistry of  $\text{LiMO}_2$  ( $M=\text{Ti, Mn, Fe, Co, Ni}$ ) prepared by mechanochemical synthesis”, *Solid State Ionics* **1998**, *112*, 9–19, DOI 10.1016/S0167-2738(98)00225-2.
- [34] N. M. Cepeda-Sánchez, J. A. Díaz-Guillén, M. Maczka, U. Amador, A. F. Fuentes, “Mechanochemical synthesis, crystal structure and ion conduction in the system  $\text{Gd}_2\text{Hf}_{2-x}\text{Ti}_x\text{O}_7$ ”, *J. Mater. Sci.* **2017**, *52*, 11933–11946, DOI 10.1007/s10853-017-1037-2.
- [35] D. T. Peterson, V. G. Fattore, “Calcium-calcium hydride phase system”, *J. Phys. Chem.* **1961**, *65*, 2062–2064, DOI 10.1021/j100828a034.
- [36] S. Grätz, B. Wolfrum, L. Borchardt, “Mechanochemical Suzuki polycondensation-from linear to hyperbranched polyphenylenes”, *Green Chem.* **2017**, *19*, 2973–2979, DOI 10.1039/c7gc00693d.
- [37] J. Chaudhuri, M. L. Ram, B. K. Sarkar, “Observation of a high pressure polymorph of titania by vibrational ball milling”, *J. Mater. Sci.* **1994**, *29*, 3484–3488, DOI 10.1007/BF00352053.

- [38] S. Bid, S. K. Pradhan, “Preparation and microstructure characterization of ball-milled  $\text{ZrO}_2$  powder by the Rietveld method: Monoclinic to cubic phase transformation without any additive”, *J. Appl. Crystallogr.* **2002**, *35*, 517–525, DOI 10.1107/S0021889802008725.
- [39] H. Brandstätter, D. Wohlmuth, P. Bottke, V. Pregartner, M. Wilkening, “Li Ion Dynamics in Nanocrystalline and Structurally Disordered  $\text{Li}_2\text{TiO}_3$ ”, *Zeitschrift für Phys. Chemie* **2015**, *229*, 1363–1374, DOI 10.1515/zpch-2014-0665.
- [40] A. Laumann, K. T. Fehr, M. Wachsmann, M. Holzapfel, B. B. Iversen, “Metastable formation of low temperature cubic  $\text{Li}_2\text{TiO}_3$  under hydrothermal conditions — Its stability and structural properties”, *Solid State Ionics* **2010**, *181*, 1525–1529, DOI 10.1016/j.ssi.2010.08.017.
- [41] G. Guerrero, P. H. Mutin, A. Vioux, “Anchoring of phosphonate and phosphinate coupling molecules on titania particles”, *Chem. Mater.* **2001**, *13*, 4367–4373, DOI 10.1021/cm001253u.
- [42] P. De La Presa, M. Multigner, J. De La Venta, M. A. García, M. L. Ruiz-González, “Structural and magnetic characterization of oleic acid and oleylamine-capped gold nanoparticles”, *J. Appl. Phys.* **2006**, *100*, DOI 10.1063/1.2401314.
- [43] L. Zhang, R. He, H. C. Gu, “Oleic acid coating on the monodisperse magnetite nanoparticles”, *Appl. Surf. Sci.* **2006**, *253*, 2611–2617, DOI 10.1016/j.apsusc.2006.05.023.
- [44] A. Nasser, U. Mingelgrin, “Mechanochemistry: A review of surface reactions and environmental applications”, *Appl. Clay Sci.* **2012**, *67-68*, 141–150, DOI 10.1016/j.clay.2011.11.018.
- [45] A. Fischer, C. Ney, G. Kickelbick, “Synthesis of Surface-Functionalized Titania Particles with Organophosphorus Coupling Agents by Reactive Milling”, *Eur. J. Inorg. Chem.* **2013**, *2013*, 5701–5707, DOI 10.1002/ejic.201300589.
- [46] A. Betke, G. Kickelbick, “Long Alkyl Chain Organophosphorus Coupling Agents for in Situ Surface Functionalization by Reactive Milling”, *Inorganics* **2014**, *2*, 410, DOI 10.3390/inorganics2030410.
- [47] A. S. Heintz, M. J. Fink, B. S. Mitchell, “Mechanochemical synthesis of blue luminescent alkyl/alkenyl-passivated silicon nanoparticles”, *Adv. Mater.* **2007**, *19*, 3984–3988, DOI 10.1002/adma.200602752.
- [48] M. M. Thackeray, “Spinel Electrodes for Lithium Batteries”, *J. Am. Ceram. Soc.* **2004**, *82*, 3347–3354, DOI 10.1111/j.1151-2916.1999.tb02250.x.
- [49] C. Daniel, D. Mohanty, J. Li, D. L. Wood, “Cathode materials review”, *AIP Conf. Proc.* **2014**, *1597*, 26–43, DOI 10.1063/1.4878478.
- [50] N. Nitta, F. Wu, J. T. Lee, G. Yushin, “Li-ion battery materials: present and future”, *Mater. Today* **2015**, *18*, 252–264, DOI 10.1016/j.mattod.2014.10.040.

- 
- [51] M. Wagemaker, W. J. H. Borghols, F. M. Mulder, "Large Impact of Particle Size on Insertion Reactions. A Case for Anatase  $\text{Li}_x\text{TiO}_2$ ", *J. Am. Chem. Soc.* **2007**, *129*, 4323–4327, DOI 10.1021/ja067733p.
- [52] K. Mizushima, P. Jones, P. Wiseman, J. Goodenough, " $\text{Li}_x\text{CoO}_2$  ( $0 < x < 1$ ): A new cathode material for batteries of high energy density", *Solid State Ionics* **1981**, *3-4*, 171–174, DOI 10.1016/0167-2738(81)90077-1.
- [53] M. Thackeray, W. David, P. Bruce, J. Goodenough, "Lithium insertion into manganese spinels", *Mater. Res. Bull.* **1983**, *18*, 461–472, DOI 10.1016/0025-5408(83)90138-1.
- [54] M. S. Whittingham, "n-Butyllithium – An Effective, General Cathode Screening Agent", *J. Electrochem. Soc.* **2006**, *124*, 1387, DOI 10.1149/1.2133659.
- [55] C. Satto, P. Sciau, E. Dooryhee, J. Galy, P. Millet, "The  $\delta \rightarrow \epsilon \rightarrow \gamma$   $\text{LiV}_2\text{O}_5$  "High Temperature" Phase Transitions Evidenced by Synchrotron X-Ray Powder Diffraction Analysis", *J. Solid State Chem.* **1999**, *146*, 103–109, DOI 10.1006/jssc.1999.8314.
- [56] B. Chaloner-Gill, D. R. Shackle, T. N. Andersen, "A Vanadium-Based Cathode for Lithium-Ion Batteries", *J. Electrochem. Soc.* **2000**, *147*, 3575, DOI 10.1149/1.1393941.
- [57] W. David, M. Thackeray, L. De Picciotto, J. Goodenough, "Structure refinement of the spinel-related phases  $\text{Li}_2\text{Mn}_2\text{O}_4$  and  $\text{Li}_{0.2}\text{Mn}_2\text{O}_4$ ", *J. Solid State Chem.* **1987**, *67*, 316–323, DOI 10.1016/0022-4596(87)90369-0.
- [58] G. Izquierdo, A. R. West, "Phase equilibria in the system  $\text{Li}_2\text{O-TiO}_2$ ", *Mater. Res. Bull.* **1980**, *15*, 1655–1660, DOI 10.1016/0025-5408(80)90248-2.
- [59] J. C. Mikkelsen, "Pseudobinary Phase Relations of  $\text{Li}_2\text{Ti}_3\text{O}_7$ ", *J. Am. Ceram. Soc.* **1980**, *63*, 331–335, DOI 10.1111/j.1151-2916.1980.tb10732.x.
- [60] H. Kleykamp, "Phase equilibria in the Li–Ti–O system and physical properties of  $\text{Li}_2\text{TiO}_3$ ", *Fusion Eng. Des.* **2002**, *61-62*, 361–366, DOI 10.1016/S0920-3796(02)00120-5.
- [61] G. Lang, "Die Kristallstruktur einiger Vertreter der Verbindungsklasse  $\text{Me}_2^I\text{Me}^{IV}\text{O}_3$  als Beitrag zur Aufklärung der Ordnungsphase von  $\text{Li}_2\text{TiO}_3$ ", *ZAAC J. Inorg. Gen. Chem.* **1954**, *276*, 77–94, DOI 10.1002/zaac.19542760109.
- [62] K. Kataoka, Y. Takahashi, N. Kijima, H. Nagai, J. Akimoto, Y. Idemoto, K. ichi Ohshima, "Crystal growth and structure refinement of monoclinic  $\text{Li}_2\text{TiO}_3$ ", *Mater. Res. Bull.* **2009**, *44*, 168–172, DOI 10.1016/j.materresbull.2008.03.015.
- [63] C. Giquel, M. M. Mayer, R. Bouaziz, M. G. Champetier, "Sur quelques composés oxygénés du titane et des alcalins (Li, Na); étude des binaires  $M_2\text{O-TiO}_2$  dans les zones riches en oxyde alcalin.", *C. R. Acad. Sc. Paris* **1972**, *275*, 1427–1430.

- [64] M. Vijayakumar, S. Kerisit, Z. Yang, G. L. Graff, J. Liu, J. A. Sears, S. D. Burton, K. M. Rosso, J. Hu, “Combined 6,7Li NMR and Molecular Dynamics Study of Li Diffusion in  $\text{Li}_2\text{TiO}_3$ ”, *J. Phys. Chem. C* **2009**, *113*, 20108–20116, DOI 10.1021/jp9072125.
- [65] D. Becker, R. Haberkorn, G. Kickelbick, “Mechanochemical Induced Structure Transformations in Lithium Titanates: A Detailed PXRD and 6Li MAS NMR Study”, *Inorganics* **2018**, *6*, 117, DOI 10.3390/inorganics6040117.
- [66] J. Kopasz, J. Miller, C. Johnson, “Tritium release from lithium titanate, a low-activation tritium breeding material”, *J. Nucl. Mater.* **1994**, *212-215*, 927–931, DOI 10.1016/0022-3115(94)90971-7.
- [67] N. Roux, J. Avon, A. Floreancing, J. Mougin, B. Rasneur, S. Ravel, “Low-temperature tritium releasing ceramics as potential materials for the ITER breeding blanket”, *J. Nucl. Mater.* **1996**, *233-237*, 1431–1435, DOI 10.1016/S0022-3115(96)00136-5.
- [68] W. Iwaniak, J. Fritzsche, M. Zukalová, R. Winter, M. Wilkening, P. Heitjans, “Li Conductivity of Nanocrystalline  $\text{Li}_4\text{Ti}_5\text{O}_{12}$  Prepared by a Sol-Gel Method and High-Energy Ball Milling”, *Defect Diffus. Forum* **2009**, *289-292*, 565–570, DOI 10.4028/www.scientific.net/DDF.289-292.565.
- [69] D. Fattakhova, P. Krtil, “Electrochemical Activity of Hydrothermally Synthesized Li-Ti-O Cubic Oxides toward Li Insertion”, *J. Electrochem. Soc.* **2002**, *149*, A1224, DOI 10.1149/1.1499500.
- [70] K. Kataoka, Y. Takahashi, N. Kijima, J. Akimoto, K. ichi Ohshima, “Single crystal growth and structure refinement of  $\text{Li}_4\text{Ti}_5\text{O}_{12}$ ”, *J. Phys. Chem. Solids* **2008**, *69*, 1454–1456, DOI 10.1016/j.jpcs.2007.10.134.
- [71] W. Schmidt, M. Wilkening, “Discriminating the Mobile Ions from the Immobile Ones in  $\text{Li}_{4+x}\text{Ti}_5\text{O}_{12}$ :  $^6\text{Li}$  NMR Reveals the Main  $\text{Li}^+$  Diffusion Pathway and Proposes a Refined Lithiation Mechanism”, *J. Phys. Chem. C* **2016**, *120*, 11372–11381, DOI 10.1021/acs.jpcc.6b02828.
- [72] K. Colbow, J. Dahn, R. Haering, “Structure and electrochemistry of the spinel oxides  $\text{LiTi}_2\text{O}_4$  and  $\text{Li}_{4/3}\text{Ti}_{5/3}\text{O}_4$ ”, *J. Power Sources* **1989**, *26*, 397–402, DOI 10.1016/0378-7753(89)80152-1.
- [73] K. Zaghib, M. Simoneau, M. Armand, M. Gauthier, “Electrochemical study of  $\text{Li}_4\text{Ti}_5\text{O}_{12}$  as negative electrode for Li-ion polymer rechargeable batteries”, *J. Power Sources* **1999**, *81-82*, 300–305, DOI 10.1016/S0378-7753(99)00209-8.
- [74] F. Ronci, P. Reale, B. Scrosati, S. Panero, V. Rossi Albertini, P. Perfetti, M. Di Michiel, J. M. Merino, “High-resolution in-situ structural measurements of the  $\text{Li}_{4/3}\text{Ti}_{5/3}\text{O}_4$  "zero-strain" insertion material”, *J. Phys. Chem. B* **2002**, *106*, 3082–3086, DOI 10.1021/jp013240p.

- [75] L. Aldon, P. Kubiak, M. Womes, J. C. Jumas, J. Olivier-Fourcade, J. L. Tirado, J. I. Corredor, C. Pérez Vicente, “Chemical and Electrochemical Li-Insertion into the  $\text{Li}_4\text{Ti}_5\text{O}_{12}$  Spinel”, *Chem. Mater.* **2004**, *16*, 5721–5725, DOI 10.1021/cm0488837.
- [76] K. Ariyoshi, R. Yamato, T. Ohzuku, “Zero-strain insertion mechanism of  $\text{Li}[\text{Li}_{1/3}\text{Ti}_{5/3}]\text{O}_4$  for advanced lithium-ion (shuttlecock) batteries”, *Electrochim. Acta* **2005**, *51*, 1125–1129, DOI 10.1016/j.electacta.2005.05.053.
- [77] M. Wilkening, R. Amade, W. Iwaniak, P. Heitjans, “Ultraslow Li diffusion in spinel-type structured  $\text{Li}_4\text{Ti}_5\text{O}_{12}$  – A comparison of results from solid state NMR and impedance spectroscopy”, *Phys. Chem. Chem. Phys.* **2007**, *9*, 1239–1246, DOI 10.1039/b616269j.
- [78] C. H. Chen, J. T. Vaughey, A. N. Jansen, D. W. Dees, A. J. Kahaian, T. Goacher, M. M. Thackeray, “Studies of Mg-Substituted  $\text{Li}_{4-x}\text{Mg}_x\text{Ti}_5\text{O}_{12}$  Spinel Electrodes ( $0 < x < 1$ ) for Lithium Batteries”, *J. Electrochem. Soc.* **2001**, *148*, A102, DOI 10.1149/1.1344523.
- [79] D. Mandal, M. Sheno, S. Ghosh, “Synthesis & fabrication of lithium-titanate pebbles for ITER breeding blanket by solid state reaction & spherodization”, *Fusion Eng. Des.* **2010**, *85*, 819–823, DOI 10.1016/j.fusengdes.2010.06.018.
- [80] A. Laumann, K. T. Fehr, H. Boysen, M. Hölzel, M. Holzapfel, “Temperature-dependent structural transformations of hydrothermally synthesized cubic  $\text{Li}_2\text{TiO}_3$  studied by in-situ neutron diffraction”, *Zeitschrift für Krist.* **2011**, *226*, 53–61, DOI 10.1524/zkri.2011.1286.
- [81] A. Laumann, K. M. Ørnsbjerg Jensen, C. Tyrsted, M. Bremholm, K. T. Fehr, M. Holzapfel, B. B. Iversen, “In-situ Synchrotron X-ray Diffraction Study of the Formation of Cubic  $\text{Li}_2\text{TiO}_3$  Under Hydrothermal Conditions”, *Eur. J. Inorg. Chem.* **2011**, *2011*, 2221–2226, DOI 10.1002/ejic.201001133.
- [82] L. L. Hench, J. K. West, “The Sol-Gel Process”, *Chem. Rev.* **1990**, *90*, 33–72, DOI 10.1021/cr00099a003.
- [83] L. Kavana, M. Grätzel, “Facile synthesis of nanocrystalline  $\text{Li}_4\text{Ti}_5\text{O}_{12}$  (Spinel) exhibiting fast Li insertion”, *Electrochem. Solid-State Lett.* **2002**, *5*, 39–42, DOI 10.1149/1.1432783.
- [84] M. Kalbáč, M. Zukalová, L. Kavan, “Phase-pure nanocrystalline  $\text{Li}_4\text{Ti}_5\text{O}_{12}$  for a lithium-ion battery”, *J. Solid State Electrochem.* **2003**, *8*, 2–6, DOI 10.1007/s10008-003-0415-7.
- [85] I. Carbajal-Ramos, J. Andrade-Gamboa, A. Condó, F. Gennari, “Formation of cubic  $\text{Li}_2\text{TiO}_3$  by mechanical activation and its transformation to monoclinic phase: Stability in helium and hydrogen flows”, *Solid State Ionics* **2017**, *308*, 46–53, DOI 10.1016/j.ssi.2017.05.017.

- [86] M. Thackeray, M. Mansuetto, D. Dees, D. Vissers, “The thermal stability of lithium-manganese-oxide spinel phases”, *Mater. Res. Bull.* **1996**, *31*, 133–140, DOI 10.1016/0025-5408(95)00190-5.
- [87] T. Yamashita, A. Vannice, “NO Decomposition over  $\text{Mn}_2\text{O}_3$  and  $\text{Mn}_3\text{O}_4$ ”, *J. Catal.* **1996**, *163*, 158–168, DOI 10.1006/jcat.1996.0315.
- [88] E. Stobbe, B. de Boer, J. Geus, “The reduction and oxidation behaviour of manganese oxides”, *Catal. Today* **1999**, *47*, 161–167, DOI 10.1016/S0920-5861(98)00296-X.
- [89] D. Wickham, W. Croft, “Crystallographic and magnetic properties of several spinels containing trivalent manganese”, *J. Phys. Chem. Solids* **1958**, *7*, 351–360, DOI 10.1016/0022-3697(58)90285-3.
- [90] R. Perthel, H. Jahn, “Über das paramagnetische Verhalten von  $\text{Mn}_3\text{O}_4$  und  $\text{Co}_3\text{O}_4$ ”, *Phys. status solidi* **1964**, *5*, 563–568, DOI 10.1002/pssb.19640050313.
- [91] R. Buhl, “Manganites spinelles purs d’elements de transition preparations et structures cristallographiques”, *J. Phys. Chem. Solids* **1969**, *30*, 805–812, DOI 10.1016/0022-3697(69)90275-3.
- [92] K. Momma, F. Izumi, “VESTA 3 for three-dimensional visualization of crystal, volumetric and morphology data”, *J. Appl. Crystallogr.* **2011**, *44*, 1272–1276, DOI 10.1107/S0021889811038970.
- [93] H. Hayakawa, T. Takada, H. Enoki, E. Akiba, “New findings on the structural phase transitions of spinel  $\text{LiMn}_2\text{O}_4$  at low temperature”, *J. Mater. Sci. Lett.* **1998**, *17*, 811–812, DOI 10.1023/A:1006682304966.
- [94] K. Oikawa, T. Kamiyama, F. Izumi, B. C. Chakoumakos, H. Ikuta, M. Wakihara, J. Li, Y. Matsui, “Structural phase transition of the spinel-type oxide  $\text{LiMn}_2\text{O}_4$ ”, *Solid State Ionics* **1998**, *109*, 35–41, DOI 10.1016/S0167-2738(98)00073-3.
- [95] V. Massarotti, D. Capsoni, M. Bini, P. Scardi, M. Leoni, V. Baron, H. Berg, “ $\text{LiMn}_2\text{O}_4$  low-temperature phase: synchrotron and neutron diffraction study”, *J. Appl. Crystallogr.* **1999**, *32*, 1186–1189, DOI 10.1107/S0021889899011577.
- [96] J. Akimoto, Y. Takahashi, Y. Gotoh, S. Mizuta, “Single Crystal X-ray Diffraction Study of the Spinel-type  $\text{LiMn}_2\text{O}_4$ ”, *Chem. Mater.* **2000**, *12*, 3246–3248, DOI 10.1021/cm0003673.
- [97] A. Paolone, A. Sacchetti, P. Postorino, R. Cantelli, A. Congeduti, G. Rousse, C. Masquelier, “Stabilization of an orthorhombic phase in  $\text{LiMn}_2\text{O}_4$  by means of high pressure”, *Solid State Ionics* **2005**, *176*, 635–639, DOI 10.1016/j.ssi.2004.10.007.
- [98] K. Kodama, N. Igawa, S. I. Shamoto, K. Ikeda, H. Oshita, N. Kaneko, T. Otomo, K. Suzuya, “Local lattice distortion caused by short range charge ordering in  $\text{LiMn}_2\text{O}_4$ ”, *J. Phys. Soc. Japan* **2013**, *82*, 1–6, DOI 10.7566/JPSJ.82.094601.

- [99] Z. Durmus, H. Kavas, A. Baykal, M. S. Toprak, “A green chemical route for the synthesis of  $\text{Mn}_3\text{O}_4$  nanoparticles”, *Cent. Eur. J. Chem.* **2009**, *7*, 555–559, DOI 10.2478/s11532-009-0049-4.
- [100] P. Li, C. Nan, Z. Wei, J. Lu, Q. Peng, Y. Li, “ $\text{Mn}_3\text{O}_4$  nanocrystals: Facile synthesis, controlled assembly, and application”, *Chem. Mater.* **2010**, *22*, 4232–4236, DOI 10.1021/cm100831q.
- [101] Y.-M. Hon, K.-Z. Fung, M.-H. Hon, “Effect of Temperature and Atmosphere on Phase Stability and Morphology of  $\text{LiMn}_2\text{O}_4$  Powder Synthesized by Citric Acid Gel Process.”, *J. Ceram. Soc. Japan* **2000**, *108*, 462–468, DOI 10.2109/jcersj.108.1257\_462.
- [102] Y. Hon, S. Lin, K. Fung, M. Hon, “Synthesis and characterization of nano- $\text{LiMn}_2\text{O}_4$  powder by tartaric acid gel process”, *J. Eur. Ceram. Soc.* **2002**, *22*, 653–660, DOI 10.1016/S0955-2219(01)00382-X.
- [103] H.-J. Choi, K.-M. Lee, G.-H. Kim, J.-G. Lee, “Mechanochemical Synthesis and Electrochemical Properties of  $\text{LiMn}_2\text{O}_4$ ”, *J. Am. Ceram. Soc.* **2001**, *84*, 242–244, DOI 10.1111/j.1151-2916.2001.tb00642.x.
- [104] S.-H. Kang, J. B. Goodenough, L. K. Rabenberg, “Effect of Ball-Milling on 3-V Capacity of Lithium-Manganese Oxospinel Cathodes”, *Chem. Mater.* **2001**, *13*, 1758–1764, DOI 10.1021/cm000920g.
- [105] N. Kamarulzaman, R. Yusoff, N. Kamarudin, N. H. Shaari, N. A. Abdul Aziz, M. A. Bustam, N. Blagojevic, M. Elcombe, M. Blackford, M. Avdeev, A. K. Arof, “Investigation of cell parameters, microstructures and electrochemical behaviour of  $\text{LiMn}_2\text{O}_4$  normal and nano powders”, *J. Power Sources* **2009**, *188*, 274–280, DOI 10.1016/j.jpowsour.2008.10.139.
- [106] D. Chen, S. Ni, G. L. Chen, Z. H. Chen, “Preparation of Nano-Particles of Metal Oxides via a Novel Solid-Liquid Mechanochemical Reaction Technology”, *Adv. Mater. Res.* **2007**, *26-28*, 671–674, DOI 10.4028/www.scientific.net/amr.26-28.671.
- [107] D. Chen, B. Yang, Y. Jiang, Y. Z. Zhang, “Synthesis of  $\text{Mn}_3\text{O}_4$  Nanoparticles for Catalytic Application via Ultrasound-Assisted Ball Milling”, *ChemistrySelect* **2018**, *3*, 3904–3908, DOI 10.1002/slct.201702878.
- [108] A. Y. Fishman, M. Ivanov, S. Petrova, R. G. Zakharov, “Structural Phase Transitions in Mechanoactivated Manganese Oxides”, *Defect Diffus. Forum* **2010**, *297-301*, 1306–1311, DOI 10.4028/www.scientific.net/ddf.297-301.1306.
- [109] A. Y. Fishman, T. E. Kurennykh, V. Y. Mitrofanov, E. A. Pastukhov, S. A. Petrova, S. A. Uporov, V. B. Vykhodets, R. G. Zakharov, “Mechanical Activation of Mn-O Oxides: Structural Phase Transitions, Magnetism and Oxygen Isotope Exchange”, *Diffus. Found.* **2014**, *1*, 175–197, DOI 10.4028/www.scientific.net/df.1.175.

- [110] J. A. Aguilar-garib, F. Sánchez-de-jesús, A. M. Bolarín-miró, S. Ham-hernández, “Synthesis of  $\text{NiMn}_2\text{O}_4$  assisted by high-energy ball milling of NiO-MnO powders”, *J. Ceram. Process. Res.* **2011**, *12*, 721–726.
- [111] W. H. Bragg, W. L. Bragg, “The Reflection of X-rays by Crystals”, *Proc. R. Soc. A Math. Phys. Eng. Sci.* **1913**, *88*, 428–438, DOI 10.1098/rspa.1913.0040.
- [112] A. A. Bunaciu, E. gabriela Udriștioiu, H. Y. Aboul-Enein, “X-Ray Diffraction: Instrumentation and Applications”, *Crit. Rev. Anal. Chem.* **2015**, *45*, 289–299, DOI 10.1080/10408347.2014.949616.
- [113] L. Spieß, R. Schwarzer, H. Behnken, G. Teichert, *Moderne Röntgenbeugung*, Vieweg + Teubner Verlag, Wiesbaden, **2005**, DOI 10.1007/978-3-663-10831-3.
- [114] H. M. Rietveld, “Line profiles of neutron powder-diffraction peaks for structure refinement”, *Acta Crystallogr.* **1967**, *22*, 151–152, DOI 10.1107/S0365110X67000234.
- [115] H. M. Rietveld, “A profile refinement method for nuclear and magnetic structures”, *J. Appl. Crystallogr.* **1969**, *2*, 65–71, DOI 10.1107/S0021889869006558.
- [116] R. A. Young, P. E. Mackie, R. B. Von Dreele, “Application of the Pattern-Fitting Structure-Refinement Method to X-ray Powder Diffractometer Patterns”, *J. Appl. Crystallogr.* **1977**, *10*, 262–269.
- [117] R. J. Hill, C. J. Howard, “Quantitative phase analysis from neutron powder diffraction data using the Rietveld method”, *J. Appl. Crystallogr.* **1987**, *20*, 467–474, DOI 10.1107/S0021889887086199.
- [118] B. H. Toby, “R factors in Rietveld analysis: How good is good enough?”, *Powder Diffr.* **2006**, *21*, 67–70, DOI 10.1154/1.2179804.
- [119] P. Scherrer, “Bestimmung der Größe und der inneren Struktur von Kolloidteilchen mittels Röntgenstrahlen”, *Göttinger Nachrichten* **1918**, *2*, 98–100.
- [120] A. L. Patterson, “The scherrer formula for X-ray particle size determination”, *Phys. Rev.* **1939**, *56*, 978–982, DOI 10.1103/PhysRev.56.978.
- [121] G. K. Williamson, W. H. Hall, “X-Ray broadening from filed aluminium and tungsten”, *Acta Metall.* **1953**, *1*, 22–31.
- [122] L. Alexander, “The synthesis of x-ray spectrometer line profiles with application to crystallite size measurements”, *J. Appl. Phys.* **1954**, *25*, 155–161, DOI 10.1063/1.1721595.
- [123] R. W. Cheary, A. Coelho, “Fundamental parameters approach to x-ray line-profile fitting”, *J. Appl. Crystallogr.* **1992**, *25*, 109–121, DOI 10.1107/S0021889891010804.
- [124] D. Balzar, “Voigt-function model in diffraction line-broadening analysis”, *Microstruct. Anal. from Diffr.* **1999**, *44*, DOI 10.1.1.30.7311.
- [125] Topas 4.2, “General profile and structure analysis software for powder diffraction data”, *Bruker AXS Karlsruhe Ger.* **2009**.

- 
- [126] Topas 5, “General profile and structure analysis software for powder diffraction data”, *Bruker AXS Karlsruhe Ger.* **2014**.
- [127] P. W. Stephens, “Phenomenological model of anisotropic peak broadening in powder diffraction”, *J. Appl. Crystallogr.* **1999**, *32*, 281–289, DOI 10.1107/S0021889898006001.
- [128] D. Ectors, F. Goetz-Neunhoeffler, J. Neubauer, “A generalized geometric approach to anisotropic peak broadening due to domain morphology”, *J. Appl. Crystallogr.* **2015**, *48*, 189–194, DOI 10.1107/S1600576714026557.
- [129] D. Ectors, F. Goetz-Neunhoeffler, J. Neubauer, “Domain size anisotropy in the double-Voigt approach: An extended model”, *J. Appl. Crystallogr.* **2015**, *48*, 1998–2001, DOI 10.1107/S1600576715018488.
- [130] H. P. Beck, M. Douiheche, R. Haberkorn, H. Kohlmann, “Synthesis and characterisation of chloro-vanadato-apatites (M = Ca, Sr, Ba)”, *Solid State Sci.* **2006**, *8*, 64–70, DOI 10.1016/j.solidstatesciences.2005.08.014.
- [131] R. Haberkorn, J. Bauer, G. Kickelbick, “Chemical Sodiation of V<sub>2</sub>O<sub>5</sub> by Na<sub>2</sub>S”, *Zeitschrift für Anorg. und Allg. Chemie* **2014**, *640*, 3197–3202, DOI 10.1002/zaac.201400381.
- [132] J. Bauer, R. Haberkorn, G. Kickelbick, “Chemical redox reactions and extended PXRD-characterization of triphylite-Type compounds  $AM_{0.5}Fe_{0.5}PO_4$  (A = Li, Na; M = Mn, Co)”, *Powder Diffr.* **2017**, *32*, S74–S81, DOI 10.1017/S0885715617000355.



## **Part II     Results and Discussion**



## 6 Mechanochemical Induced Structure Transformations in Lithium Titanates: A Detailed PXRD and $^6\text{Li}$ MAS NMR Study

The aim of this study was to gain a better understanding of the reaction pathway of the mechanochemical syntheses and the mechanism of mechanical induced structure changes in metal oxides. The effects of milling on mixtures of LiOH and  $\text{TiO}_2$  and on monoclinic  $\text{Li}_2\text{TiO}_3$  and cubic spinel  $\text{Li}_4\text{Ti}_5\text{O}_{12}$  were studied systematically. Apart from the expected crystallite size reduction, the formation of cubic  $\text{Li}_2\text{TiO}_3$  was observed in all cases. The mechanochemical synthesis and the mechanical induced structure transformations were studied via PXRD with Rietveld refinement and  $^6\text{Li}$  MAS NMR. The studies were carried out with  $\text{ZrO}_2$  and WC grinding tools to investigate the influence of grinding tool hardness and density. Complete transformations are only achieved by using WC grinding tools because of its higher density.

The mechanochemical synthesis of  $\text{Li}_2\text{TiO}_3$ , from LiOH and  $\text{TiO}_2$ , reveals a formation limit of ca. 70 % cubic  $\text{Li}_2\text{TiO}_3$ . As crystalline side product only  $\text{Li}_2\text{CO}_3$  is observed, which is formed by residual LiOH which reacts with  $\text{CO}_2$  from air. Additionally an amorphous background can be identified. Coupled TG-IR measurements reveal  $\text{CO}_2$  to be the primary factor for the mass loss, indicating that  $\text{TiO}_2$  forms the amorphous background. The thermal stability of the mechanochemically formed cubic  $\text{Li}_2\text{TiO}_3$  is investigated by heating the product in 100 K steps and obtaining ex situ PXRD patterns in each step. The cubic phase is stable up to a temperature of 300 °C. A transformation back to the monoclinic phase takes place and the two phases coexist up to a temperature of 700 °C. The cubic polymorph may also be obtained by milling of monoclinic  $\text{Li}_2\text{TiO}_3$  from a solid state reaction. The transformation is limited if  $\text{ZrO}_2$  grinding tools are used, since  $\text{Li}_2\text{CO}_3$  is formed as a side product. If WC tools are used however, a nearly complete transformation to the cubic polymorph is obtained after just one hour of grinding.  $\text{Li}_4\text{Ti}_5\text{O}_{12}$  behaves similarly. A short milling time induces an asymmetric reflection broadening, which is actually caused by the formation of cubic  $\text{Li}_2\text{TiO}_3$  as a second phase. Longer milling times lead to a decomposition and amorphization, however. Rietveld refinement allows to gain insight into the periodic structure and phase composition of the products, while lithium NMR studies allow to observe the local structure that cannot be directly observed with powder diffraction. The NMR studies suggest a lithium population of interstitial sites with tetrahedral coordination after grinding. This allowed to reiterate the structure model

of cubic  $\text{Li}_2\text{TiO}_3$  and to obtain an improved fit. Impedance spectroscopy measurements allow to derive the electrical and ionic conductivity of the samples. It is shown that slight milling increases the conductivity of monoclinic  $\text{Li}_2\text{TiO}_3$  and spinel  $\text{Li}_4\text{Ti}_5\text{O}_{12}$  from solid-state reactions by several orders of magnitude. Increased milling times however decrease the conductivity again.

In conclusion, cubic  $\text{Li}_2\text{TiO}_3$  is the stable polymorph under the conditions of high energy ball milling since it is formed in a mechanochemical reaction from an educt mixture and also from a mechanical induced transformation of monoclinic  $\text{Li}_2\text{TiO}_3$  and spinel  $\text{Li}_4\text{Ti}_5\text{O}_{12}$ . The formed products reveal very small crystallite sizes and defects in the form of lithium interstitial positions, which is confirmed by the combination of NMR experiments and an appropriate Rietveld refinement model. The electrical and ionic conductivity is increased by the mechanochemical treatment, as shown by impedance spectroscopy.

These results were published in the journal *Inorganics* (MDPI):

D. Becker, R. Haberkorn, G. Kickelbick, Mechanochemical Induced Structure Transformations in Lithium Titanates: A Detailed PXRD and  $^6\text{Li}$  MAS NMR Study. *Inorganics* **2018**, 6(4), 117. DOI:10.3390/inorganics6040117.

Dennis Becker carried out the experimental work, data interpretation and evaluation, and preparation of the original draft of the publication. Robert Haberkorn has contributed with scientific ideas, interpretation and discussions of the results, and editing of the manuscript. Guido Kickelbick has contributed with scientific ideas, interpretation and discussions of the results, and editing of the manuscript.

The publication is reproduced under the terms of the Creative Commons Attribution-NonCommercial License, which permits use, distribution and reproduction in any medium, provided the original work is properly cited and is not used for commercial purposes.

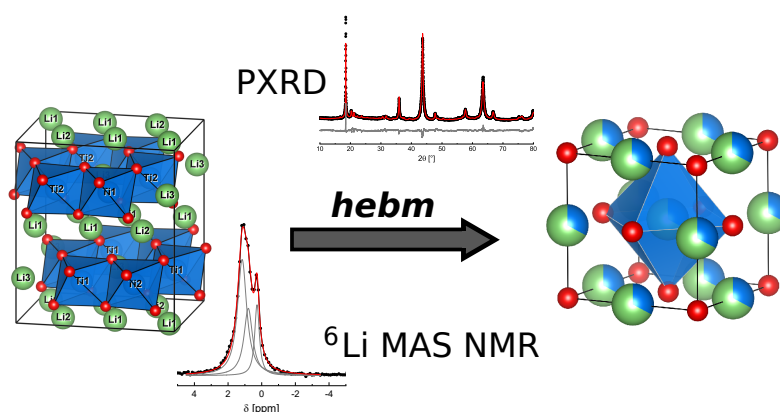


Figure 6.1: Table of contents graphic – Structure transformation of monoclinic  $\text{Li}_2\text{TiO}_3$  to cubic  $\text{Li}_2\text{TiO}_3$ , investigated via  $^6\text{Li}$  MAS NMR and PXRD. DOI:10.3390/inorganics6040117

Article

# Mechanochemical Induced Structure Transformations in Lithium Titanates: A Detailed PXRD and $^6\text{Li}$ MAS NMR Study

Dennis Becker , Robert Haberkorn  and Guido Kickelbick \* 

Inorganic Solid State Chemistry, Saarland University, Campus, Building C 4 1, 66123 Saarbrücken, Germany; dennis.becker@uni-saarland.de (D.B.); haberkorn@mx.uni-saarland.de (R.H.)

\* Correspondence: guido.kickelbick@uni-saarland.de; Tel.: +49-681-302-70651

Received: 30 September 2018; Accepted: 23 October 2018; Published: 27 October 2018



**Abstract:** Lithium titanates are used in various applications, such as anode materials for lithium intercalation ( $\text{Li}_4\text{Ti}_5\text{O}_{12}$ ) or breeding materials in fusion reactors ( $\text{Li}_2\text{TiO}_3$ ). Here, we report the formation of nano-crystalline lithium titanates by a mechanochemical approach and present a deeper insight into their structural characteristics by X-ray diffraction (XRD) and solid-state NMR spectroscopy. The compounds were synthesized in a high-energy planetary ball mill with varying milling parameters and different grinding tools. NaCl type  $\text{Li}_2\text{TiO}_3$  ( $\alpha\text{-Li}_2\text{TiO}_3$ ) was formed by dry milling of lithium hydroxide with titania (rutile or anatase) and by a milling induced structure transformation of monoclinic  $\beta\text{-Li}_2\text{TiO}_3$  or spinel type  $\text{Li}_4\text{Ti}_5\text{O}_{12}$ . Heating of mechanochemical prepared  $\alpha\text{-Li}_2\text{TiO}_3$  induces a phase transformation to the monoclinic phase similar to hydrothermal reaction products, but a higher thermal stability was observed for the mechanochemical formed product. Microstructure and crystallographic structure were characterized by XRD via Rietveld analysis. Detailed phase analysis shows the formation of the cubic phase from the various educts. A set of two lattice parameters for  $\alpha\text{-Li}_2\text{TiO}_3$  was refined, depending on the presence of  $\text{OH}^-$  during the milling process. An average crystallite size of less than 15 nm was observed for the mechanochemical generated products. The local Li environment detected by  $^6\text{Li}$  NMR revealed Li defects in the form of tetrahedral instead of octahedral site occupation. Subsequent adjustment of the structural model for Rietveld refinement leads to better fits, supporting this interpretation.

**Keywords:** lithium titanium oxide; mechanochemistry; high energy ball milling; X-ray diffraction; Rietveld refinement;  $^6\text{Li}$  SPE MAS NMR; impedance spectroscopy

## 1. Introduction

High energy ball milling (*hebm*) is a versatile tool in the synthesis of metal oxides [1]. Beside the formation of oxide phases that can also be produced in other solid-state reactions, such as high temperature or hydrothermal reactions, it is possible to obtain nanocrystalline high-temperature or high-pressure phases, which are not accessible with traditional synthetic techniques. Examples are the formation of a high-pressure polymorph of  $\text{TiO}_2$  starting from anatase or the formation of a  $(\text{Zr}_{1-x}\text{Ti}_x)\text{O}_2$  solid solution [2,3]. The milling process can also be used for a solvent-free surface functionalization of nanocrystallites due to the formation of reactive surfaces during the milling process [4]. Additionally, milling generates defects in the form of oxygen vacancies in anatase, as shown by impedance spectroscopy measurements [5].

$\text{Li}_2\text{TiO}_3$  represents an interesting system for high energy ball milling because of the three known polymorphs that might be converted under the milling conditions depending on the energy impact. The monoclinic low temperature modification  $\beta\text{-Li}_2\text{TiO}_3$  (Figure 1a) with space group  $C2/c$  has a

layered structure with three different lithium sites and two different titanium sites and is isostructural to  $\text{Li}_2\text{SnO}_3$  [6–9]. The cubic high temperature modification  $\gamma\text{-Li}_2\text{TiO}_3$  (Figure 1b) with space group  $Fm\bar{3}m$  consists of a NaCl type structure with statistical distribution of  $\text{Li}^+$  and  $\text{Ti}^{4+}$  on the  $4a$  site and  $Z = 4/3$  formula units per unit cell ( $\text{Li}_{2.66}\text{Ti}_{1.33}\text{O}_4$ ) [7–9]. The  $\beta$  polymorph undergoes a reversible transformation to the  $\gamma$  polymorph at approximately 1150 °C [7,10]. A metastable cubic low temperature form with space group  $Fm\bar{3}m$  is obtained by hydrothermal reactions from  $\text{LiOH}$  and  $\text{TiO}_2$  in water and is denoted as  $\alpha\text{-Li}_2\text{TiO}_3$  [7,11–13]. An irreversible phase transformation from hydrothermally formed  $\alpha\text{-Li}_2\text{TiO}_3$  to  $\beta\text{-Li}_2\text{TiO}_3$  occurs after heating above 300 °C [13–15].

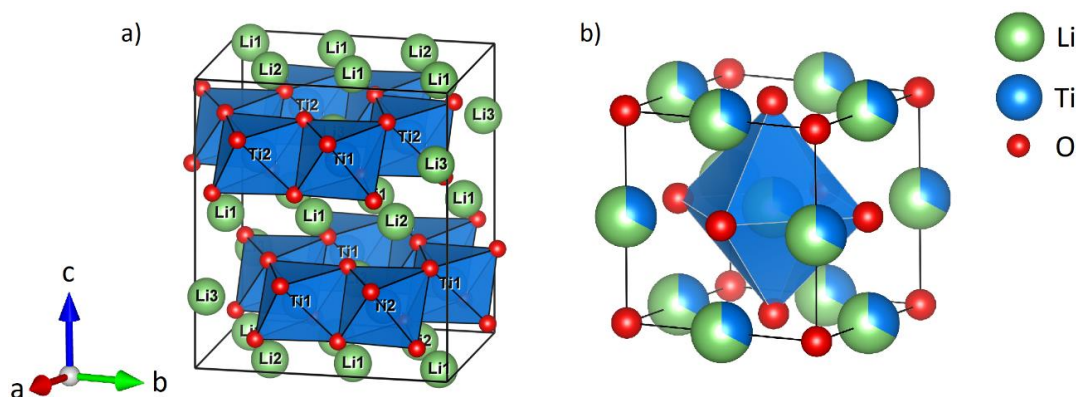


**Figure 1.** Unit cell of monoclinic  $\beta\text{-Li}_2\text{TiO}_3$  (a) and cubic  $\alpha/\gamma\text{-Li}_2\text{TiO}_3$  (b). The green spheres represent lithium, blue titanium and red oxygen. Only polyhedra around titanium (a) or a single octahedra (b) are shown, to emphasize the structural features.

Ball milling of monoclinic  $\beta\text{-Li}_2\text{TiO}_3$  enhances the long-range ion transport, while also inducing a partial transformation to the cubic  $\alpha$  polymorph and amorphization, but neither quantitative conversion nor details of the structural properties or phase compositions after milling have been reported yet [16]. The  $\alpha$  polymorph may also be obtained by milling of  $\text{NaOH}$ ,  $\text{LiCl}$  and  $\text{TiO}_2$ , but subsequent washing to remove  $\text{NaCl}$  is necessary and no structural characterization of the product is given [17]. For  $\text{Li}_4\text{Ti}_5\text{O}_{12}$ , a well-known Li-ion battery anode material, an increase in ion conductivity is reported after milling, but no structure transformation or structural changes by milling have been reported in the literature yet [18].

The goal of our study was the investigation of mechanochemical-induced processes in lithium titanates and the systematic study of process parameters such as milling tools, milling times and milling speed via detailed powder X-ray diffraction (PXRD) Rietveld refinement and  $^6\text{Li}$  single pulse excitation magic angle spinning NMR (SPE MAS NMR) experiments. The mechanochemical induced synthesis of cubic  $\alpha\text{-Li}_2\text{TiO}_3$  from the simple educts  $\text{LiOH}$  and  $\text{TiO}_2$  is reported for the first time and its thermal stability is explored by PXRD. Furthermore, the mechanochemical induced phase transformation of  $\beta$ - to  $\alpha\text{-Li}_2\text{TiO}_3$  is examined by PXRD and additionally by  $^6\text{Li}$  NMR experiments, revealing occupation of tetrahedral sites by lithium. Subsequent modification of the structural model for  $\alpha\text{-Li}_2\text{TiO}_3$  improves the Rietveld refinement. Lastly, PXRD and  $^6\text{Li}$  NMR experiments reveal a strong structural influence on spinel  $\text{Li}_4\text{Ti}_5\text{O}_{12}$  by mechanochemical treatment.

## 2. Results and Discussion

### 2.1. Mechanochemical Formation of $\alpha\text{-Li}_2\text{TiO}_3$ from $\text{LiOH}$ and $\text{TiO}_2$

High energy ball milling of  $\text{LiOH}$  with rutile or anatase as titania precursors in yttrium stabilized zirconia ( $\text{ZrO}_2$ ) and tungsten carbide/cobalt hard metal (WC) tools leads to the formation of new reflections in the X-ray diffractogram which may be indexed by a cubic unit cell, as already noted in a previous study [19]. The new reflections could be assigned to either  $\text{LiTiO}_2$  or  $\text{Li}_2\text{TiO}_3$  with NaCl type

structure (SG  $Fm-3m$ ) and a refined lattice parameter  $a$  varying between 4.15 and 4.16 Å, depending on the reaction conditions. While both compounds have the same structure type, a quantitative reduction of  $Ti^{4+}$  to  $Ti^{3+}$  is required to form  $LiTiO_2$ . This is unlikely under the given conditions, since a reducing agent or oxygen release would be necessary. However, the appearance of very small portions of  $Ti^{3+}$  in  $TiO_2$  has been described as a result of defect formation by mechanochemical methods [20]. The mechanochemical formation of  $LiTiO_2$  has been described before by milling of  $Li_2O$ ,  $TiO_2$  and  $Ti$ , with larger impurities of elemental iron from abrasion of the steel milling tools [21]. Furthermore,  $LiTiO_2$  is black in color [22], while the products of our process are white if  $ZrO_2$  tools are used or gray if WC tools are used. The grey color is based upon abrasion from the WC tools [23]. Hence, the composition of the milling products corresponds to a composition close to  $Li_2TiO_3$  with a mean Ti oxidation state of nearly IV. Due to the additional anatase to high pressure phase transformation [2], milling products of  $LiOH$  and anatase show a complex phase composition. The Rietveld refinement of the milling product from  $ZrO_2$  tools after 6 h of milling at 600 rpm is shown as an example in the Supplementary Materials (Figure S1). The reflections of the high-pressure polymorph  $TiO_2$ -II overlap with the reflections of anatase and  $\alpha$ - $Li_2TiO_3$ . Additionally, milling with anatase as the titania precursor leads to a smaller portion of cubic phase after the same milling conditions.

Based on the reported results we decided to only discuss the rutile ball milling more closely in the following sections. PXRD measurements of  $LiOH$ , rutile and the milling products with different parameters are shown in Figure 2. Decrease of the  $TiO_2$  main reflection and rise of new  $\alpha$ - $Li_2TiO_3$  reflections are marked by yellow rectangles. Formation of  $Li_2CO_3$  (marked by triangles) is caused by unreacted amorphous  $LiOH$  which forms crystalline  $Li_2CO_3$  on contact with air, allowing for quantification by Rietveld refinement.

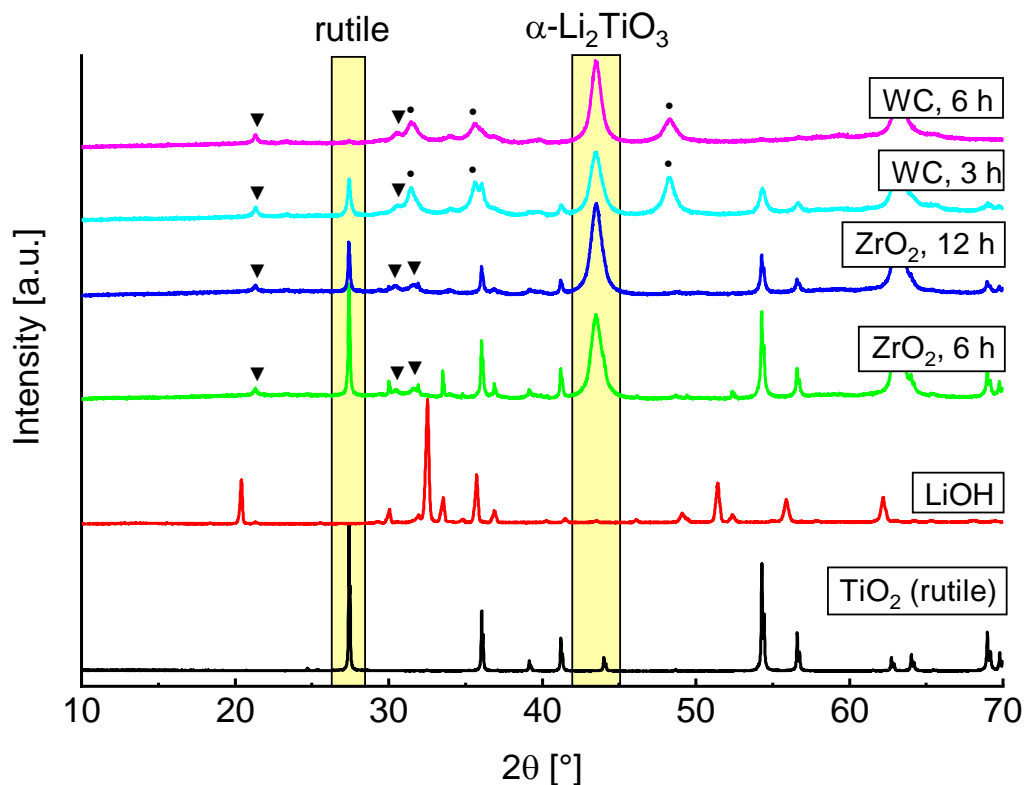


**Figure 2.** PXRD measurements of  $LiOH$  and rutile after different milling conditions. Excess  $LiOH$  forms  $Li_2CO_3$  after the milling process (triangles). WC reflections (circles) arise due to abrasion of the tools.

A faster formation of  $\alpha\text{-Li}_2\text{TiO}_3$  can be observed by use of WC milling tools. Rietveld refinements indicate an introduction of 2 to 4% crystalline WC from abrasion of the tools (marked by circles). After a milling time of 6 h no rutile reflections are visible, while these are still present after 12 h if  $\text{ZrO}_2$  tools are used. This is most likely due to the different hardness of the milling tools and the resulting variations in impact energies. There are already reports in the literature which indicate that the milling tools can have a large influence on the formation of different phases [3,24].

Only results obtained by using WC tools are discussed more closely in the following, since they show a more efficient conversion to cubic  $\text{Li}_2\text{TiO}_3$ . Depending on the milling parameters, the refined structural parameters of the PXRD measurements are slightly different. The lattice parameter  $a$  varies and the crystallite size is in the range of 10 to 15 nm. Since  $\text{OH}^-$  anions are readily available by using  $\text{LiOH}$  in the mechanochemical synthesis, substitution of  $\text{O}^{2-}$  by  $\text{OH}^-$  may be the case to some extent, resulting in a variation of the lattice parameter (4.15–4.16 Å) depending on the degree of substitution. Because only traces of  $\text{H}_2\text{O}$  were found during TG-IR investigation (Supplementary Materials Figures S4 and S5) only a small amount of  $\text{OH}^-$  may be assumed but different  $\text{OH}^-$  contents caused by varying conditions of synthesis account for the different lattice parameters of the as prepared products.

Higher amounts of cubic  $\text{Li}_2\text{TiO}_3$  were only obtained after long milling times or high milling speeds (Figure 3). The cubic phase formed slowly at lower rotational speeds (400 rpm) and even after 24 h a portion of 50% was not exceeded. At high milling speeds (600 rpm) a portion larger than 50% was already achieved after milling for only three hours.

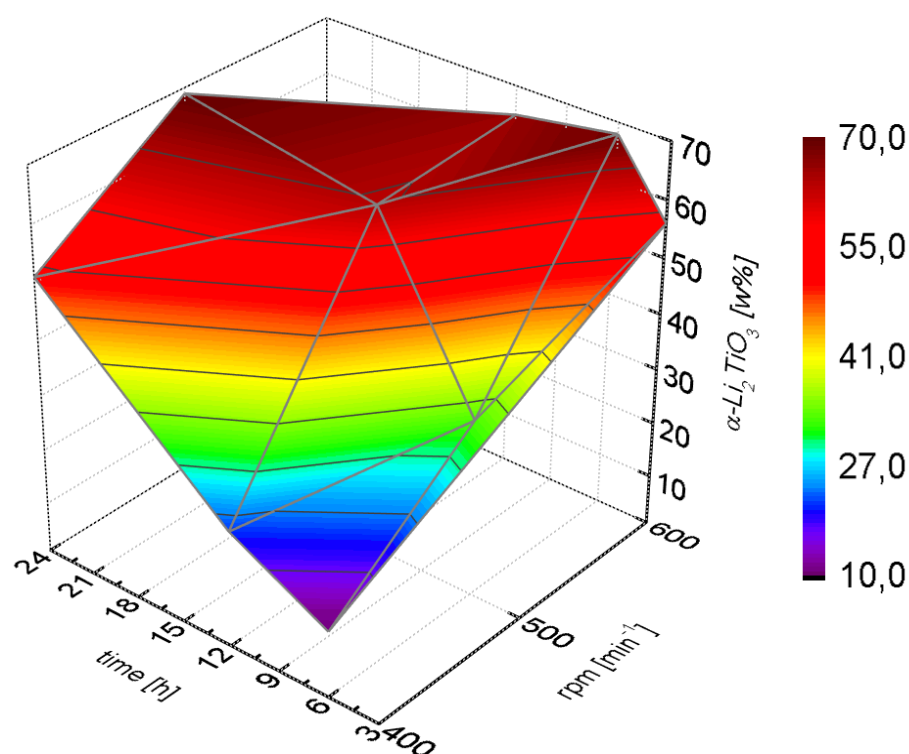


**Figure 3.** Weight portions (from Rietveld refinement) of  $\alpha\text{-Li}_2\text{TiO}_3$  after milling of  $\text{LiOH}$  and rutile in WC tools with different parameters.

The percentage of  $\alpha\text{-Li}_2\text{TiO}_3$  after milling at 600 rpm for 6 h amounts to 68%, as analyzed by Rietveld refinement (Figure 4) neglecting possibly existing amorphous matter. Since  $\text{Li}_2\text{CO}_3$  is still present after complete conversion of  $\text{TiO}_2$  and an increased baseline intensity is visible, a portion of amorphous material may be assumed. Handling of the milling product in a glovebox with subsequent measurement in an airtight dome sample holder (Rietveld refinement in Supplementary Materials

Figure S2) reveals no crystalline phase of LiOH nor Li<sub>2</sub>CO<sub>3</sub>, therefore Li<sub>2</sub>CO<sub>3</sub> is formed after the milling process from the amorphous material by exposure to air. Measurements with an internal standard (50% of  $\alpha$ -Al<sub>2</sub>O<sub>3</sub>) led to the identification of approximately 35% amorphous content, which may contain missing amounts of TiO<sub>2</sub>.

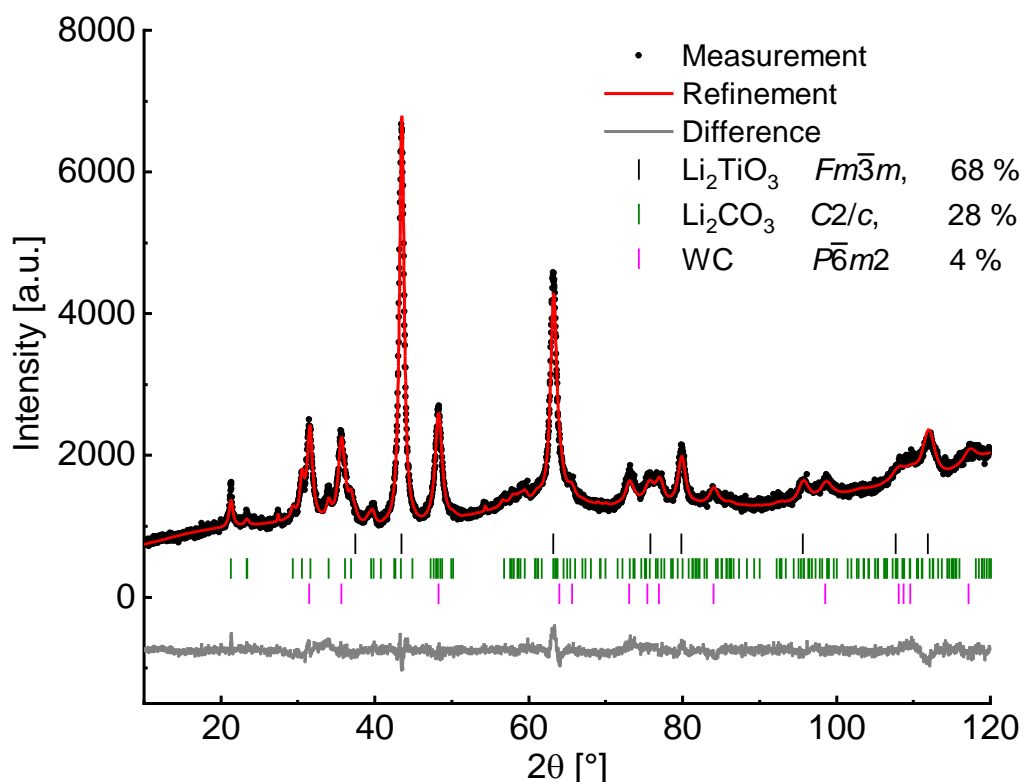


**Figure 4.** Rietveld plot of the milling product from LiOH and rutile (WC tools, 600 rpm, 6h). Li<sub>2</sub>TiO<sub>3</sub> in SG  $Fm\bar{3}m$  with  $a = 4.1588(2) \text{ \AA}$ ,  $V = 71.93(1) \text{ \AA}^3$ , number of reflections = 8 and  $R_{Bragg} = 1.17\%$ . Refinement parameters: number of independent parameters = 40,  $R_{wp} = 3.44\%$ ,  $R_{exp} = 2.60\%$ ,  $GOF = 1.32$ . For more detailed refinement parameters see Supplementary Materials Table S1.

If the amorphous content is assumed to contain the starting composition, the total formula may be written as Li<sub>2-4x</sub>Ti<sub>1+x</sub>O<sub>3</sub> to consider a non-stoichiometry. A formula of Li<sub>1.4</sub>Ti<sub>1.15</sub>O<sub>3</sub> ( $x = 0.15$ ) is necessary to stay in the range of the starting composition with a Li to Ti ratio of 2:1. A constrained refinement of the Li and Ti occupancy on the  $4a$  site of  $\alpha$ -Li<sub>2</sub>TiO<sub>3</sub> also suggests a lithium deficiency. However, to preserve electric neutrality one titanium substitutes four lithium atoms resulting in a small electronic contrast and, accordingly, these refinements rather represent a general tendency and no absolute values. Since Li<sub>2</sub>CO<sub>3</sub> crystallized only after the reaction, the remaining amorphous content may be assumed to be only or mainly TiO<sub>2</sub> in which case a nearly stoichiometric compound with the formula Li<sub>2</sub>TiO<sub>3</sub> would be obtained. Thermogravimetric analysis reveals a mass loss of 16.2% (Supplementary Materials, Figure S4) upon heating to 1000 °C. IR coupling of the gas flow shows primarily characteristic bands of carbon dioxide besides traces of H<sub>2</sub>O (Supplementary Materials, Figure S5), indicating crystalline Li<sub>2</sub>CO<sub>3</sub> as the main fraction responsible for the mass loss. Therefore, the amorphous background is assumed to be primarily TiO<sub>2</sub>.

SEM images (Supplementary Materials, Figure S3) indicate that large agglomerates with a seemingly granular surface were formed in the milling process. The primary grains of the agglomerates that form the surface are visible. The grain size of the primary grains is in the range of 20 nm and is of the same order as the refined crystallite sizes.

2.2. Thermal Transformation of  $\alpha\text{-Li}_2\text{TiO}_3$  to  $\beta\text{-Li}_2\text{TiO}_3$ 

The thermal stability of mechanochemical formed  $\alpha\text{-Li}_2\text{TiO}_3$  (milling of LiOH and rutile in WC tools at 600 rpm for 6 h) was investigated by successive heating in 100 K steps for 1 h and subsequent PXRD measurement at ambient conditions after each step (Figure 5). Between 300 and 500 °C, the formation of a broad reflection in the range around 20° 2 $\theta$  indicates a short-range ordering phenomenon. Since the range in which the reflection is formed coincides with the position of the 002-reflection (18.5°) of  $\beta\text{-Li}_2\text{TiO}_3$ , the broad reflection is probably caused by the nucleation of the monoclinic phase. Sharp reflections of  $\beta\text{-Li}_2\text{TiO}_3$  become evident between 500 and 600 °C. The transformation is completed at temperatures over 700 °C. Compared to the hydrothermal synthesis of  $\alpha\text{-Li}_2\text{TiO}_3$ , sharp reflections of  $\beta\text{-Li}_2\text{TiO}_3$  are visible at 420 °C and the transformation is nearly complete at 500 °C, with only minor amounts of the  $\alpha$ -phase visible (estimated at 12%) [14].

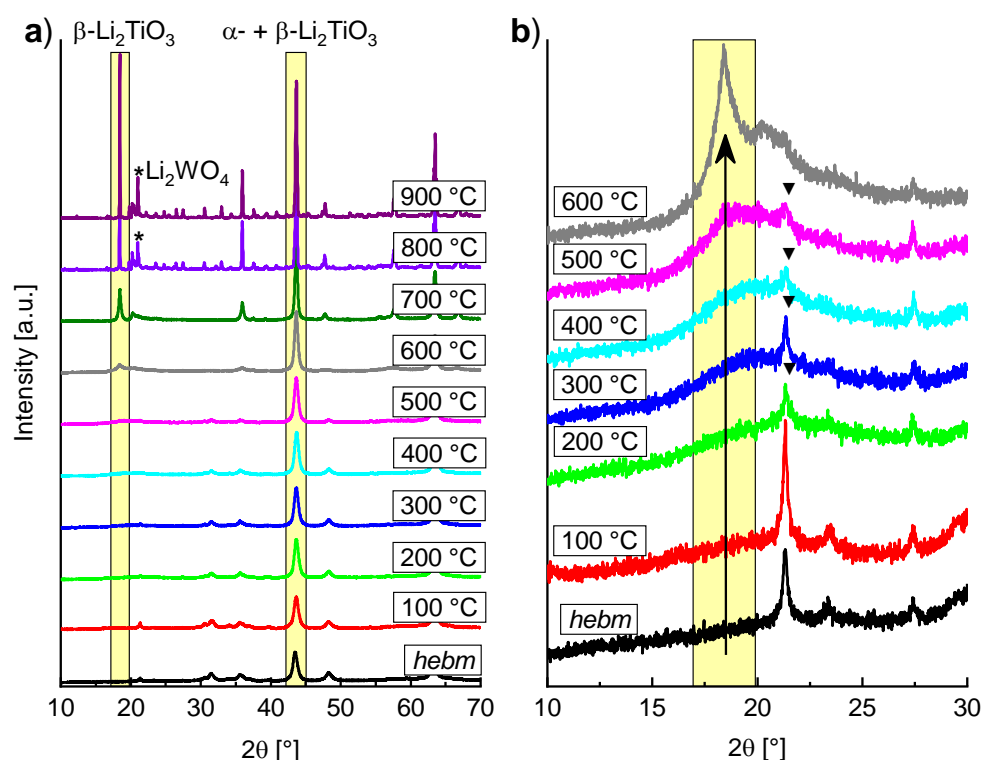


**Figure 5.** PXRD measurements of high energy ball milling (*hebm*)  $\text{Li}_2\text{TiO}_3$  after heating to different temperatures for 1 h. (a) Main reflections of  $\beta$ - and  $\alpha\text{-Li}_2\text{TiO}_3$  are highlighted; (b) The arrow indicates the deployment of the (002) reflection of  $\beta\text{-Li}_2\text{TiO}_3$  between 500 and 600 °C. Triangles indicate the main reflection of  $\text{Li}_2\text{CO}_3$ .

The lattice parameter  $a$  of  $\alpha\text{-Li}_2\text{TiO}_3$  changes from 4.1588(2) to 4.1435(1) Å after heating to 200 °C for 1 h. This may be a consequence of the previously mentioned hypothetical  $\text{OH}^-$  contents in the lattice of an as-prepared  $\alpha\text{-Li}_2\text{TiO}_3$ . Heating induces a transformation of  $\text{OH}^-$  to  $\text{O}^{2-}$  and  $\text{H}_2\text{O}$ , leaving the cubic phase with a smaller lattice parameter. Additionally, a high phase portion of  $\alpha\text{-Li}_2\text{TiO}_3$  has been obtained under these mild conditions, with only 7%  $\text{Li}_2\text{CO}_3$  remaining and without affecting crystallite size of the cubic phase (Rietveld refinement shown in Supplementary Materials, Figure S6).

In the temperature range between 300 °C and 600 °C, a single fraction of  $\beta\text{-Li}_2\text{TiO}_3$  was used in the refinements to estimate the proportion of cubic and monoclinic  $\text{Li}_2\text{TiO}_3$ . Starting with a temperature of 600 °C a three-fraction model for  $\beta\text{-Li}_2\text{TiO}_3$  was used (described under Section 3.4). Increasing amounts of 30 to 90% monoclinic fraction were refined in the temperature range between 300 and 700 °C, while the amount of  $\alpha\text{-Li}_2\text{TiO}_3$  was decreasing. However, up to 500 °C the intensities

of the cubic reflections are hardly affected. This either indicates that the monoclinic ordering arises from byproducts without affecting the cubic structure, or that the ordering takes place continuously. The refined phase portions of  $\alpha$ - $\text{Li}_2\text{TiO}_3$  (cubic)  $\text{Li}_2\text{CO}_3$  and  $\beta$ - $\text{Li}_2\text{TiO}_3$  (monoclinic) are depicted in Figure 6 with the corresponding calcination temperature.

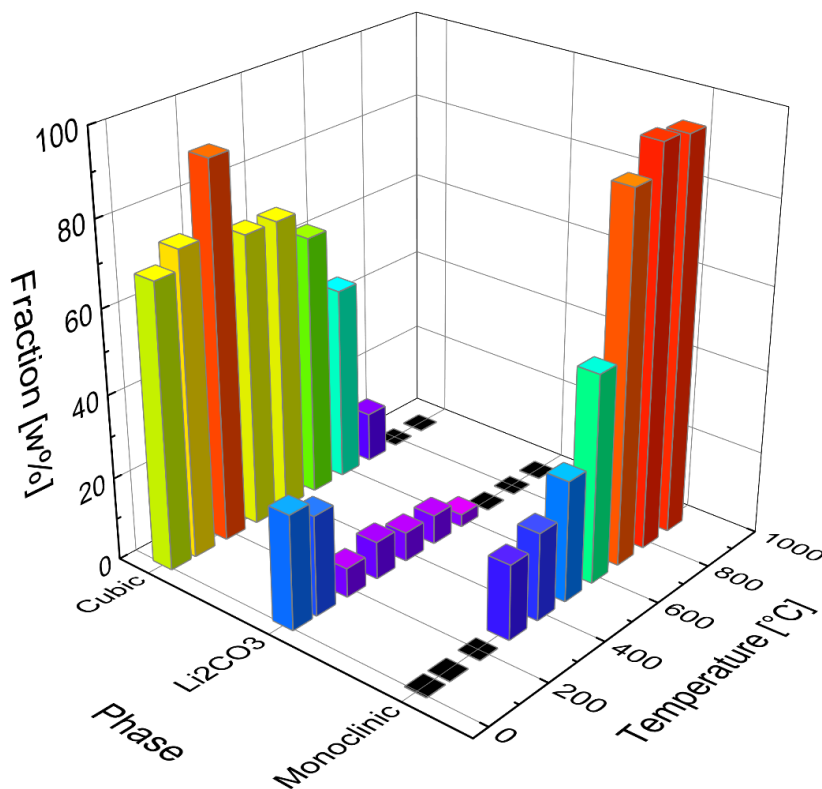


**Figure 6.** Graphical representation of the refined phase portions of  $\alpha$ - $\text{Li}_2\text{TiO}_3$ , (cubic)  $\text{Li}_2\text{CO}_3$  and  $\beta$ - $\text{Li}_2\text{TiO}_3$  (monoclinic) and the corresponding calcination temperature.

Thermogravimetric analysis (Supplementary Materials, Figure S4) between 25 and 1000 °C shows a mass loss up to the temperature range of 575 to 600 °C (attributed to  $\text{Li}_2\text{CO}_3$ ). An exothermic signal arises in the calculated differential thermal analysis (DTA) curve, which correlates to the complete crystallization of  $\beta$ - $\text{Li}_2\text{TiO}_3$  as observed in the PXRD measurements. At 600 °C a composition with equal amounts of  $\alpha$ - and  $\beta$ - $\text{Li}_2\text{TiO}_3$  was refined. Fitting with only the monoclinic phase led to an insufficient refinement ( $GOF = 4.39$ ) while inclusion of the cubic phase results in a greatly improved description ( $GOF = 1.42$ ). At 700 °C an abrupt increase to >90%  $\beta$ - $\text{Li}_2\text{TiO}_3$  occurs, with only minor amounts of the cubic phase remaining. Fitting with only the monoclinic structure results in a similar description ( $GOF = 2.09$ ) as by using both structures ( $GOF = 1.93$ ). Though the improvement of the description is small, this may still be attributed to remaining portions of the cubic phase. This leads to an overall interpretation that an ordering phenomenon takes place in the cubic phase at lower temperatures with a discrete structure change between 600 and 700 °C.

### 2.3. Mechanochemical Induced Phase Transformation of $\beta$ - $\text{Li}_2\text{TiO}_3$ and Spinel $\text{Li}_4\text{Ti}_5\text{O}_{12}$ to $\alpha$ - $\text{Li}_2\text{TiO}_3$

The ball milling-induced phase transformation from  $\beta$ - to  $\alpha$ - $\text{Li}_2\text{TiO}_3$  has already been mentioned by Brandstätter et al. [16], but no further investigation in terms of a quantitative conversion was conducted. In Figure 7, PXRD measurements of  $\beta$ - $\text{Li}_2\text{TiO}_3$  before and after milling with (a)  $\text{ZrO}_2$  tools and (b) WC tools at different parameters are shown. In both cases (a) and (b), a decrease of the  $\beta$ - $\text{Li}_2\text{TiO}_3$  main reflection can be seen. Milling with  $\text{ZrO}_2$  tools at 600 rpm for 6 h leads to portions

of 48%  $\alpha\text{-Li}_2\text{TiO}_3$ , 25%  $\beta\text{-Li}_2\text{TiO}_3$  and 28%  $\text{Li}_2\text{CO}_3$ . Prolonged milling leads to a further increase in intensity of  $\text{Li}_2\text{CO}_3$  reflections. In contrast, the ball milling induced phase transformation is already detectable after milling for 10 min in WC tools. A portion of ca. 30%  $\alpha\text{-Li}_2\text{TiO}_3$  can be fitted, with small amounts of  $\text{Li}_2\text{CO}_3$  (<10%). Even after milling for 1 h, only marginal amounts of ca. 5%  $\beta\text{-Li}_2\text{TiO}_3$  remained. Milling with WC tools leads to complete disappearance of  $\beta\text{-Li}_2\text{TiO}_3$  reflections after 6 h. Portions of 89%  $\alpha\text{-Li}_2\text{TiO}_3$ , 8%  $\text{Li}_2\text{CO}_3$  and 3% WC have been refined (Rietveld refinement in Supplementary Materials, Figure S7). Similar to the mechanochemical synthesis from  $\text{LiOH}$  and rutile, an increase in baseline intensity suggests the formation of amorphous material. Refinement of  $\beta\text{-Li}_2\text{TiO}_3$  (milling in WC tools for 6 h) with an internal standard (50% of  $\alpha\text{-Al}_2\text{O}_3$ ) suggests a portion of 27% amorphous background. In comparison to the mechanochemical synthesis from  $\text{LiOH}$  and rutile in WC tools, a smaller lattice parameter  $a = 4.1463(2)$  Å is refined for  $\alpha\text{-Li}_2\text{TiO}_3$  if  $\beta\text{-Li}_2\text{TiO}_3$  is used as an educt. This may also be a consequence of the previously mentioned hypothetical  $\text{OH}^-$  contents in the lattice. Since no  $\text{OH}^-$  is available in the mechanochemical-induced phase transformation of  $\beta$ - to  $\alpha\text{-Li}_2\text{TiO}_3$ , a lattice parameter similar to the one of  $\alpha\text{-Li}_2\text{TiO}_3$  after heating to 200 °C is refined.

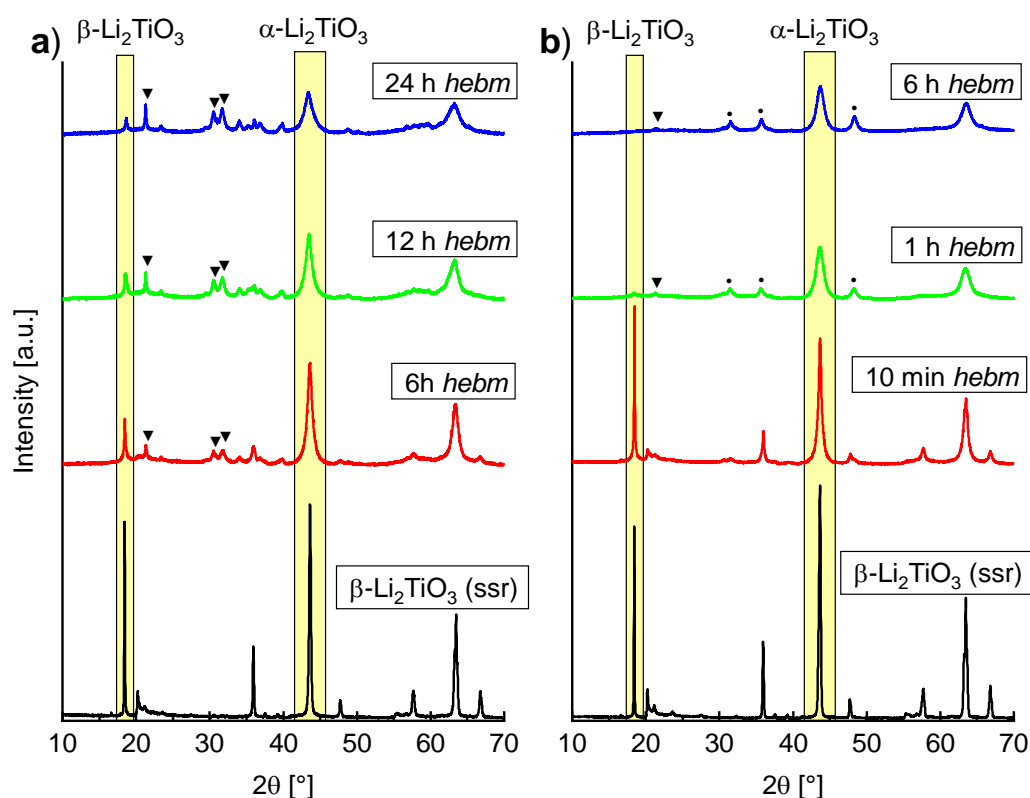


**Figure 7.** PXRD measurements of  $\beta\text{-Li}_2\text{TiO}_3$  after milling in (a)  $\text{ZrO}_2$  and (b) WC tools at 600 rpm after different grinding times. Triangles indicate  $\text{Li}_2\text{CO}_3$ , circles indicate WC.

Formation of  $\alpha\text{-Li}_2\text{TiO}_3$  is also observed by milling of  $\text{Li}_4\text{Ti}_5\text{O}_{12}$  with spinel type structure. PXRD measurements of  $\text{Li}_4\text{Ti}_5\text{O}_{12}$  before and after milling in WC tools at 400 rpm are shown in Figure 8a. After a milling time of 1 h a slight asymmetric broadening of the (400) reflection is visible, while the (111) reflection is not as strongly affected and shows little asymmetry. This is caused by the formation of  $\alpha\text{-Li}_2\text{TiO}_3$  whose reflections overlap with the spinel reflections. In Figure 8b the Bragg intensities of the spinel (400) and the  $\alpha\text{-Li}_2\text{TiO}_3$  (200) reflection are shown with the resulting Rietveld fit. The (111) reflection of the spinel phase vanishes completely after a milling time of 6 h. Though a phase with cubic structure is formed, the intensities are very low and additional unidentified reflections are visible. Even after these mild milling conditions, the structure of the spinel phase is

strongly altered, which may have large impact on the use of mechanochemically treated  $\text{Li}_4\text{Ti}_5\text{O}_{12}$  as anode material in battery applications. It has already been established by impedance spectroscopy that milling of  $\text{Li}_4\text{Ti}_5\text{O}_{12}$  leads to an increase in conductivity [18]. This may be due to this partial structure transformation of spinel  $\text{Li}_4\text{Ti}_5\text{O}_{12}$  to  $\alpha\text{-Li}_2\text{TiO}_3$ .

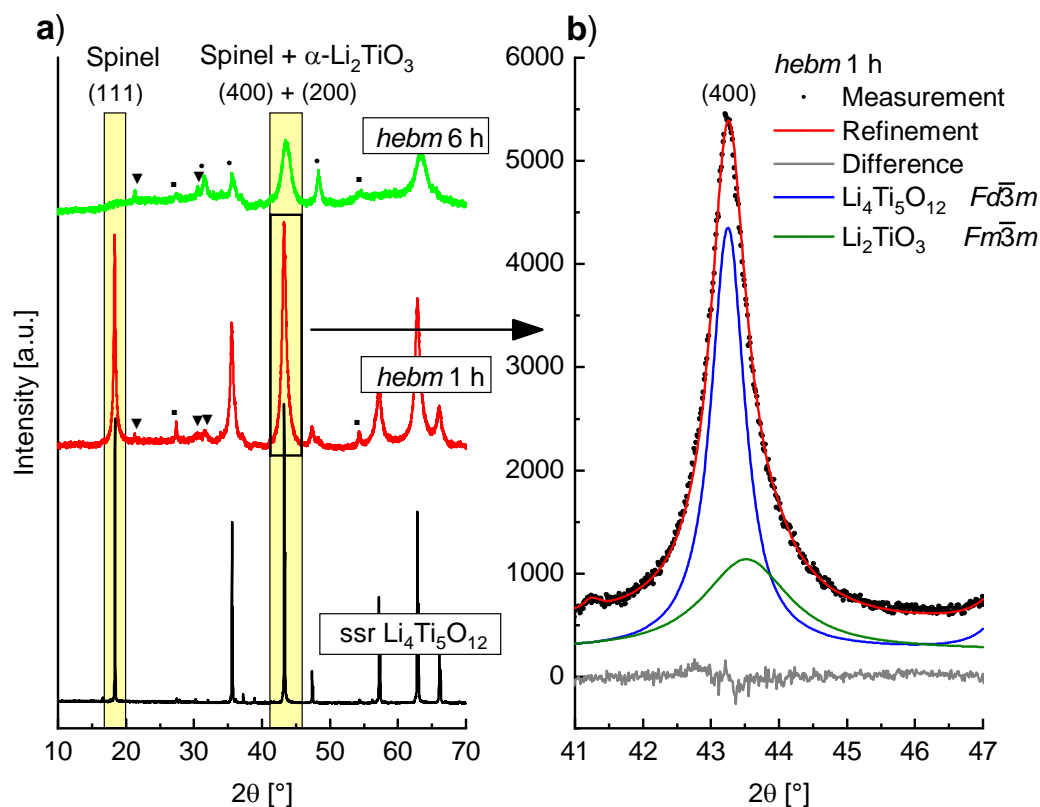


**Figure 8.** (a) PXRD of spinel  $\text{Li}_4\text{Ti}_5\text{O}_{12}$  before and after milling in WC tools at 400 rpm for 1 h and 6 h. Data of  $\text{Li}_4\text{Ti}_5\text{O}_{12}$  were scaled by a factor of 0.5. Triangles indicate  $\text{Li}_2\text{CO}_3$ , squares indicate rutile and circles indicate WC reflections; (b) Enhanced section of the Rietveld plot after milling for 1 h, with fitted portions of spinel (blue) and NaCl type structure (green).

#### 2.4. $^6\text{Li}$ SPE MAS NMR

$^6\text{Li}$  SPE MAS NMR experiments reveal additional insight into the milling-induced structure transformation. To illustrate the following interpretations, the unit cell of spinel  $\text{Li}_4\text{Ti}_5\text{O}_{12}$  is shown in Figure 9. (The unit cell of monoclinic  $\beta\text{-Li}_2\text{TiO}_3$  is shown in Figure 1.)

PXRD refinements of  $900\text{ }^\circ\text{C}$  sintered  $\beta\text{-Li}_2\text{TiO}_3$  with constrained lithium site occupancy factors (total Li content is 2.0 Li per formula unit) show a full occupation of the  $8f$  and  $4d$  site (Li1 and Li2), while the  $4e$  lithium site (Li3) and the two titanium  $4e$  sites (Ti1 and Ti2) show a mixed occupation with 0.6 Li on the Li3 site, 0.3 Li on the Ti1 site and 0.1 Li on the Ti2 site. To obtain a sample with low Li3/Ti1/Ti2 anti-site mixing, several sintering steps at  $1100\text{ }^\circ\text{C}$  were necessary. A mixing of 0.1 Li on the Ti1 site and 0.1 Li on the Ti2 site remained.

The  $^6\text{Li}$  NMR spectrum of  $1100\text{ }^\circ\text{C}$  sintered  $\beta\text{-Li}_2\text{TiO}_3$  is shown in Figure 10a where three signals are visible. Fitting of the line profile was performed with three independent Voigt functions, resulting in shifts of  $\delta = 1.30, 0.80$  and  $0.23$  ppm. The peak at  $0.80$  ppm is attributed to lithium on the  $4e$  site (Li3) in the  $\text{LiTi}_2$  layer, the peak at  $0.23$  ppm originates from the two magnetically equivalent lithium sites  $8f$  (Li1) and  $4d$  (Li2) in the  $\text{Li}_2$  layer [25,26]. The signals are consistent with values reported in the literature if an offset of ca.  $-1$  ppm is considered due to the referencing against solid LiCl [27]. The shift of the third signal matches a tetrahedral coordination of lithium [25]. In Figure 10b the  $^6\text{Li}$

spectrum of spinel  $\text{Li}_4\text{Ti}_5\text{O}_{12}$  is shown.  $\text{Li}_4\text{Ti}_5\text{O}_{12}$  may also be written as  $(\text{Li})[\text{Li}_{0.33}\text{Ti}_{1.66}]\text{O}_4$  to illustrate the occupation of 1 Li on the tetrahedral and  $1/3$  Li on the octahedral position. According to the literature, the peak at 1.32 ppm is attributed to tetrahedrally-coordinated lithium on the  $8a$  site, and the smaller peak at 0.96 ppm to octahedrally-coordinated lithium on the  $16d$  site [28]. Additionally, the NMR spectrum of  $\text{Li}_2\text{CO}_3$  reveals the solely tetrahedrally-coordinated lithium in this compound (Figure 10c). A single shift of 1.16 ppm is observed, which is also in accordance with the literature [28]. Since pristine compounds of  $\beta\text{-Li}_2\text{TiO}_3$  and spinel  $\text{Li}_4\text{Ti}_5\text{O}_{12}$  were yielded by solid state reactions, no  $\text{Li}_2\text{CO}_3$  may be present (confirmed by PXRD measurements). The third signal of  $\beta\text{-Li}_2\text{TiO}_3$  is therefore assigned to lithium on an interstitial position with tetrahedral coordination.

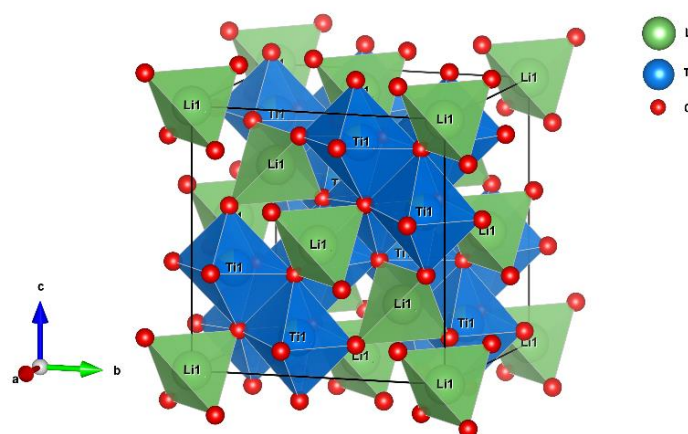


**Figure 9.** Unit cell of spinel  $\text{Li}_4\text{Ti}_5\text{O}_{12}$ . The green spheres represent lithium, blue titanium and red oxygen. The Ti1 position inside the octahedra are occupied by 0.833 Ti and 0.167 Li.

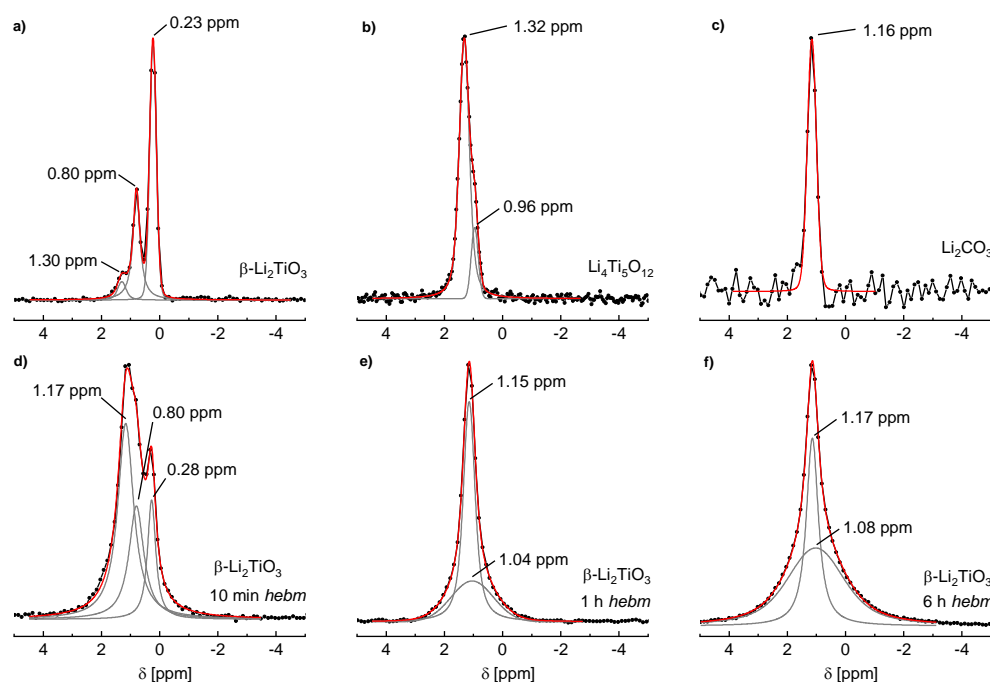


**Figure 10.**  $^6\text{Li}$  SPE MAS NMR spectra of (a)  $\beta\text{-Li}_2\text{TiO}_3$ ; (b) spinel  $\text{Li}_4\text{Ti}_5\text{O}_{12}$ ; (c)  $\text{Li}_2\text{CO}_3$ ; (d)  $\beta\text{-Li}_2\text{TiO}_3$  after *hebm* for 10 min; (e) 1 h and (f) 6 h. All spectra were referenced against solid  $\text{LiCl}$  and fitted with one, two or three independent Voigt functions with  $R^2 > 0.99$ .

The spectrum of  $\beta$ - $\text{Li}_2\text{TiO}_3$  after 10 min of milling is shown in Figure 10d. The signal formerly at  $\delta = 1.30$  ppm is shifted to 1.17 ppm, while the positions of the two other signals are hardly affected. Additionally, the signal intensities of  $\beta$ - $\text{Li}_2\text{TiO}_3$  are strongly altered. The signal at 1.17 ppm indicates that more than half the lithium atoms are tetrahedrally coordinated, while only few remain in octahedral coordination. After 1 h of milling (Figure 10e) only two signals are present. The tetrahedral coordination remains as the dominant state indicated by the sharp line at 1.15 ppm. The band at 1.04 ppm, probably caused by cubic  $\text{Li}_2\text{TiO}_3$  with Li and Ti in octahedral coordination and random ordering, indicates an additional new coordination environment. The signal at 1.15 ppm may be caused by  $\text{Li}_2\text{CO}_3$  that is formed after the milling process. However, PXRD refinements show a portion of only 19%  $\text{Li}_2\text{CO}_3$  after milling for 1 h, while the NMR signal is clearly caused by the main fraction in the sample. The tetrahedral coordination in  $\text{Li}_2\text{TiO}_3$  is therefore assumed to be a transition state for the formation of the cubic state. This new broad signal at ca. 1 ppm becomes the dominant state after milling for 6 h (Figure 10f). The  $^6\text{Li}$  SPE MAS NMR spectrum of  $\text{Li}_2\text{TiO}_3$  from milling of LiOH and rutile (WC tools, 6 h milling time) is nearly identical (not shown). This underlines the assumption that this broad signal is caused by octahedrally-coordinated Li in the cubic phase. Parts of the tetrahedra signal remain. This is most probably caused by occupation of interstitial positions and by  $\text{Li}_2\text{CO}_3$ , but it was not possible to separate the contributions of these two states.

The  $^6\text{Li}$  SPE MAS NMR spectra of  $\text{Li}_4\text{Ti}_5\text{O}_{12}$  (Supplementary Materials, Figure S8) show a slightly different behavior compared to the transformation of  $\beta$ - $\text{Li}_2\text{TiO}_3$ . A broad signal at  $\delta = 1.15$  ppm is visible after milling for 1 h, indicating a purely tetrahedral coordination environment. No signal of an octahedral coordination at ca. 1 ppm is visible. Additionally, a small signal at 1.57 ppm can be distinguished. This signal indicates a very short Li-O bonding distance or a coordination number lower than four. This signal may either be attributed to an interstitial position or the unidentified phase seen in PXRD, but no further identification was possible.

In conclusion to the finding that a tetrahedral coordination environment plays a major role in the structure after mechanochemical treatment, a revised structure model for the Rietveld refinement of  $\alpha$ - $\text{Li}_2\text{TiO}_3$  was constructed. In the ideal NaCl structure model the octahedral 4a site is occupied by 1/3 Ti and 2/3 Li (model A). In the revised model, the tetrahedral 8c site was added and the corresponding site occupancy factors (*sof*) of Li on the 4a site (Li\_O) and 8c site (Li\_T) were refined. To keep the overall stoichiometry of  $\text{Li}_2\text{TiO}_3$ , a constraint refinement in the form [ $\text{sof}(\text{Li}_T) = 1/3 - \frac{1}{2} \cdot \text{sof}(\text{Li}_O)$ ] was defined, while the occupation of Ti was kept constant (model B). The resulting structure parameters are shown in Table 1.

**Table 1.** Structure model for the Rietveld refinement of  $\alpha$ - $\text{Li}_2\text{TiO}_3$  with a mixed Li occupation in octahedral and tetrahedral gaps. Li\_T = tetrahedra gap, Li\_O = octahedra gap, WP = Wyckoff position, *sof* = site occupancy factor.

Site	WP	x	y	z	Atom	sof
Li_T	8c	1/4	1/4	1/4	Li <sup>+</sup>	0.07(1)
Li_O	4a	0	0	0	Li <sup>+</sup>	0.53(1)
	4a	-	-	-	Ti <sup>4+</sup>	0.333
O1	4b	1/2	1/2	1/2	O <sup>2-</sup>	1

As a consequence of this adapted model, the Rietveld refinement of milled  $\beta$ - $\text{Li}_2\text{TiO}_3$  (WC tools, 600 rpm, 6h) is improved. This can be seen particularly in the description of the 022 reflection, which is depicted in Figure 11 with a fit using the (a) standard model A and (b) the adjusted model B. To better accommodate the shape of the amorphous background, a polynomial of 25th degree was used in these both cases, instead of the elsewhere-used polynomial of 15th degree. Both the  $R_{\text{Bragg}}$  value of the  $\text{Li}_2\text{TiO}_3$  phase and the overall fit are improved in model B. The *GOF* is reduced from 1.13 in model A to 1.11 in model B, which is only slightly better but nonetheless indicating an improvement. Beyond that, the  $R_{\text{Bragg}}$  value, which only depends on the agreement between observed and calculated

reflection intensities of the phase, is significantly lowered from 0.60% in model A to 0.28% in model B. However, since Li has a very low X-ray scattering factor the obtained values for the site occupancies in Table 1 are just an indication of an occupation of the tetrahedral site and cannot be regarded as proof. Nevertheless, this model helps to harmonize the results of the Rietveld refinement with the fitted areas of the signals of tetrahedral and octahedral environments in the  $^6\text{Li}$  SPE MAS NMR spectrum of milled  $\beta\text{-Li}_2\text{TiO}_3$  (WC tools, 600 rpm, 6 h). The areas in the  $^6\text{Li}$  spectrum sum up to a proportion of 0.59 to 1 for tetrahedral- and octahedral-coordinated lithium, which corresponds to 37% tetrahedrally-coordinated lithium. The phase fraction from Rietveld refinement with model A (7%  $\text{Li}_2\text{CO}_3$ , 90%  $\alpha\text{-Li}_2\text{TiO}_3$  or 10.2 mol %  $\text{Li}_2\text{CO}_3$  and 88.3 mol %  $\alpha\text{-Li}_2\text{TiO}_3$ ) corresponds to only 10% tetrahedrally coordinated lithium, solely arising from  $\text{Li}_2\text{CO}_3$ . This is far below the 37% from the  $^6\text{Li}$  spectrum. If tetrahedrally-coordinated lithium in  $\alpha\text{-Li}_2\text{TiO}_3$  from model B (6.2%  $\text{Li}_2\text{CO}_3$ , 91.1%  $\alpha\text{-Li}_2\text{TiO}_3$  or 9.0 mol %  $\text{Li}_2\text{CO}_3$  and 89.5 mol %  $\alpha\text{-Li}_2\text{TiO}_3$ ) is factored in, a portion of 30% tetrahedrally-coordinated lithium is obtained, which fits the portion of the Li NMR spectrum. Here, a *sof* of 0.07 for Li on the 8c site (Li\_T) corresponds to 21% of tetrahedrally coordinated lithium in  $\alpha\text{-Li}_2\text{TiO}_3$ .

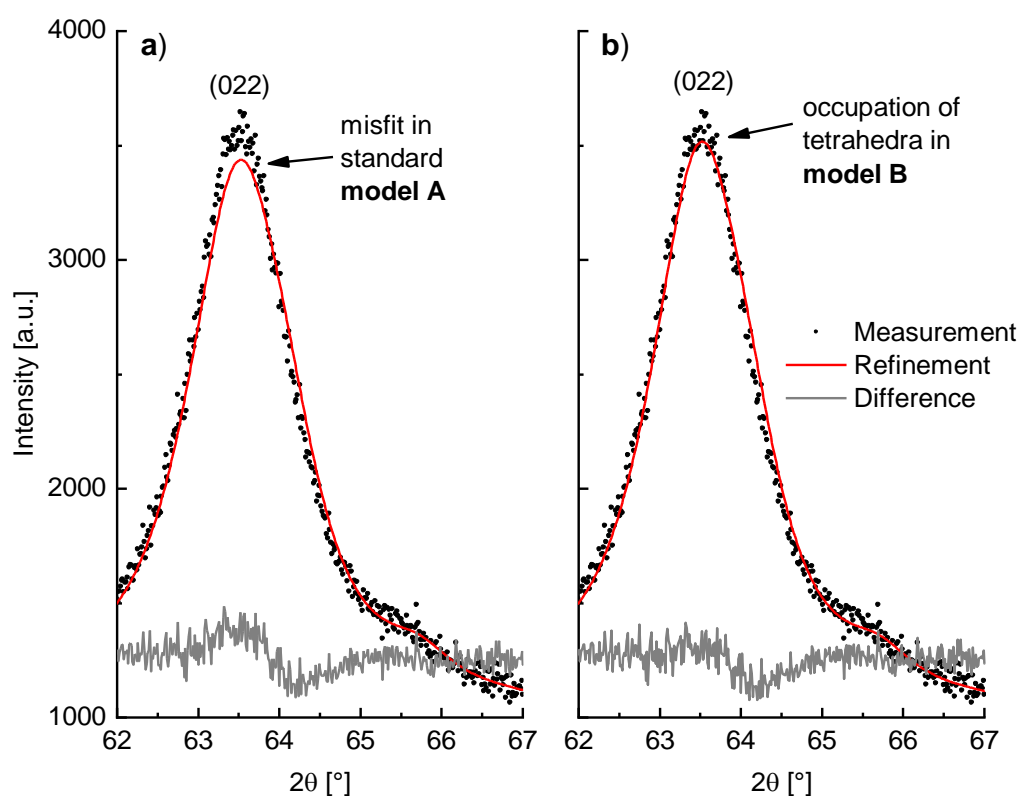


**Figure 11.** Rietveld refinement of milled  $\beta\text{-Li}_2\text{TiO}_3$  (WC tools, 600 rpm, 6 h) with (a) the ideal NaCl structure model and (b) a NaCl structure with mixed Li occupation in octahedra and tetrahedra gaps. Refinement parameters: (a)  $R_{Bragg} = 0.60\%$ ,  $GOF = 1.13$  and (b)  $R_{Bragg} = 0.28\%$ ,  $GOF = 1.11$ .

### 2.5. Impedance Spectroscopy

Since ball milling leads to the formation of defects, structure deformations and amorphization, an influence on the ion conductivity can be expected. The impedance spectra of ball-milled  $\text{Li}_2\text{TiO}_3$  (600 rpm) and  $\text{Li}_4\text{Ti}_5\text{O}_{12}$  (400 rpm) show an increase in conductivity of up to three orders of magnitude. The frequency dependent real part of the conductivity is shown in Figure 12a,b. The spectra were recorded at 298K.

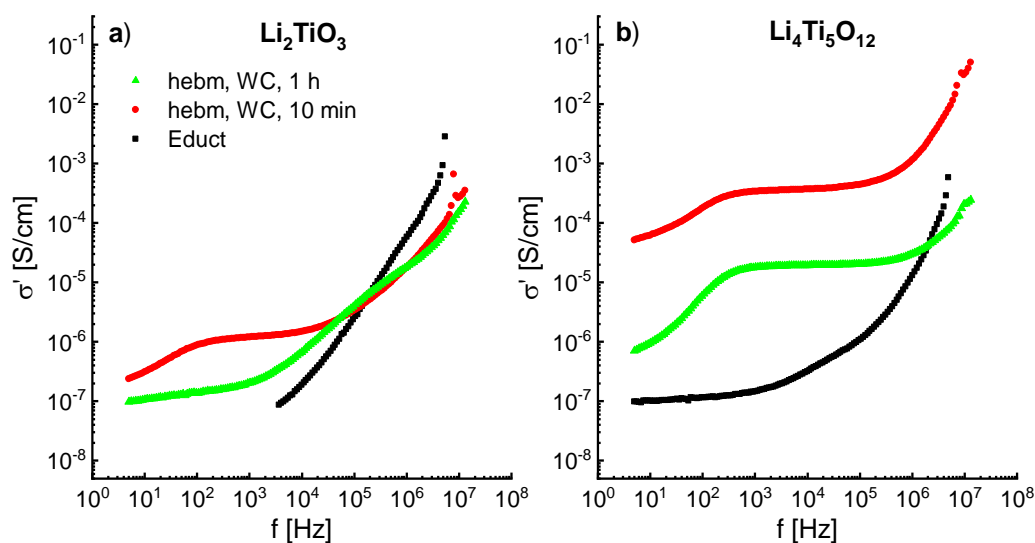


**Figure 12.** Frequency dependent real part of the conductivity at 298K of (a)  $\text{Li}_2\text{TiO}_3$  and (b)  $\text{Li}_4\text{Ti}_5\text{O}_{12}$  before and after milling at (a) 600 rpm and (b) 400 rpm for 10 min and 1 h.

The conductivity of  $\text{Li}_2\text{TiO}_3$  from the solid-state reaction is rather poor and is immeasurable at frequencies below 3 kHz. After milling for 10 min an increase of one order of magnitude can be observed, with a typical dc plateau ( $\sigma_{\text{dc}} \approx 10^{-6}$  S/cm) at lower frequencies and a dispersive regime at higher frequencies. Similar results are shown by Brandstätter et al. [16], however, only a conductivity  $\sigma_{\text{dc}}$  of about  $10^{-9}$  S/cm is reported at room temperature for a milled sample. Milling of  $\text{Li}_2\text{TiO}_3$  for 1 h decreases the conductivity to  $\approx 10^{-7}$  S/cm, indicating a blocking of the Li ion transport. This may be due to the phase transformation from  $\beta$ - to  $\alpha$ - $\text{Li}_2\text{TiO}_3$ . As already shown by  $^6\text{Li}$  MAS NMR in Figure 10, milling for 10 min displaces Li to tetrahedrally-coordinated sites, which may be responsible for the increase in conductivity. Longer milling times promote a new octahedral coordinated state, which may be associated to the decrease in conductivity.

$\text{Li}_4\text{Ti}_5\text{O}_{12}$  shows a similar behavior to  $\text{Li}_2\text{TiO}_3$ , with a dc plateau at lower frequencies and a dispersive region at higher frequencies and a decrease of the conductivity after longer milling times. However,  $\text{Li}_4\text{Ti}_5\text{O}_{12}$  from solid state reaction already exhibits a dc plateau at lower frequencies with  $\sigma_{\text{dc}} \approx 10^{-7}$  S/cm at 298 K. Milling for 10 min increases the conductivity by three orders of magnitude to  $>10^{-4}$  S/cm at 298 K. The observed conductivities are the highest shown yet for ball-milled  $\text{Li}_4\text{Ti}_5\text{O}_{12}$  at room temperature [18].

### 3. Materials and Methods

#### 3.1. Materials

LiOH (Merck, Darmstadt, Germany, 98%),  $\text{Li}_2\text{CO}_3$  (Merck, 99%),  $\text{TiO}_2$  (Anatase, Merck,  $\geq 99\%$  and Rutile, Alfa Aesar GmbH, Karlsruhe, Germany, 99.5%), 2-propanole (Biesterfeld Spezialchemie, 97%) and *n*-pentane (Sigma Aldrich, Steinheim, Germany, 99%) were used as received. All solids have been characterized by PXRD. The used LiOH contained 20%  $\text{LiOH}\cdot\text{H}_2\text{O}$ .

#### 3.2. Sample Preparation

Milling was conducted in a Retsch PM100 planetary ball mill with rotational speeds of 400, 500 and 600 rpm. Milling tools, consisting of yttrium stabilized zirconia ( $\text{ZrO}_2$ ) and tungsten carbide in cobalt matrix (WC) with a volume of 50 mL, as well as 200 milling balls of the same material, with a diameter of 5 mm, were used. The ball to powder weight ratio was 27:1 in case of  $\text{ZrO}_2$  and 60:1 in case of WC tools. Approximately 3 g of starting powder ( $\text{Li}_4\text{Ti}_5\text{O}_{12}$  or  $\beta$ - $\text{Li}_2\text{TiO}_3$ ) were placed in the

grinding jar. To prevent cementing of the powders, 200  $\mu\text{L}$  of 2-propanole were added as dispersing agent. In case of the mechanochemical synthesis from binary oxides, LiOH and  $\text{TiO}_2$  (rutile or anatase) to form 3 g of  $\text{Li}_2\text{TiO}_3$  were deployed. An excess of 10 mol % LiOH was used.

Spinel  $\text{Li}_4\text{Ti}_5\text{O}_{12}$  and  $\beta\text{-Li}_2\text{TiO}_3$  were synthesized by conventional solid-state reactions [6,29]. Appropriate amounts of lithium carbonate and anatase were homogenized by wet ball milling with *n*-pentane at 400 rpm for 1 h. A 50-mL agate grinding jar and twenty agate balls of 10 mm diameter were used. The dried mixtures were heated in a platinum crucible to 900  $^\circ\text{C}$  for 8 h in air atmosphere. The resulting white powders were manually ground in an agate mortar and reheated a second time. To obtain samples of  $\beta\text{-Li}_2\text{TiO}_3$  with higher crystallinity and less Li-Ti-disorder, several heating steps at 1100  $^\circ\text{C}$  were carried out.

### 3.3. Characterization

Powder X-ray diffraction (PXRD) patterns were recorded on a Bruker D8-A25-Advance diffractometer (Bruker, Karlsruhe, Germany) in Bragg–Brentano  $\theta$ – $\theta$ -geometry (goniometer radius 280 mm) with Cu  $K\alpha$ -radiation ( $\lambda = 154.0596$  pm). A 12  $\mu\text{m}$  Ni foil working as  $K\beta$  filter and a variable divergence slit were mounted at the primary beam side. A LYNXEYE detector with 192 channels was used at the secondary beam side. Experiments were carried out in a  $2\theta$  range of 7 to 120 $^\circ$  with a step size of 0.013 $^\circ$  and a total scan time of 2h. Topas 4.2 [30] was used for the Rietveld refinements. Crystallographic structure and microstructure were refined, while instrumental line broadening was included in a fundamental parameters approach [31]. The background was fitted by a Chebychev polynomial function of 15th degree, while fluorescence induced background was reduced by discriminating the detector. Crystal structure data were obtained from the crystallography open database (COD) [32] and inorganic crystal structure database (ICSD).

Thermogravimetric analysis was conducted on a Netzsch TG 209 F1 Iris ASC (Netzsch, Selb, Germany) in alumina crucibles ( $V = 75$   $\mu\text{L}$ ), in a temperature range from 25–1000  $^\circ\text{C}$  under a nitrogen flow of 40  $\text{mL}\cdot\text{min}^{-1}$  with a heating rate of 20  $\text{K}\cdot\text{min}^{-1}$ . The samples were dried in a pre-heating phase at 100  $^\circ\text{C}$  under flowing nitrogen and cooled again before the measurement was started. Coupling of the gas flow to a Bruker Vertex 70 IR spectrometer (Bruker, Karlsruhe, Germany) was achieved with a heated transfer line (200  $^\circ\text{C}$ ) under constant nitrogen flow. Spectra were recorded between 4500 to 600  $\text{cm}^{-1}$  with a resolution of 4  $\text{cm}^{-1}$  and 32 scans per spectrum.

$^6\text{Li}$  single-pulse excitation magic angle spinning (SPE MAS) NMR spectra were recorded on a Bruker AV400WB spectrometer (Bruker, Karlsruhe, Germany) ( $^6\text{Li}$  at 58.91 MHz) at 298K in standard  $\text{ZrO}_2$  rotors ( $d = 4$  mm). A spinning rate of 12 to 13 kHz and a relaxation delay of 3 s were used. Solid LiCl was used as external reference at 0 ppm.

Impedance spectra were recorded on an HP 4192A impedance analyzer (Hewlett-Packard, Palo Alto, CA, USA) in a frequency range of 5 Hz to 13 MHz at 298 K. Data points were recorded via software [33]. The samples were pressed into pellets with 10 mm diameter and a thickness of 1.4–2.1 mm under a uniaxial pressure of 250 MPa at room temperature. Both sides of the pellets were coated with silver conducting paste and dried overnight in air, to establish electrical contact with the platinum electrodes in the measurement cell.

### 3.4. Structural Model for $\beta\text{-Li}_2\text{TiO}_3$ in Rietveld Refinement

As already mentioned in the literature, Rietveld refinement of  $\beta\text{-Li}_2\text{TiO}_3$  requires a more complex structural model than a single well-ordered phase. A mixed occupancy of Li and Ti in the  $\text{LiTi}_2$  layer and different stacking variants must be considered to obtain a satisfactory fit [34]. In our work a three-fraction model [35,36] with a Li-Ti-mixing in the  $\text{LiTi}_2$  layer was used to account for a distribution of different states, but no stacking variants were considered. The parameters of the microstructure of the three fractions were constrained but lattice parameters were refined independently.

#### 4. Conclusions

The cubic polymorph of  $\text{Li}_2\text{TiO}_3$  was successfully synthesized via high energy ball milling of LiOH with rutile,  $\beta\text{-Li}_2\text{TiO}_3$  and spinel  $\text{Li}_4\text{Ti}_5\text{O}_{12}$ . The material of the used milling tools showed a large impact on the composition of the product powders. Use of tungsten carbide (WC) led to full conversion of rutile with LiOH or  $\beta\text{-Li}_2\text{TiO}_3$  to  $\alpha\text{-Li}_2\text{TiO}_3$ . In contrast, the use of yttrium-stabilized zirconia ( $\text{ZrO}_2$ ) did not lead to full conversion, neither of rutile with LiOH nor  $\beta\text{-Li}_2\text{TiO}_3$  regardless of the applied milling conditions. TG-IR coupling of the gas flow showed primarily characteristic bands of  $\text{CO}_2$ , indicating crystalline  $\text{Li}_2\text{CO}_3$  to be mainly responsible for the mass loss upon heating. Therefore, the amorphous background is assumed to primarily consist of  $\text{TiO}_2$ .

Heating under mild conditions (200 °C for 1 h) of the mechanically produced cubic phase caused a phase percentage of 90% cubic phase, without affecting the nano-crystallinity. Further heating resulted in an ordering phenomenon with monoclinic structure at lower temperatures, following a discrete structure change between 600 and 700 °C resulting in a full transformation to  $\beta\text{-Li}_2\text{TiO}_3$ .

Even after mild milling conditions, the structure of spinel  $\text{Li}_4\text{Ti}_5\text{O}_{12}$  is strongly altered, which may have a large impact on the use of mechanochemically treated  $\text{Li}_4\text{Ti}_5\text{O}_{12}$  as anode material. Though a phase with cubic structure was formed, the reflections were very broad and additional unidentified reflections were visible.

$^6\text{Li}$  SPE MAS NMR spectra revealed an extensive rearrangement of the Li environment in  $\beta\text{-Li}_2\text{TiO}_3$  after 10 min of milling. A tetrahedrally coordinated state may be occupied by Li. NMR spectra of the mechanochemically treated spinel  $\text{Li}_4\text{Ti}_5\text{O}_{12}$  indicated a purely tetrahedrally-coordinated environment after milling for 1 h. The process of the milling-induced transformation of the spinel is not completely understood yet. In conclusion to these findings, a revised structure model including a tetrahedral Li site in cubic  $\text{Li}_2\text{TiO}_3$  was tested in Rietveld refinement and resulted in a slightly improved fit.

Impedance spectroscopy measurements at 298K show an increase in conductivity of up to three orders of magnitude after milling for just 10 min. This may be due to the displacement of Li ions to tetrahedrally-coordinated or interstitial sites (as observed by  $^6\text{Li}$  NMR). Longer milling times tend to decrease the conductivity again. These results may be a hint of how to activate anode materials for a faster lithium intercalation.

**Supplementary Materials:** The following are available online at <http://www.mdpi.com/2304-6740/6/4/117/s1>, Figure S1: Rietveld refinement of the milling product from LiOH and anatase, Figure S2: Rietveld refinement of the milling product from LiOH and rutile, Figure S3: SEM photograph of the milling product from LiOH and rutile, Table S1: Refined structure parameters of  $\alpha\text{-Li}_2\text{TiO}_3$  produced by milling of LiOH and rutile, Figure S4: TGA and calculated DTA curve of  $\text{Li}_2\text{TiO}_3$  from milling of LiOH and rutile, Figure S5: Temperature dependent IR signals from coupling of TGA gas flow to IR detector, Figure S6: Rietveld refinement of the milling product from LiOH and rutile, Figure S7: Rietveld refinement of  $\beta\text{-Li}_2\text{TiO}_3$  after ball milling with WC tools for 6 h at 600 rpm, Figure S8:  $^6\text{Li}$  SPE MAS NMR spectra of (a) spinel  $\text{Li}_4\text{Ti}_5\text{O}_{12}$ ; (b) after *hebm* for 1 h.

**Author Contributions:** Conceptualization, D.B., R.H. and G.K.; Methodology and Formal Analysis, D.B. and R.H.; Investigation, D.B.; Resources, G.K.; Writing—Original Draft Preparation, D.B.; Writing—Review & Editing, D.B., R.H., and G.K.; Visualization, D.B.; Supervision, R.H. and G.K.

**Funding:** This research received no external funding.

**Acknowledgments:** We would like to thank Christina Odenwald for recording of the SEM photographs and Michael Zimmer for conducting the NMR experiments and helpful discussion.

**Conflicts of Interest:** The authors declare no conflict of interest.

#### References

1. Fuentes, A.F.; Takacs, L. Preparation of Multicomponent Oxides by Mechanochemical Methods. *J. Mater. Sci.* **2013**, *48*, 598–611. [CrossRef]
2. Chaudhuri, J.; Ram, M.L.; Sarkar, B.K. Observation of a High Pressure Polymorph of Titania by Vibrational Ball Milling. *J. Mater. Sci.* **1994**, *29*, 3484–3488. [CrossRef]

3. Kong, L.; Ma, J.; Zhu, W.; Tan, O. Phase Formation and Thermal Stability of (Zr<sub>1-x</sub>Ti<sub>x</sub>)O<sub>2</sub> Solid Solution via a High-Energy Ball Milling Process. *J. Alloys Compd.* **2002**, *335*, 290–296. [[CrossRef](#)]
4. Fischer, A.; Ney, C.; Kickelbick, G. Synthesis of Surface-Functionalized Titania Particles with Organophosphorus Coupling Agents by Reactive Milling. *Eur. J. Inorg. Chem.* **2013**, *2013*, 5701–5707. [[CrossRef](#)]
5. Amade, R.; Heitjans, P.; Indris, S.; Finger, M.; Haeger, A.; Hesse, D. Defect Formation during High-Energy Ball Milling in TiO<sub>2</sub> and Its Relation to the Photocatalytic Activity. *J. Photochem. Photobiol. A Chem.* **2009**, *207*, 231–235. [[CrossRef](#)]
6. Lang, G. Die Kristallstruktur Einiger Vertreter Der Verbindungsklasse Me<sub>2</sub>Me<sup>IV</sup>O<sub>3</sub> Als Beitrag Zur Aufklärung Der Ordnungsphase von Li<sub>2</sub>TiO<sub>3</sub>. *J. Inorg. Gen. Chem.* **1954**, *276*, 77–94. [[CrossRef](#)]
7. Giquel, C.; Mayer, M.M.; Bouaziz, R.; Champetier, M.G. Sur Quelques Composés Oxygénés Du Titane et Des Alcalins (Li, Na); Étude Des Binaires M<sub>2</sub>O-TiO<sub>2</sub> Dans Les Zones Riches En Oxyde Alcalin. *C. R. Acad. Sc. Paris* **1972**, *275*, 1427–1430.
8. Mikkelsen, J.C. Pseudobinary Phase Relations of Li<sub>2</sub>Ti<sub>3</sub>O<sub>7</sub>. *J. Am. Ceram. Soc.* **1980**, *63*, 331–335. [[CrossRef](#)]
9. Kleykamp, H. Phase Equilibria in the Li–Ti–O System and Physical Properties of Li<sub>2</sub>TiO<sub>3</sub>. *Fusion Eng. Des.* **2002**, *61–62*, 361–366. [[CrossRef](#)]
10. Kleykamp, H. Enthalpy, Heat Capacity and Enthalpy of Transformation of Li<sub>2</sub>TiO<sub>3</sub>. *J. Nucl. Mater.* **2001**, *295*, 244–248. [[CrossRef](#)]
11. Tomiha, M.; Masaki, N.; Uchida, S.; Sato, T. Hydrothermal Synthesis of Alkali Titanates from Nano Size Titania Powder. *J. Mater. Sci.* **2002**, *37*, 2341–2344. [[CrossRef](#)]
12. Song, H.; Jiang, H.; Liu, T.; Liu, X.; Meng, G. Preparation and Photocatalytic Activity of Alkali Titanate Nano Materials A<sub>2</sub>Ti<sub>n</sub>O<sub>2n+1</sub> (A = Li, Na and K). *Mater. Res. Bull.* **2007**, *42*, 334–344. [[CrossRef](#)]
13. Laumann, A.; Fehr, K.T.; Wachsmann, M.; Holzapfel, M.; Iversen, B.B. Metastable Formation of Low Temperature Cubic Li<sub>2</sub>TiO<sub>3</sub> under Hydrothermal Conditions—Its Stability and Structural Properties. *Solid State Ionics* **2010**, *181*, 1525–1529. [[CrossRef](#)]
14. Laumann, A.; Ørnsbjerg Jensen, K.M.; Tyrsted, C.; Bremholm, M.; Fehr, K.T.; Holzapfel, M.; Iversen, B.B. In-Situ Synchrotron X-Ray Diffraction Study of the Formation of Cubic Li<sub>2</sub>TiO<sub>3</sub> Under Hydrothermal Conditions. *Eur. J. Inorg. Chem.* **2011**, *2011*, 2221–2226. [[CrossRef](#)]
15. Laumann, A.; Fehr, K.T.; Boysen, H.; Hölzel, M.; Holzapfel, M. Temperature-Dependent Structural Transformations of Hydrothermally Synthesized Cubic Li<sub>2</sub>TiO<sub>3</sub> Studied by in-Situ Neutron Diffraction. *Zeitschrift für Kristallographie Crystalline Materials* **2011**, *226*, 53–61. [[CrossRef](#)]
16. Brandstätter, H.; Wohlmuth, D.; Bottke, P.; Pregartner, V.; Wilkening, M. Li Ion Dynamics in Nanocrystalline and Structurally Disordered Li<sub>2</sub>TiO<sub>3</sub>. *Z. Phys. Chem.* **2015**, *229*, 1363–1374. [[CrossRef](#)]
17. Carbajal-Ramos, I.A.; Andrade-Gamboa, J.J.; Condó, A.M.; Gennari, F.C. Formation of Cubic Li<sub>2</sub>TiO<sub>3</sub> by Mechanical Activation and Its Transformation to Monoclinic Phase: Stability in Helium and Hydrogen Flows. *Solid State Ionics* **2017**, *308*, 46–53. [[CrossRef](#)]
18. Iwaniak, W.; Fritzsche, J.; Zukalová, M.; Winter, R.; Wilkening, M.; Heitjans, P. Li Conductivity of Nanocrystalline Li<sub>4</sub>Ti<sub>5</sub>O<sub>12</sub> Prepared by a Sol-Gel Method and High-Energy Ball Milling. *Defect Diffus. Forum* **2009**, *289–292*, 565–570. [[CrossRef](#)]
19. Becker, D.; Haberkorn, R.; Kickelbick, G. Mechanochemical Synthesis of Cubic Li<sub>2</sub>TiO<sub>3</sub>. *Zeitschrift für Kristallographie Supplements* **2017**, *37*, P178.
20. Indris, S.; Amade, R.; Heitjans, P.; Finger, M.; Haeger, A.; Hesse, D.; Grünert, W.; Börger, A.; Becker, K.D. Preparation by High-Energy Milling, Characterization, and Catalytic Properties of Nanocrystalline TiO<sub>2</sub>. *J. Phys. Chem. B* **2005**, *109*, 23274–23278. [[CrossRef](#)] [[PubMed](#)]
21. Obrovac, M. Structure and Electrochemistry of LiMO<sub>2</sub> (M = Ti, Mn, Fe, Co, Ni) Prepared by Mechanochemical Synthesis. *Solid State Ionics* **1998**, *112*, 9–19. [[CrossRef](#)]
22. Jiang, K.; Hu, X.; Sun, H.; Wang, D.; Jin, X.; Ren, Y.; Chen, G.Z. Electrochemical Synthesis of LiTiO<sub>2</sub> and LiTi<sub>2</sub>O<sub>4</sub> in Molten LiCl. *Chem. Mater.* **2004**, *16*, 4324–4329. [[CrossRef](#)]
23. Betke, A.; Kickelbick, G. Important Reaction Parameters in the Synthesis of Phenylphosphonic Acid Functionalized Titania Particles by Reactive Milling. *New J. Chem.* **2014**, *38*, 1264–1270. [[CrossRef](#)]
24. Gajovic, A.; Furic, K.; Music, S.; Djerdj, I.; Tonejc, A.; Tonejc, A.M.; Su, D.; Schlogl, R. Mechanism of ZrTiO<sub>4</sub> Synthesis by Mechanochemical Processing of TiO<sub>2</sub> and ZrO<sub>2</sub>. *J. Am. Ceram. Soc.* **2006**, *89*, 2196–2205. [[CrossRef](#)]

25. Vijayakumar, M.; Kerisit, S.; Yang, Z.; Graff, G.L.; Liu, J.; Sears, J.A.; Burton, S.D.; Rosso, K.M.; Hu, J. Combined  $^{6,7}\text{Li}$  NMR and Molecular Dynamics Study of Li Diffusion in  $\text{Li}_2\text{TiO}_3$ . *J. Phys. Chem. C* **2009**, *113*, 20108–20116. [[CrossRef](#)]
26. Baklanova, Y.V.; Arapova, I.Y.; Shein, I.R.; Maksimova, L.G.; Mikhalev, K.N.; Denisova, T.A. Charge Distribution and Mobility of Lithium Ions in  $\text{Li}_2\text{TiO}_3$  from  $^{6,7}\text{Li}$  NMR Data. *J. Struct. Chem.* **2013**, *54* (Suppl. 1), 111–118. [[CrossRef](#)]
27. Xu, Z.; Stebbins, J.F.  $^6\text{Li}$  Nuclear Magnetic Resonance Chemical Shifts, Coordination Number and Relaxation in Crystalline and Glassy Silicates. *Solid State Nucl. Magn. Reson.* **1995**, *5*, 103–112. [[CrossRef](#)]
28. Kartha, J.P.; Tunstall, D.P.; Irvine, J.T.S. An NMR Investigation of Lithium Occupancy of Different Sites in the Oxide Superconductor  $\text{LiTi}_2\text{O}_4$  and Related Compounds. *J. Solid State Chem.* **2000**, *152*, 397–402. [[CrossRef](#)]
29. Leonidov, I.A.; Leonidova, O.N.; Perelyaeva, L.A.; Samigullina, R.F.; Kovyazina, S.A.; Patrakeeve, M.V. Structure, Ionic Conduction, and Phase Transformations in Lithium Titanate  $\text{Li}_4\text{Ti}_5\text{O}_{12}$ . *Phys. Solid State* **2003**, *45*, 2183–2188. [[CrossRef](#)]
30. Bruker, A.X.; Topas, V. *General Profile and Structure Analysis Software for Powder Diffraction Data*; Bruker AXS: Karlsruhe, Germany, 2009.
31. Cheary, R.W.; Coelho, A.A.; Cline, J.P. Fundamental Parameters Line Profile Fitting in Laboratory Diffractometers. *J. Res. Natl. Inst. Stand. Technol.* **2004**, *109*, 1–25. [[CrossRef](#)] [[PubMed](#)]
32. Gražulis, S.; Chateigner, D.; Downs, R.T.; Yokochi, A.F.T.; Quirós, M.; Lutterotti, L.; Manakova, E.; Butkus, J.; Moeck, P.; Le Bail, A. Crystallography Open Database — An Open-Access Collection of Crystal Structures. *J. Appl. Crystallogr.* **2009**, *42*, 726–729. [[CrossRef](#)] [[PubMed](#)]
33. Lüke, H. *HPLueke Version 2—A Program for Running an HP 4192A Impedance Analyzer*; Marl, Germany, 2016.
34. Tarakina, N.V.; Neder, R.B.; Denisova, T.A.; Maksimova, L.G.; Baklanova, Y.V.; Tyutyunnik, A.P.; Zubkov, V.G. Defect Crystal Structure of New  $\text{TiO}(\text{OH})_2$  Hydroxide and Related Lithium Salt  $\text{Li}_2\text{TiO}_3$ . *Dalton Trans.* **2010**, *39*, 8168. [[CrossRef](#)] [[PubMed](#)]
35. Beck, H.P.; Douiheche, M.; Haberkorn, R.; Kohlmann, H. Synthesis and Characterisation of Chloro-Vanadato-Apatites  $M_5(\text{VO}_4)_3\text{Cl}$  ( $M = \text{Ca}, \text{Sr}, \text{Ba}$ ). *Solid State Sci.* **2006**, *8*, 64–70. [[CrossRef](#)]
36. Haberkorn, R.; Bauer, J.; Kickelbick, G. Chemical Sodiation of  $\text{V}_2\text{O}_5$  by  $\text{Na}_2\text{S}$ . *Z. Anorg. Allg. Chem.* **2014**, *640*, 3197–3202. [[CrossRef](#)]



© 2018 by the authors. Licensee MDPI, Basel, Switzerland. This article is an open access article distributed under the terms and conditions of the Creative Commons Attribution (CC BY) license (<http://creativecommons.org/licenses/by/4.0/>).

## Supplementary Materials: Mechanochemical Induced Structure Transformations in Lithium Titanates: A Detailed PXRD and $^6\text{Li}$ MAS NMR Study

Dennis Becker, Robert Haberkorn and Guido Kickelbick

### Formation of $\alpha\text{-Li}_2\text{TiO}_3$ from $\text{LiOH}$ and $\text{TiO}_2$

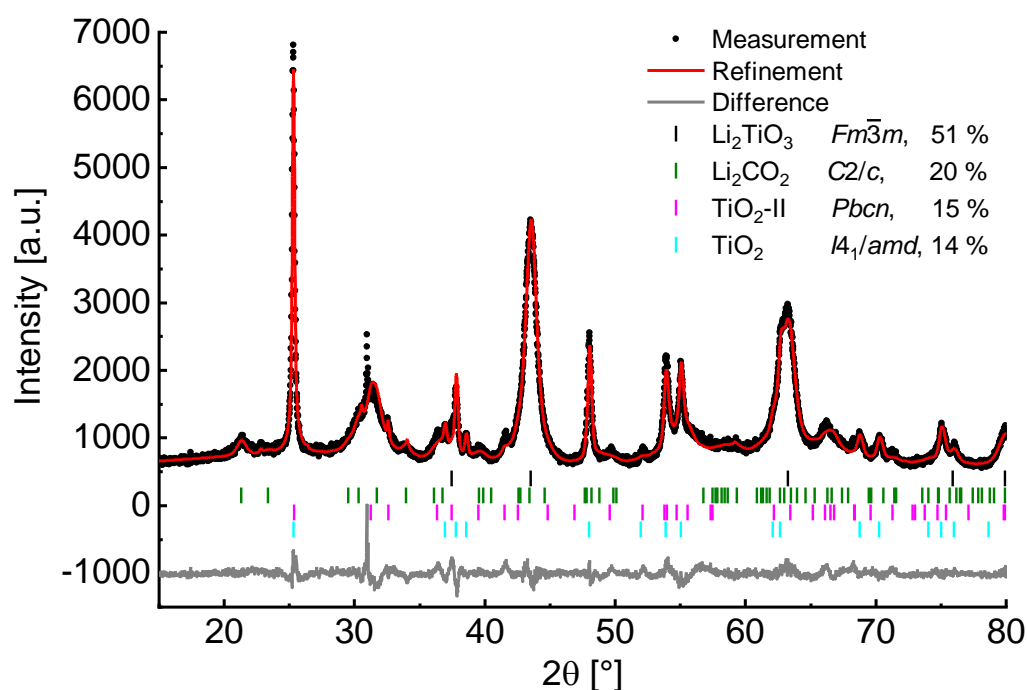


**Figure S1:** Rietveld refinement of the milling product from  $\text{LiOH}$  and anatase ( $\text{ZrO}_2$  tools, 600 rpm, 6h).  $\text{Li}_2\text{TiO}_3$  in SG  $Fm\bar{3}m$  with  $a = 4.1555(2) \text{ \AA}$ ,  $V = 71.76(1) \text{ \AA}^3$ , number of reflections = 8 and  $R_{\text{Bragg}} = 0.99\%$ . Refinement parameters: number of independent parameters = 46,  $R_{\text{wp}} = 5.41\%$ ,  $R_{\text{exp}} = 3.30\%$ ,  $GOF = 1.64$ .

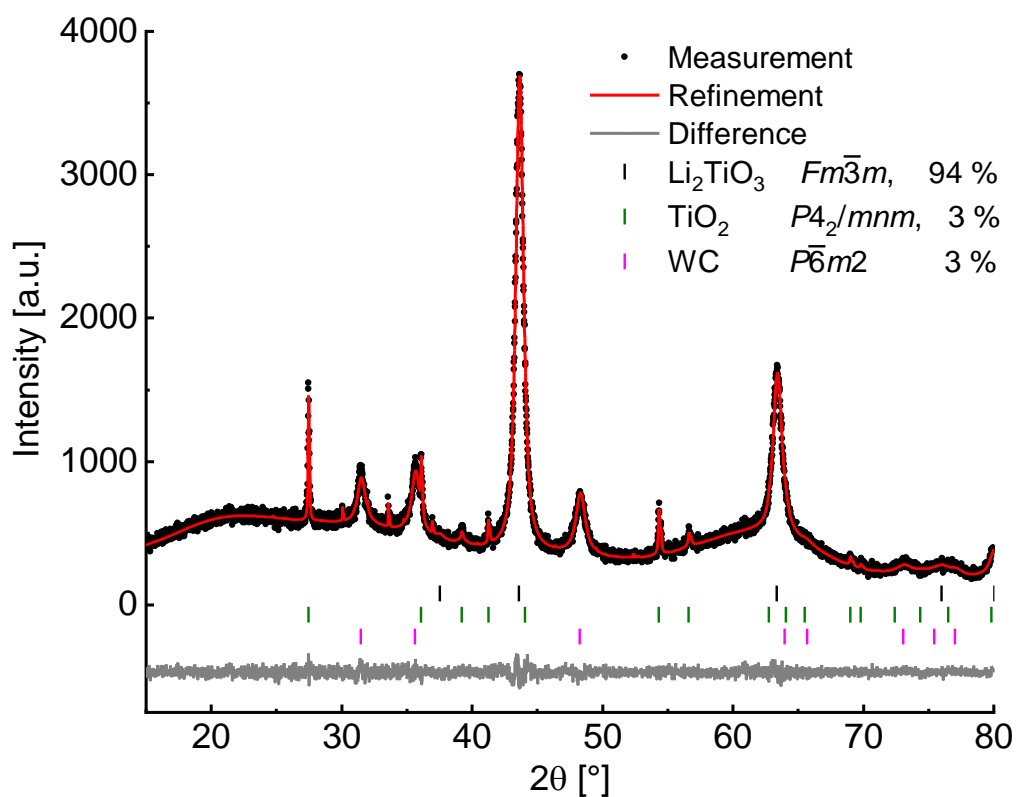


**Figure S2:** Rietveld refinement of the milling product from LiOH and rutile (WC tools, 600 rpm, 6h) after handling in the glovebox. Measurement was conducted with an air-tight dome sample holder (responsible for the background signal). The small percentage of crystalline  $\text{TiO}_2$  is due to a small unreacted residue between milling vial and lid.

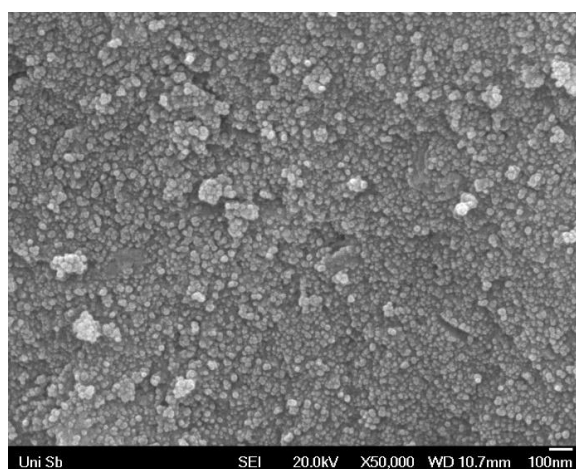
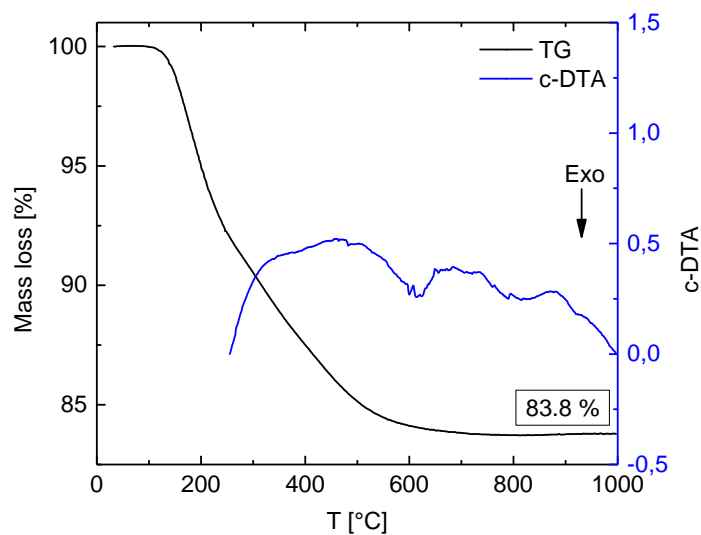


**Figure S3:** SEM photograph of the milling product from LiOH and rutile in WC tools at 600 rpm and 6h.

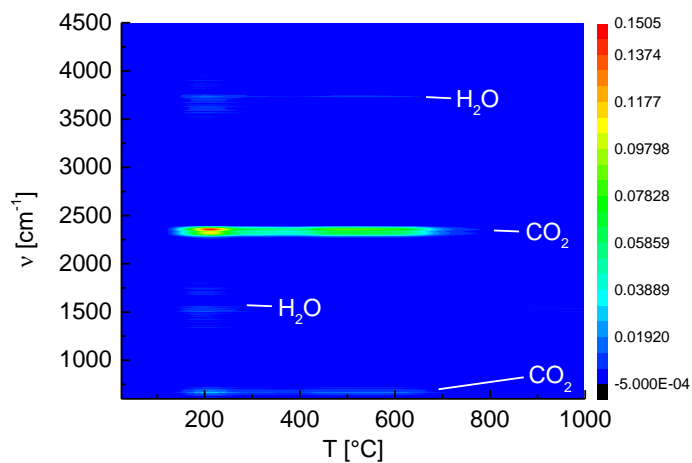
**Table S1:** Refined structure parameters of  $\alpha\text{-Li}_2\text{TiO}_3$  produced by milling of LiOH and rutile in WC tools at 600 rpm for 6 h.  $B_{iso}$  was constrained at the same value for all atoms in the refinement. Global refinement parameters: number of independent parameters = 40,  $R_{wp}$  = 3.44%,  $R_{exp}$  = 2.60%,  $GOF$  = 1.32.  $WP$  = Wyckoff position,  $sof$  = site occupancy factor.

SG	$Fm\bar{3}m$						
$R_{Bragg}$	1.17%						
No. of reflections	8						
Wt% Rietveld	68.3(4)						
Cell Mass	150.6(5)						
Cell Volume [ $\text{\AA}^3$ ]	71.93(1)						
Lattice Parameter [ $\text{\AA}$ ]	4.1588(2)						
Crystallite Size $L_{vol-IB}$ [nm]	15.7(4)						
Strain $e_0$	0.18742						
Lin. Abs. Coeff. [ $\text{cm}^{-1}$ ]	358(4)						
Crystal Density [ $\text{g/cm}^3$ ]	3.48(1)						
Site	$WP$	$x$	$y$	$z$	Atom	$sof$	$B_{iso}$
Li1	$4a$	0	0	0	$\text{Li}^+$	0.46(2)	1.34(2)
	$4a$				$\text{Ti}^{4+}$	0.39(6)	1.34(2)
O1	$4b$	1/2	1/2	1/2	$\text{O}^{2-}$	1	1.34(2)

## Thermogravimetric analysis

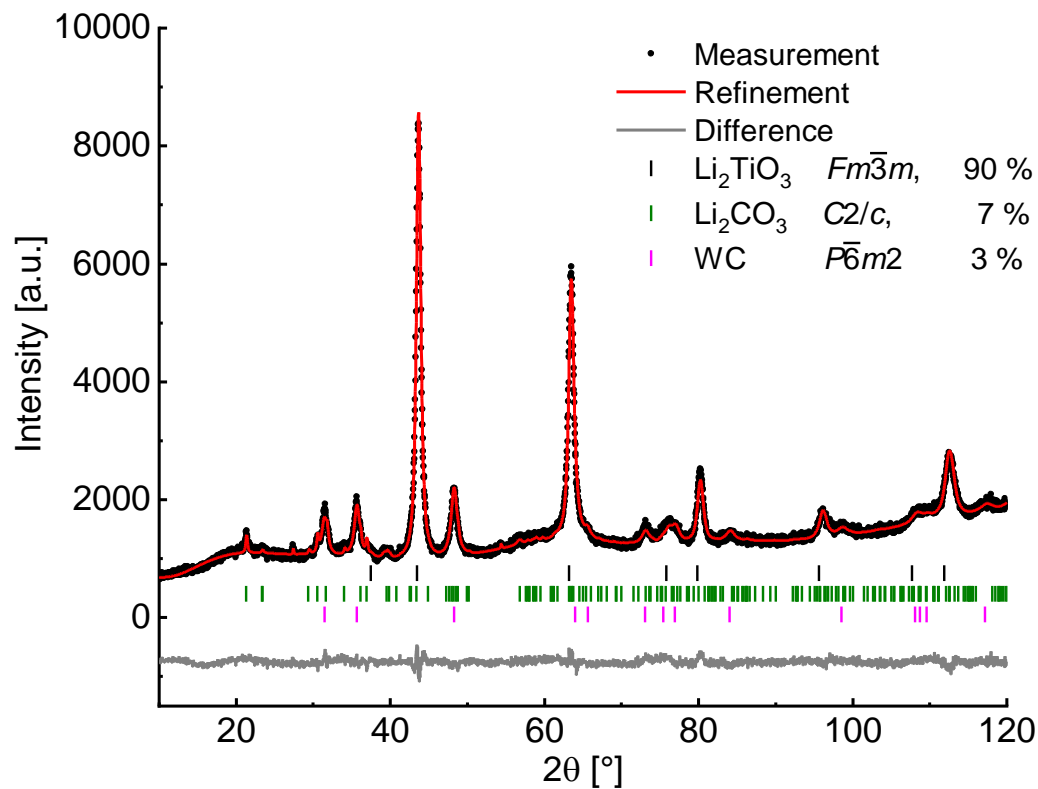


**Figure S4:** TGA and calculated DTA curve of  $\text{Li}_2\text{TiO}_3$  from milling of  $\text{LiOH}$  and rutile in WC tools at 600 rpm for 6 h. Intermediate drying in  $\text{N}_2$  atmosphere at 100 °C led to mass loss of 3%.

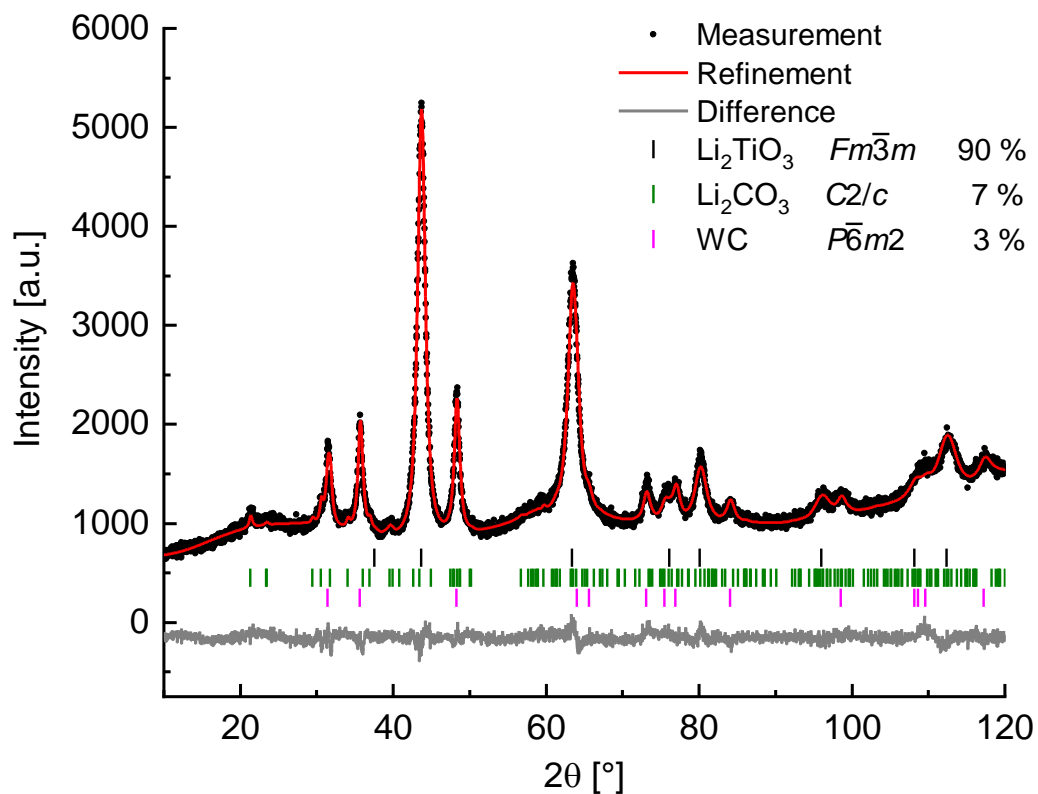


**Figure S5:** Temperature dependent IR signals from coupling of TGA gas flow to IR detector. Colors indicate intensity of the signals.

### Thermal transformation of $\alpha\text{-Li}_2\text{TiO}_3$ to $\beta\text{-Li}_2\text{TiO}_3$



**Figure S6:** Rietveld refinement of the milling product from LiOH and rutile (WC tools, 600 rpm, 6h) after heating to 200 °C for 1 h.  $\text{Li}_2\text{TiO}_3$  in SG  $Fm\bar{3}m$  with  $a = 4.1435(1)$  Å,  $V = 71.14(1)$  Å<sup>3</sup>, number of reflections = 8 and  $R_{\text{Bragg}} = 1.50\%$ . Refinement parameters: number of independent parameters = 48,  $R_{\text{wp}} = 3.08\%$ ,  $R_{\text{exp}} = 2.63\%$ ,  $GOF = 1.17$ .

Transformation of  $\beta$ - $\text{Li}_2\text{TiO}_3$  and spinel  $\text{Li}_4\text{Ti}_5\text{O}_{12}$  to  $\alpha$ - $\text{Li}_2\text{TiO}_3$ 

**Figure S7:** Rietveld refinement of  $\beta$ - $\text{Li}_2\text{TiO}_3$  after ball milling with WC tools for 6 h at 600 rpm.  $\text{Li}_2\text{TiO}_3$  in SG  $Fm\bar{3}m$  with  $a = 4.1463(2) \text{ \AA}$ ,  $V = 71.28(1) \text{ \AA}^3$ , number of reflections = 8 and  $R_{\text{Bragg}} = 0.60\%$ . Refinement parameters: number of independent parameters = 31,  $R_{\text{wp}} = 3.60\%$ ,  $R_{\text{exp}} = 2.85\%$ ,  $GOF = 1.26$ .

$^6\text{Li}$  SPE MAS NMR of  $\text{Li}_4\text{Ti}_5\text{O}_{12}$

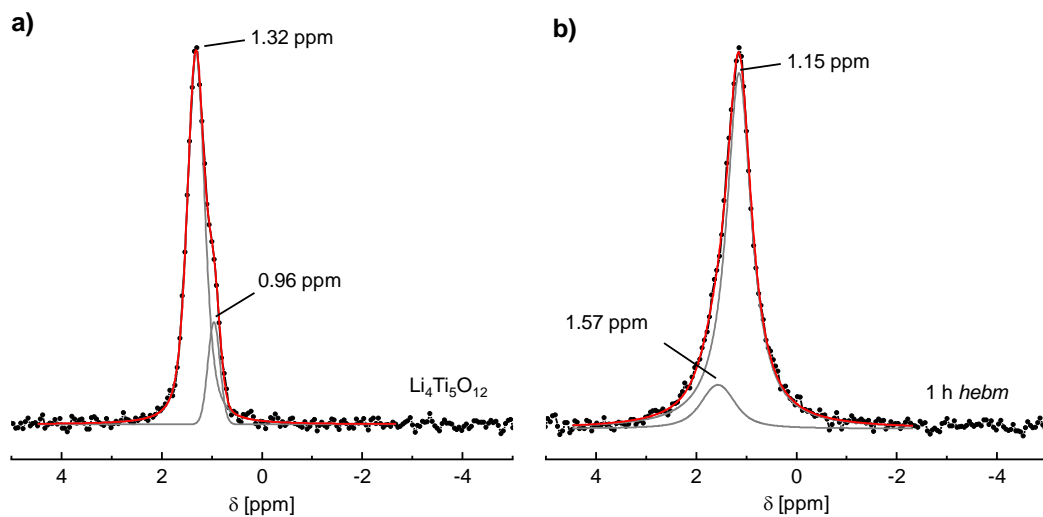


**Figure S8:**  $^6\text{Li}$  SPE MAS NMR spectra of a) spinel  $\text{Li}_4\text{Ti}_5\text{O}_{12}$ , b) after *hebm* for 1 h. The spectra were referenced against solid LiCl and fitted with two independent Voigt functions with  $R^2 > 0.99$ .

## 7 Mechanochemical Synthesis of $\text{Mn}_3\text{O}_4$ Nanocrystals and their Lithium Intercalation Capability

The aim of this study was to establish a synthetic route to form  $\text{Mn}_3\text{O}_4$  nanocrystals without the need of solvents or high temperature treatment. Additionally, the lithium intercalation capability of the formed product is screened by chemical lithium intercalation and compared to a coarse grained product from a solid-state reaction. The phase compositions, crystallite sizes and lattice parameters are extracted from PXRD with Rietveld refinement.

The mechanochemical synthesis of  $\text{Mn}_3\text{O}_4$  is conducted by grinding the simple oxides  $\text{MnO}$  and  $\text{Mn}_2\text{O}_3$  in a stoichiometry of 1:1, which forms  $\text{Mn}_3\text{O}_4$  without oxidation or reduction reactions. A milling map is constructed by systematically varying milling speed and milling time. It is shown that the  $\text{Mn}_3\text{O}_4$  formation is primarily affected by milling speed. Even at low speed and short grinding time, the crystallite size of the educts is massively reduced and  $\text{Mn}_3\text{O}_4$  formation takes place already. A complete conversion can be achieved after milling for 12 h at 600 rpm rotational speed. The pure product reveals a crystallite size below 20 nm. The lattice parameters are identical to the ones of a coarse grained product from a solid-state reaction.

The lithium intercalation capability of the mechanochemically formed  $\text{Mn}_3\text{O}_4$  is screened by a chemical lithium intercalation reaction with  $\text{BuLi}$  in dry hexane at room temperature. To observe the intercalation speed, the reaction is stopped after one hour. A phase portion of 50%  $\text{Li}_x\text{Mn}_3\text{O}_4$  is observed in Rietveld refinement. The refined lattice parameters and cell volume match the published ones very closely, for which reason  $x = 1$  is assumed. Coarse grained  $\text{Mn}_3\text{O}_4$  shows no reaction at the same conditions, indicating that the milling process induces additional structure defects that cannot be directly observed with PXRD.

In conclusion,  $\text{Mn}_3\text{O}_4$  can be formed by simple grinding of a mixture of  $\text{MnO}$  and  $\text{Mn}_2\text{O}_3$ . A nanocrystalline product with very high lithium intercalation capability, compared to a coarse grained product, is obtained.

These results were published in the journal *Inorganic Chemistry* (American Chemical Society, ACS):

D. Becker, M. Klos, G. Kickelbick, Mechanochemical Synthesis of  $Mn_3O_4$  Nanocrystals and their Lithium Intercalation Capability. *Inorg. Chem.* **2019**, 15021-15024.

DOI:10.1021/acs.inorgchem.9b02429.

Dennis Becker carried out the experimental work, data interpretation and evaluation, and preparation of the original draft of the publication. Michael Klos has contributed with experimental work, scientific ideas, and editing of the manuscript. Guido Kickelbick has contributed with scientific ideas, interpretation and discussions of the results, and editing of the manuscript.

The publication is reproduced with permission of the American Chemical Society (ACS).

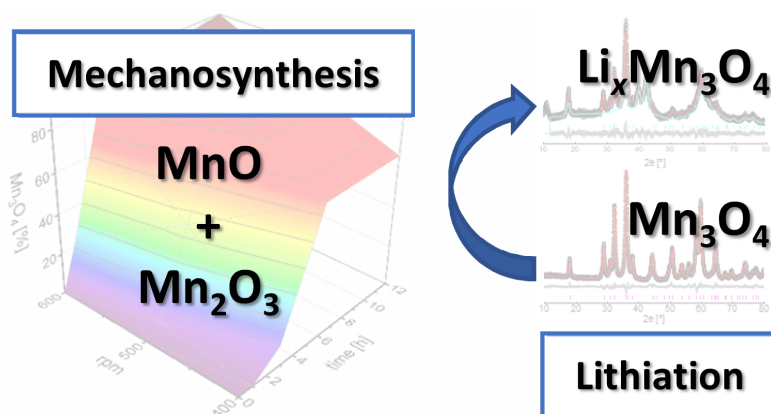


Figure 7.1: Table of contents graphic – Milling map of the mechanochemical  $Mn_3O_4$  synthesis and Rietveld plots of the products from the chemical lithium intercalation. DOI:10.1021/acs.inorgchem.9b02429.

# Mechanochemical Synthesis of Mn<sub>3</sub>O<sub>4</sub> Nanocrystals and Their Lithium Intercalation Capability

Dennis Becker, Michael Klos, and Guido Kickelbick\*

Saarland University, Inorganic Solid-State Chemistry, Campus, Building C4 1, 66123 Saarbrücken, Germany

 Supporting Information

**ABSTRACT:** Syntheses of Mn<sub>3</sub>O<sub>4</sub> involve either high sintering temperatures to produce well crystallized products or the use of water-soluble precursors, surfactants, and organic solvents to generate nanocrystalline products. Mechanochemical approaches are known to be effective in the preparation of fine-grained or nanoscaled materials, while also being environmentally friendly because no solvents and no sintering at high temperatures are required. We report the solvent free mechanochemical synthesis of Mn<sub>3</sub>O<sub>4</sub> nanocrystals at room temperature, from a mixture of MnO and Mn<sub>2</sub>O<sub>3</sub>. The single-phase product was characterized by Rietveld refinement and SEM images. The obtained crystallite size was 14.2(2) nm, which is among the smallest ever produced crystallite sizes of Mn<sub>3</sub>O<sub>4</sub>. The obtained product reveals an enormous increase in lithium intercalation capability, which was proven via chemical lithium intercalation at room temperature. More than 50% lithiation of nanocrystalline Mn<sub>3</sub>O<sub>4</sub> is observed after a reaction time of 1 h, while coarse-grained material from a solid-state reaction shows no intercalation under the same reaction conditions. Therefore, the produced manganese oxide has a high potential in lithium battery applications.

Hausmannite Mn<sub>3</sub>O<sub>4</sub>, especially nanosized or modified with graphene, is known to be an effective anode material for lithium ion batteries.<sup>1,2</sup> However, ex situ investigations via chemical lithiation with *n*-butyllithium have so far only been reported for well crystallized products.<sup>3,4</sup> The lithiation is found to be very slow and takes several days or up to weeks to be completed. In several studies it was shown that lithium intercalation as well as catalytic activity of metal oxides strongly depend on diffusion path lengths, surface area, and morphology of the used material.<sup>5–7</sup> Several synthetic methods to produce Mn<sub>3</sub>O<sub>4</sub> with different morphologies and particle sizes are known, but mechanochemical approaches are rare.

Sintering of manganese carbonate or oxides in air with subsequent quenching or the wet chemical precipitation of manganese(II) salts with simultaneous oxidation by air results in coarse-grained materials.<sup>8–11</sup> The diffusion paths in the resulting materials are long and the surface area is low, limiting the efficient application as intercalation or catalytically active material. Nanocrystalline Mn<sub>3</sub>O<sub>4</sub> may be obtained via solvothermal synthesis from Mn(NO<sub>3</sub>)<sub>2</sub> in oleylamine,<sup>12</sup> precipitation of Mn(NO<sub>3</sub>)<sub>2</sub> with oxidation by H<sub>2</sub>O<sub>2</sub> in ionic liquids,<sup>13</sup> ultrasound-based emulsions synthesis,<sup>14</sup> or refluxing

Mn(acac)<sub>3</sub> in tri(ethylene glycol).<sup>15</sup> However, large quantities of solvents are required in all these approaches, making them less appealing from an ecological point of view. Wet mechanochemical approaches to synthesize Mn<sub>3</sub>O<sub>4</sub> nanoparticles have been proposed by milling of elemental metal powders in water<sup>16</sup> and by ultrasound-assisted milling of manganese acetate in water.<sup>17</sup> Although the use of water as solvent is ecologically beneficial, long drying at elevated temperatures is necessary to use the products subsequently.

Dry mechanochemical approaches are known to be effective to produce fine grained or nanoscaled materials, while also being environmentally friendly because very little or no solvents or surfactants are required in the process.<sup>18</sup> Even though milling of some manganese oxides has been described in literature, no mechanochemical synthesis of nanocrystalline Mn<sub>3</sub>O<sub>4</sub> from simpler oxides has been reported so far. Fishman et al.<sup>19,20</sup> describe the milling of coarse-grained Mn<sub>3</sub>O<sub>4</sub> or mixtures of Mn<sub>3</sub>O<sub>4</sub> with Mn<sub>2</sub>O<sub>3</sub> or MnO<sub>2</sub> and Mn<sub>2</sub>O<sub>3</sub> with MnO<sub>2</sub>. A solid-state synthesis with subsequent quenching is still necessary to produce Mn<sub>3</sub>O<sub>4</sub>.

Here we report the facile and solventless mechanochemical synthesis of Mn<sub>3</sub>O<sub>4</sub> nanocrystals, starting from a dry mixture of MnO and Mn<sub>2</sub>O<sub>3</sub>. The mechanochemically formed Mn<sub>3</sub>O<sub>4</sub> rapidly intercalates lithium in a chemical lithium intercalation reaction with *n*-butyllithium at room temperature, while coarse-grained Mn<sub>3</sub>O<sub>4</sub> from a solid-state synthesis shows no reaction under the same conditions.

High energy ball milling (hebm) of stoichiometric mixtures of MnO and Mn<sub>2</sub>O<sub>3</sub> powders in a planetary ball mill in ZrO<sub>2</sub> grinding jars leads to the formation of new reflections in the powder X-ray patterns, which match Mn<sub>3</sub>O<sub>4</sub> in the Hausmannite structure (Figure 1). Gray bars highlight the formation of the main reflections of Mn<sub>3</sub>O<sub>4</sub>. The change in the patterns is strongly dependent on parameters, such as milling speed and milling time. A formation of Mn<sub>3</sub>O<sub>4</sub> can also be detected by the color change of the resulting powders. Pure MnO is dark green and Mn<sub>2</sub>O<sub>3</sub> is black, while pure Mn<sub>3</sub>O<sub>4</sub> is reddish brown. At shorter milling times the powders are dominated by the black color of Mn<sub>2</sub>O<sub>3</sub>, longer milling times provide powders with a more brownish color tone. The occurrence of a mechanochemical reaction between MnO and Mn<sub>2</sub>O<sub>3</sub> can be explained by the so-called *hot spot model*.<sup>21</sup> It is assumed that local temperatures of several 1000 K arise for 10<sup>-4</sup> to 10<sup>-3</sup> s in the event of a collision, propagating a solid-state reaction.

Received: August 13, 2019

Published: November 5, 2019

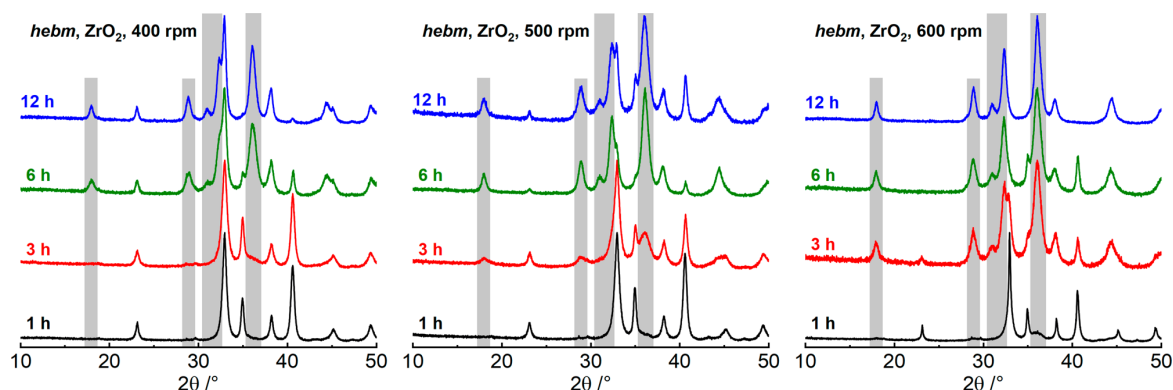


**Figure 1.** XRD patterns of the milling products of  $\text{MnO} + \text{Mn}_2\text{O}_3$  milled at 400, 500, and 600 rpm, for 1, 3, 6, and 12 h. Gray bars indicate the main reflections of  $\text{Mn}_3\text{O}_4$ .

The XRD patterns are predominantly defined by  $\text{MnO}$  and  $\text{Mn}_2\text{O}_3$  after a milling time of 1 h. The formation of  $\text{Mn}_3\text{O}_4$  reflections becomes clearly visible after a milling time of 3 h at 500 and 600 rpm. At 400 rpm, the reflections of  $\text{Mn}_3\text{O}_4$  are observed after 6 h milling time. Rietveld refinement applying TOPAS 4.2<sup>22</sup> yields the phase quantities and mean crystallite size  $\langle L \rangle$  (definition of  $\langle L \rangle$  in Supporting Information) of  $\text{MnO}$ ,  $\text{Mn}_2\text{O}_3$ , and  $\text{Mn}_3\text{O}_4$ . A 3D milling map reveals the influence of the different milling parameters on the refined phase portions of  $\text{Mn}_3\text{O}_4$  (Figure 2).

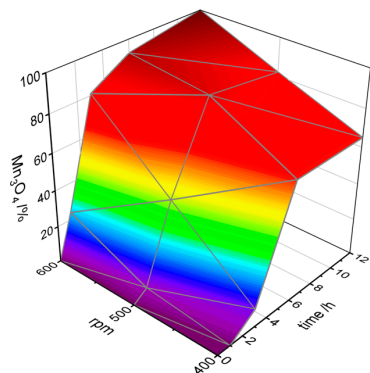


**Figure 2.** 3D Milling map of the formation of  $\text{Mn}_3\text{O}_4$  after milling of  $\text{MnO}$  and  $\text{Mn}_2\text{O}_3$  with different parameters (12 data points from Figure 1, indicated by gray lines). Weight fractions are received from Rietveld refinements.

After milling at 400 and 500 rpm for 1 h, less than 5% of  $\text{Mn}_3\text{O}_4$  can be detected. In contrast, milling at 600 rpm for 1 h leads to formation of 25%  $\text{Mn}_3\text{O}_4$ , which indicates that the milling speed is the dominating effect for the product formation. The crystallite size of  $\text{MnO}$  and  $\text{Mn}_2\text{O}_3$  is reduced to approximately 30 and 20 nm respectively, even after milling for just 1 h at 400 rpm milling speed. Since the size reduction occurs faster than the reaction between the educts, it is assumed that the particle size of the starting materials has no significant influence. The crystallite size of  $\text{MnO}$  and  $\text{Mn}_2\text{O}_3$  stays in this range after longer milling times and at higher milling speeds, while the newly formed  $\text{Mn}_3\text{O}_4$  exhibits a crystallite size of less than 10 nm. Milling for at least 6 h at 400, 500, or 600 rpm produces  $\text{Mn}_3\text{O}_4$  as the main phase, with

phase portions of 65%, 88%, and 93%, respectively. Rietveld refinement yields a crystallite size of 10 to 14 nm. At 400 rpm, the product formation becomes stagnant after milling for 6 h, and increased milling time does not increase the  $\text{Mn}_3\text{O}_4$  content further. A complete conversion of the  $\text{MnO}-\text{Mn}_2\text{O}_3$  mixture to  $\text{Mn}_3\text{O}_4$  is observed after milling at 600 rpm for 12 h. A Rietveld refinement (Supporting Information, Figure S11) yields a crystallite size of 14.2(2) nm. The reflection broadening is almost exclusively caused by crystallite size (the strain contribution is very low). The refined lattice parameters are  $a = 5.7691(2)$  Å and  $c = 9.4558(4)$  Å. These match the lattice parameters of  $a = 5.763$  Å and  $c = 9.456$  Å as reported by Boucher et al.<sup>23</sup> quite closely. Rietveld refinement of the pattern of  $\text{Mn}_3\text{O}_4$  from the solid-state reaction (sintering of  $\text{MnCO}_3$  at 1100 °C in air) yields lattice parameters of  $a = 5.7622(1)$  Å and  $c = 9.4701(1)$  Å. The slightly longer  $c$  lattice parameter may be explained by a somewhat higher Mn(III) content caused by oxygen uptake in the cooling process, thus increasing the effect of the Jahn–Teller distortion. Overall, the mechanochemically formed  $\text{Mn}_3\text{O}_4$  reveals no deviation from the expected Hausmannite structure.

The difference in size and morphology of  $\text{Mn}_3\text{O}_4$  from a classical solid-state and the mechanochemical synthesis is noticeable in the SEM images in Figure 3. The solid-state

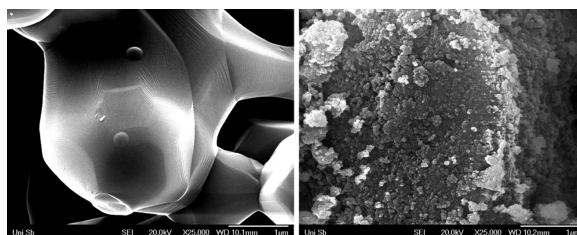


**Figure 3.** SEM images of pure  $\text{Mn}_3\text{O}_4$  from a standard solid-state reaction at 1000 °C (left) and pure  $\text{Mn}_3\text{O}_4$  from the mechanochemical synthesis at 600 rpm and 12 h (right); 25000 times magnification.

reaction leads to formation of micrometer-sized intergrown crystals with smooth edges. The mechanochemical synthesis on the other hand provides a product composed of agglomerated small particles. However, neither the particle size nor its morphology can be determined accurately from the SEM image.

For a compound to qualify as lithium battery anode or cathode material, the ability to intercalate lithium ions is necessary. Moreover, effective intercalation hosts should reveal fast intercalation processes. The lithium intercalation capability may be probed via chemical lithium intercalation with *n*-butyllithium (BuLi).<sup>24</sup> Full lithiation of Mn<sub>3</sub>O<sub>4</sub> to form Li<sub>*x*</sub>Mn<sub>3</sub>O<sub>4</sub> (with *x* ≈ 1) is typically achieved by refluxing in *n*-hexane with BuLi for several days.<sup>3</sup> Since the diffusion paths in mechanochemically synthesized Mn<sub>3</sub>O<sub>4</sub> are short and the surface area is higher, due to the smaller particle size, a much faster lithiation reaction than for coarse-grained material from a solid-state reaction is anticipated. To emphasize this, the reaction was conducted at room temperature and was stopped after a short reaction time of 1 h by adding 2-propanol, to quench remaining butyllithium. The coarse-grained material from the solid-state reaction exhibits no change in the X-ray diffraction pattern and, thus, no intercalation reaction under these conditions. In contrast, nanocrystalline Mn<sub>3</sub>O<sub>4</sub> from the proposed mechanochemical synthesis reveals a rapid intercalation reaction. More than 50% Li<sub>*x*</sub>Mn<sub>3</sub>O<sub>4</sub> is formed after 1 h (Figure 4).

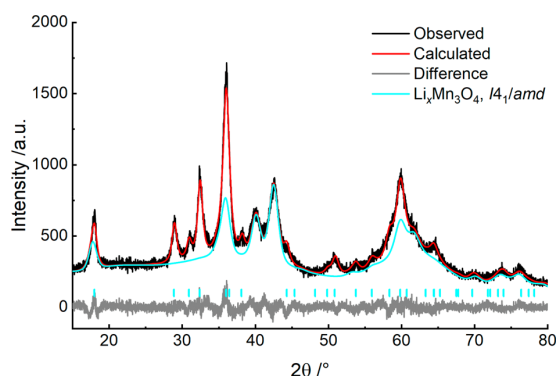


**Figure 4.** Rietveld plot of the Li intercalation product of Mn<sub>3</sub>O<sub>4</sub> from the mechanochemical synthesis (ZrO<sub>2</sub> tools, 600 rpm, 12 h): 56.4% Li<sub>*x*</sub>Mn<sub>3</sub>O<sub>4</sub>, SG *I4<sub>1</sub>/amd*, *a* = 6.019(1) Å, *c* = 9.001(2) Å, *V* = 326.1(2) Å<sup>3</sup>, *R*<sub>Bragg</sub> = 0.90%, phase portion is shown in cyan; 43.6% Mn<sub>3</sub>O<sub>4</sub>, SG *I4<sub>1</sub>/amd*, *a* = 5.787(1) Å, *c* = 9.428(2) Å, *V* = 315.8(2) Å<sup>3</sup>, *R*<sub>Bragg</sub> = 1.29%, phase portion is not shown. Refinement parameters: 30 independent parameters, *R*<sub>wp</sub> = 6.32%, *R*<sub>exp</sub> = 5.06%, GOF = 1.25.

The refinement yields lattice parameters of *a* = 6.019(1) Å and *c* = 9.001(2) Å for Li<sub>*x*</sub>Mn<sub>3</sub>O<sub>4</sub>. Thackeray et al.<sup>3</sup> have reported lattice parameters *a* = 6.022(2) Å and *c* = 9.011(4) Å. While the refined *a* parameter is in accordance with the published data, the refined *c* parameter is shorter. Since lithium intercalation leads to a reduction of Mn(III) to Mn(II), a contraction of the *c* lattice parameter is to be expected, due to the decreasing contribution of Jahn–Teller distortion caused by Mn(III). A shorter *c* parameter may therefore indicate a slightly higher lithium content in the lithiated phase. However, the refined cell volume of 326.1(2) Å<sup>3</sup> is somewhat smaller than the reported volume of 326.8(2) Å<sup>3</sup>, which in turn indicates a slightly lower or equal degree of lithiation. The remaining Mn<sub>3</sub>O<sub>4</sub> reveals lattice parameters of *a* = 5.787(1) Å and *c* = 9.428(2) Å, which differ clearly from the lattice parameters of the educt Mn<sub>3</sub>O<sub>4</sub> from the mechanochemical synthesis (*a* = 5.7691(2) Å, *c* = 9.4558(4) and *V* = 314.72(2) Å<sup>3</sup>). Since the volume of the unit cell increases by about 1 Å<sup>3</sup>,

minor lithiation may be assumed, shifting the lattice parameters in the described direction.

Many syntheses to form coarse-grained or nanocrystalline Mn<sub>3</sub>O<sub>4</sub> are known, though no direct and solventless mechanochemical reaction has been proposed so far. We have presented the formation of Mn<sub>3</sub>O<sub>4</sub> from the simple oxides MnO and Mn<sub>2</sub>O<sub>3</sub> by a mechanochemical approach. The product forms quantitatively, exhibits no discernible deviation from the expected Hausmannite structure, and shows an extremely small crystallite size of 14 nm. SEM images reveal agglomerates of nanometer sized spherical particles. Chemical lithium intercalation with *n*-butyllithium at room temperature reveals a rapid intercalation reaction, while typical coarse-grained material from a solid-state reaction shows, under the same reaction conditions, no intercalation whatsoever.

## ■ ASSOCIATED CONTENT

### Supporting Information

The Supporting Information is available free of charge on the ACS Publications website at DOI: 10.1021/acs.inorgchem.9b02429.

Experimental details, Rietveld refinement, and surface area measurements (PDF)

## ■ AUTHOR INFORMATION

### Corresponding Author

\*Tel: +49 (0)681 302 70651. E-mail: [guido.kickelbick@uni-saarland.de](mailto:guido.kickelbick@uni-saarland.de).

### ORCID

Guido Kickelbick: 0000-0001-6813-9269

### Notes

The authors declare no competing financial interest.

## ■ ACKNOWLEDGMENTS

We thank Dr. Robert Haberkorn for recording of the SEM images and helpful discussion. We also thank Prof. Volker Presser for surface area measurements and fruitful discussions.

## ■ REFERENCES

- (1) Wang, H.; Cui, L.-F.; Yang, Y.; Sanchez Casalongue, H.; Robinson, J. T.; Liang, Y.; Cui, Y.; Dai, H. Mn<sub>3</sub>O<sub>4</sub> – Graphene Hybrid as a High-Capacity Anode Material for Lithium Ion Batteries. *J. Am. Chem. Soc.* **2010**, *132*, 13978–13980.
- (2) Gao, J.; Lowe, M. A.; Abruña, H. D. Spongelike Nanosized Mn<sub>3</sub>O<sub>4</sub> as a High-Capacity Anode Material for Rechargeable Lithium Batteries. *Chem. Mater.* **2011**, *23*, 3223–3227.
- (3) Thackeray, M. M.; David, W. I. F.; Bruce, P. G.; Goodenough, J. B. Lithium Insertion into Manganese Spinels. *Mater. Res. Bull.* **1983**, *18*, 461–472.
- (4) Fernández-Rodríguez, J. M.; Morales, J.; Tirado, J. L. Thermal Evolution of the Lithiation Product of Mn<sub>3</sub>O<sub>4</sub>. *Thermochim. Acta* **1989**, *146*, 365–369.
- (5) Wagemaker, M.; Borghols, W. J. H.; Mulder, F. M. Large Impact of Particle Size on Insertion Reactions. A Case for Anatase Li<sub>*x*</sub>TiO<sub>2</sub>. *J. Am. Chem. Soc.* **2007**, *129*, 4323–4327.
- (6) Yamashita, T.; Vannice, A. NO Decomposition over Mn<sub>2</sub>O<sub>3</sub> and Mn<sub>3</sub>O<sub>4</sub>. *J. Catal.* **1996**, *163*, 158–168.
- (7) Stobbe, E. R.; de Boer, B. A.; Geus, J. W. The Reduction and Oxidation Behaviour of Manganese Oxides. *Catal. Today* **1999**, *47*, 161–167.
- (8) Perthel, R.; Jahn, H. Über Das Paramagnetische Verhalten von Mn<sub>3</sub>O<sub>4</sub> und Co<sub>3</sub>O<sub>4</sub>. *Phys. Status Solidi B* **1964**, *5*, 563–568.

- (9) Buhl, R. Manganites Spinelles Purs d'elements de Transition Preparations et Structures Cristallographiques. *J. Phys. Chem. Solids* **1969**, *30*, 805–812.
- (10) Ardizzzone, S.; Bianchi, C. L.; Tirelli, D.  $Mn_3O_4$  and  $\gamma$ - $MnOOH$  Powders, Preparation, Phase Composition and XPS Characterisation. *Colloids Surf., A* **1998**, *134*, 305–312.
- (11) Al Sagheer, F. A.; Hasan, M. A.; Pasupulety, L.; Zaki, M. I. Low-Temperature Synthesis of Hausmannite  $Mn_3O_4$ . *J. Mater. Sci. Lett.* **1999**, *18*, 209–211.
- (12) Li, P.; Nan, C.; Wei, Z.; Lu, J.; Peng, Q.; Li, Y.  $Mn_3O_4$  Nanocrystals: Facile Synthesis, Controlled Assembly, and Application. *Chem. Mater.* **2010**, *22*, 4232–4236.
- (13) Durmus, Z.; Kavas, H.; Baykal, A.; Toprak, M. S. A Green Chemical Route for the Synthesis of  $Mn_3O_4$  Nanoparticles. *Cent. Eur. J. Chem.* **2009**, *7*, 555–559.
- (14) Bastami, T. R.; Entezari, M. H. Sono-Synthesis of  $Mn_3O_4$  Nanoparticles in Different Media without Additives. *Chem. Eng. J.* **2010**, *164*, 261–266.
- (15) Gao, M.-R.; Xu, Y.-F.; Jiang, J.; Zheng, Y.-R.; Yu, S.-H. Water Oxidation Electrocatalyzed by an Efficient  $Mn_3O_4/CoSe_2$  Nanocomposite. *J. Am. Chem. Soc.* **2012**, *134*, 2930–2933.
- (16) Chen, D.; Ni, S.; Chen, G. L.; Chen, Z. H. Preparation of Nano-Particles of Metal Oxides via a Novel Solid-Liquid Mechanochemical Reaction Technology. *Adv. Mater. Res.* **2007**, *26–28*, 671–674.
- (17) Chen, D.; Yang, B.; Jiang, Y.; Zhang, Y. Z. Synthesis of  $Mn_3O_4$  Nanoparticles for Catalytic Application via Ultrasound-Assisted Ball Milling. *ChemistrySelect* **2018**, *3*, 3904–3908.
- (18) James, S. L.; Adams, C. J.; Bolm, C.; Braga, D.; Collier, P.; Frisci, T.; Grepioni, F.; Harris, K. D. M.; Hyett, G.; Jones, W.; et al. Mechanochemistry: Opportunities for New and Cleaner Synthesis. *Chem. Soc. Rev.* **2012**, *41*, 413–447.
- (19) Fishman, A. Y.; Ivanov, M. A.; Petrova, S. A.; Zakharov, R. G. Structural Phase Transitions in Mechanoactivated Manganese Oxides. *Defect Diffus. Forum* **2010**, *297–301*, 1306–1311.
- (20) Fishman, A. Y.; Kurennykh, T. E.; Mitrofanov, V. Y.; Pastukhov, E. A.; Petrova, S. A.; Uporov, S. A.; Vykhodets, V. B.; Zakharov, R. G. Mechanical Activation of Mn-O Oxides: Structural Phase Transitions, Magnetism and Oxygen Isotope Exchange. *Diffus. Found.* **2014**, *1*, 175–197.
- (21) Baláz, P.; Achimovicová, M.; Baláz, M.; Billik, P.; Cherkezova-Zheleva, Z.; Criado, J. M.; Delogu, F.; Dutková, E.; Gaffet, E.; Gotor, F. J.; Kumar, R.; Mitov, I.; Rojac, T.; Senna, M.; Streletskii, A.; Wiczorek-Ciurowa, K. Hallmarks of mechanochemistry: from nanoparticles to technology. *Chem. Soc. Rev.* **2013**, *42*, 7571–7637.
- (22) *Topas 4.2. General Profile and Structure Analysis Software for Powder Diffraction Data*. Bruker AXS, Karlsruhe, Ger. 2009.
- (23) Boucher, B.; Buhl, R.; Perrin, M. Proprietes et Structure Magnetique de  $Mn_3O_4$ . *J. Phys. Chem. Solids* **1971**, *32*, 2429–2437.
- (24) Whittingham, M. S. N-Butyllithium – An Effective, General Cathode Screening Agent. *J. Electrochem. Soc.* **1977**, *124*, 1387.

---

# Supporting Information

## Mechanochemical Synthesis of Mn<sub>3</sub>O<sub>4</sub> Nanocrystals and their Lithium Intercalation Capability

Dennis Becker<sup>1</sup>, Michael Klos<sup>1</sup> and Guido Kickelbick<sup>1,\*</sup>

<sup>1</sup>Saarland University, Inorganic Solid-state Chemistry, Campus, Building C4 1, 66123 Saarbrücken, Germany

\*Correspondence: guido.kickelbick@uni-saarland.de

### 1. Materials

MnO (Alfa Aesar GmbH, Karlsruhe, Germany, 99%), MnCO<sub>3</sub> (Alfa Aesar GmbH, Karlsruhe, Germany, 99.9%), Mn<sub>2</sub>O<sub>3</sub> (ChemPur, Karlsruhe, Germany, 99.9%), *n*-butyllithium 1.6 M in *n*-hexane (Acros Organics, Geel, Belgium) and 2-propanole (Biesterfeld Spezialchemie, 97%) were used as received. All solids have been characterized via X-ray diffraction. *n*-hexane (Fisher Scientific GmbH, Geel, Belgium, > 96%) was dried in a solvent purifying system SPS 5 (MBRAUN, Garching, Germany).

### 2. Sample Preparation

All samples were milled in a planetary ball mill, type PM100 (Retsch, Germany). Grinding jars (volume of 50 mL) consisting of yttrium stabilized zirconia (ZrO<sub>2</sub>) and 200 milling balls with a diameter of 5 mm of the same material were used. The rotational speed of the mill was set to 400, 500 or 600 rpm. Approximately 3 g of a mixture of MnO and Mn<sub>2</sub>O<sub>3</sub>, corresponding to a stoichiometry of Mn<sub>3</sub>O<sub>4</sub>, was used in all milling experiments. The ball to powder weight ratio was 27:1. To prevent cementing of the dry powders, 200 µL of 2-propanole were added as process control agent.

Coarse-grained Hausmannite Mn<sub>3</sub>O<sub>4</sub> was synthesized via standard solid-state reaction, by heating MnCO<sub>3</sub> to 1000 °C for 8 h in a platinum crucible.<sup>1</sup> Formation of Mn<sub>2</sub>O<sub>3</sub> was prevented via rapid cooling by removing the crucible from the hot furnace. Syntheses of Mn<sub>3</sub>O<sub>4</sub> from MnO or Mn<sub>2</sub>O<sub>3</sub> always contained Mn<sub>2</sub>O<sub>3</sub> as side product.

Chemical lithium intercalation was conducted by stirring 0.5 – 1.0 g Mn<sub>3</sub>O<sub>4</sub> from mechanochemical and solid-state synthesis in 40 mL of absolute *n*-hexane under Argon atmosphere with 1.05 eq of butyllithium (1.6 M in *n*-hexane) at room temperature. The reaction was stopped after 1 h by adding of 0.1 mL 2-propanole, to quench remaining butyllithium. The product was separated by filtration under Argon and subsequently transferred into an Argon filled glove box.

### 3. Characterization

Powder X-ray diffraction patterns were recorded on a Bruker D8-A25-Advance diffractometer (Bruker, Karlsruhe, Germany) with Cu radiation (40 kV, 40 mA,  $\lambda = 154.0596$  pm). A 12 µm Ni foil working as K $\beta$  filter and a variable divergence slit were mounted at the primary beam side. A LYNXEYE 1D detector was used at the secondary beam side. Fluorescence induced background was reduced by detector discrimination. Data acquisition was carried out in a  $2\theta$  range from 7 to 120° with a step size of 0.013° and a total scan time of 2h. Air sensitive samples from lithium intercalation were measured in an airtight dome sample holder with integrated knife edge in a  $2\theta$  range from 7 to 80°. TOPAS 4.2 was used for the Rietveld refinements.<sup>2</sup> Crystallographic structure and microstructure were refined, while instrumental line broadening was included in a fundamental parameters approach.<sup>3</sup> The mean crystallite size  $\langle L \rangle$  was calculated at the mean

volume weighted column height derived from the integral breadth. The background was fitted by a Chebyshev polynomial function of 15th degree. Structure data were obtained from the crystallography open database (COD)<sup>4</sup> and inorganic crystal structure database (ICSD) (Figure S11).

Gas sorption measurements were conducted by using nitrogen gas at  $-196^\circ\text{C}$  with a Quantachrome iQ system. The specific surface area was determined in the linear pressure range at low partial pressures (Figure S12).<sup>5</sup>

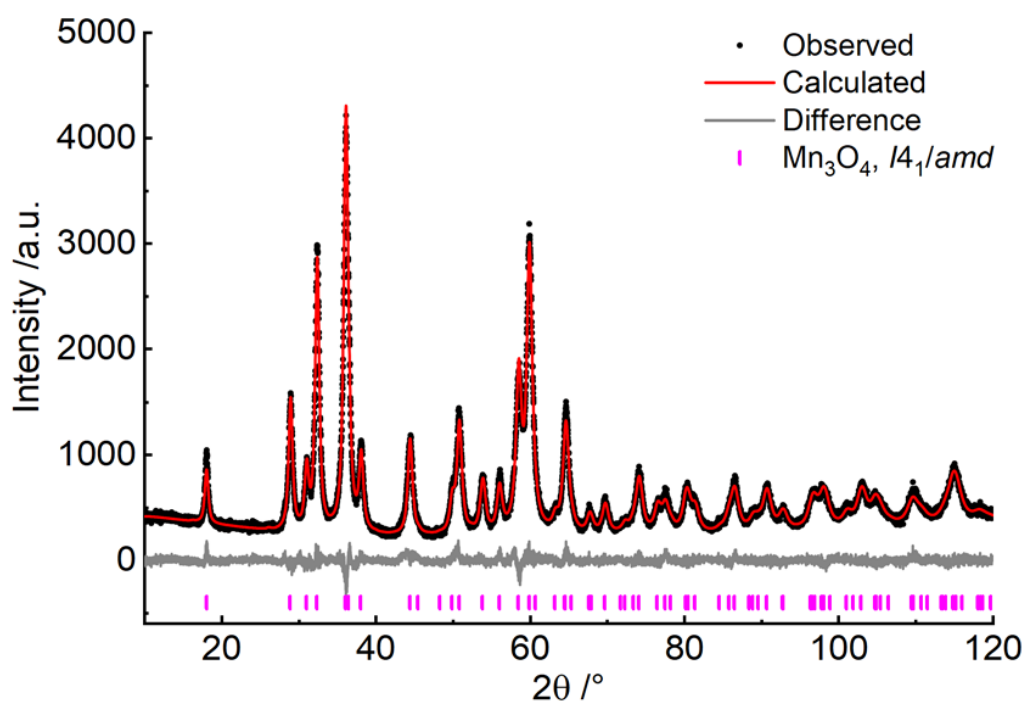


**Figure S11:** Rietveld plot of the milling product from  $MnO$  and  $Mn_2O_3$  ( $ZrO_2$  tools, 600 rpm, 12h).  $Mn_3O_4$ , SG  $I4_1/amd$ ,  $a = 5.7691(2)\text{ \AA}$ ,  $c = 9.4558(4)$ ,  $V = 314.72(2)\text{ \AA}^3$ ,  $R_{Bragg} = 1.36\%$ . Refinement parameters: 27 independent parameters,  $R_{wp} = 5.34\%$ ,  $R_{exp} = 4.24\%$ ,  $GOF = 1.26$ .

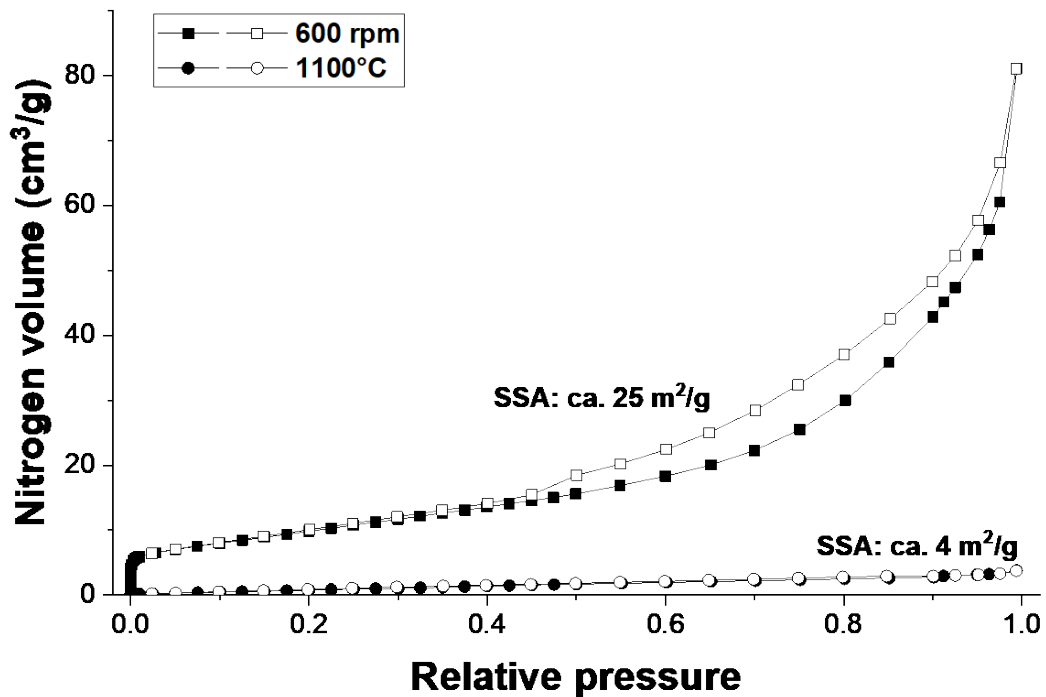


**Figure S12:** Nitrogen sorption measurement of the milling product from MnO and Mn<sub>2</sub>O<sub>3</sub> (ZrO<sub>2</sub> tools, 600 rpm, 12h) compared to the high temperature synthesized product.

#### References

1. Perthel, R.; Jahn, H. Über das paramagnetische Verhalten von Mn<sub>3</sub>O<sub>4</sub> und Co<sub>3</sub>O<sub>4</sub>. *Phys. status solidi* **1964**, *5*, 563–568.
2. Topas 4.2. General Profile and Structure Analysis Software for Powder Diffraction Data. *Bruker AXS, Karlsruhe, Ger.* **2009**.
3. Cheary, R. W.; Coelho, A. A.; Cline, J. P. Fundamental Parameters Line Profile Fitting in Laboratory Diffractometers. *J. Res. Natl. Inst. Stand. Technol.* **2004**, *109*, 1–25.
4. Gražulis, S.; Chateigner, D.; Downs, R. T.; Yokochi, A. F. T.; Quirós, M.; Lutterotti, L.; Manakova, E.; Butkus, J.; Moeck, P.; Le Bail, Crystallography Open Database – an open-access collection of crystal structures. *A. J. Appl. Crystallogr.* **2009**, *42*, 726–729.
5. Thommes, M.; Kaneko, K.; Neimark, A. V.; Olivier, J. P.; Rodriguez-Reinoso, F.; Rouquerol, J.; Sing, K. S. W. Physisorption of gases, with special reference to the evaluation of surface area and pore size distribution (IUPAC Technical Report). *Pure Appl. Chem.* **2015**, *87*, 1051–1069.



## 8 Reactive Milling Induced Structure Changes in Phenylphosphonic acid Functionalized $\text{LiMn}_2\text{O}_4$ Nanocrystals – Synthesis, Rietveld refinement and Thermal Stability

The aim of this study was to interpret the anisotropic line broadening commonly found in  $\text{LiMn}_2\text{O}_4$  after milling. The effects of milling parameters were investigated systematically by varying the milling speed and time. Since pure  $\text{LiMn}_2\text{O}_4$  decomposes under harsher milling conditions, an in situ surface functionalization with phenylphosphonic acid was conducted. This prevented the formation of  $\text{Mn}_2\text{O}_3$ . The surface functionalization is characterized by FT-IR spectroscopy via the characteristic signals of the phosphonic acid OH-groups. A complete functionalization at low rotational speeds is only observed after long milling times. Higher milling speeds allow a complete functionalization after just a few hours of grinding.

PXRD measurements reveal that at lower milling speeds the reflection pattern of spinel  $\text{LiMn}_2\text{O}_4$  is preserved. However, a severe anisotropic broadening is found. Dynamic scanning calorimetry measurements reveal a phase transformation of unmilled  $\text{LiMn}_2\text{O}_4$ , while this transformation is absent in milled  $\text{LiMn}_2\text{O}_4$ . The cubic spinel structure of  $\text{LiMn}_2\text{O}_4$  changes to an orthorhombic structure, which is still closely related to the cubic parent structure. The anisotropic line broadening obtained by milling is therefore attributed to a distribution of lattice parameters resembling the orthorhombic structure, hence the absence of a phase transformation in DSC. A simple and versatile Rietveld refinement model based on the ideal cubic spinel structure is proposed to describe the line shape. A pseudo cubic cell with three independent lattice parameters and the same atomic positions as in the spinel structure are defined. To model a distribution of lattice parameters, three constrained fractions of the pseudo cubic cell are defined. The systematic variation of the milling parameters reveals three different product states. Besides the anisotropic line broadening obtained by milling at low rotational speeds, a cation disorder is introduced at medium milling speeds and a phase transformation to a tetragonal phase is observed after high milling speeds. Since three fractions of a pseudo cubic cell with three independent lattice parameters are used, these three states can be modeled simultaneously. Additionally, crystallite size and phase portions can be extracted. The thermal stability of

the three states is investigated via in situ high temperature XRD measurements for three representative samples. In all cases the cubic spinel structure is obtained. The transformation temperature however changes, depending on the preliminary milling conditions. Additionally, tetragonal  $\text{LiMn}_2\text{O}_4$  with the hausmannite  $\text{Mn}_3\text{O}_4$  structure is also present in every sample after heating to higher temperatures.

In conclusion, depending on the milling parameters three different structure states are obtainable by grinding  $\text{LiMn}_2\text{O}_4$  in a high energy planetary ball mill. A simple and versatile Rietveld refinement model based on three constrained fractions of a pseudo cubic cell is constructed, which is able to simultaneously refine all these structure states.

These results were published in the journal *European Journal of Inorganic Chemistry* (Wiley-VCH Verlag GmbH & Co. KGaA):

D. Becker, R. Haberkorn, G. Kickelbick, Reactive Milling Induced Structure Changes in Phenylphosphonic acid Functionalized  $\text{LiMn}_2\text{O}_4$  Nanocrystals – Synthesis, Rietveld refinement and Thermal Stability. *Eur. J. Inorg. Chem.* **2019**, 4835-4845. DOI:10.1002/ejic.201900946.

Dennis Becker carried out the experimental work, data interpretation and evaluation, and preparation of the original draft of the publication. Robert Haberkorn has contributed with scientific ideas, interpretation and discussions of the results, and editing of the manuscript. Guido Kickelbick has contributed with scientific ideas, interpretation and discussions of the results, and editing of the manuscript.

The publication is reproduced under the terms of the Creative Commons Attribution-NonCommercial License, which permits use, distribution and reproduction in any medium, provided the original work is properly cited and is not used for commercial purposes.

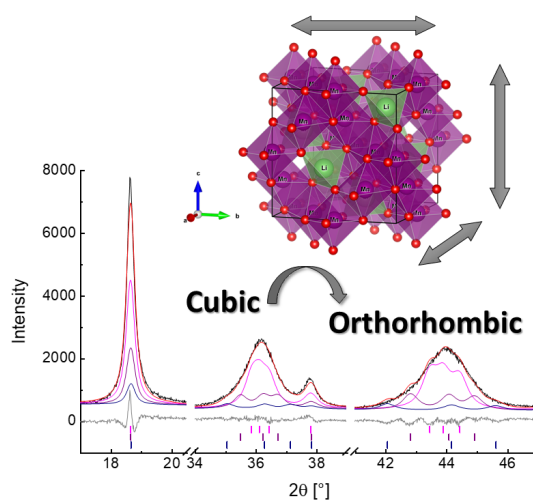


Figure 8.1: Table of contents graphic – Illustration of the symmetry reduction of cubic  $\text{LiMn}_2\text{O}_4$  and the corresponding Rietveld plot with multiple phases. DOI:10.1002/ejic.201900946.

## Mechanochemistry

Reactive Milling Induced Structure Changes in Phenylphosphonic Acid Functionalized  $\text{LiMn}_2\text{O}_4$  Nanocrystals – Synthesis, Rietveld Refinement, and Thermal StabilityDennis Becker,<sup>[a]</sup> Robert Haberkorn,<sup>[a]</sup> and Guido Kickelbick\*<sup>[a]</sup>

**Abstract:** Spinel  $\text{LiMn}_2\text{O}_4$  formed in a solid-state reaction was treated with a high energy planetary ball mill. A mechanochemical in situ surface functionalization of the nanocrystallites with a size smaller than 10 nm was achieved by addition of phenylphosphonic acid. The functionalization was proven by infrared spectroscopy and it can be shown that it prevents the formation of  $\text{Mn}_2\text{O}_3$  during the milling process. Structural changes of the samples were investigated via XRD and Rietveld refinement. Mild milling conditions induce an anisotropic broadening of the reflections caused by a distribution of lattice parameters. In this

first stage, we propose a structure model based on orthorhombic  $\text{LiMn}_2\text{O}_4$ . DSC and in situ XRD measurements also verify the presence of the orthorhombic low temperature phase. Medium milling conditions induce a change of intensities, correlated to a cation disorder. Harsher milling conditions induce the transformation to a tetragonal phase. The thermal stability of the formed phases was investigated via in situ high temperature XRD. The reformation of cubic spinel is observed in all samples; however, the transition point depends on the previous milling parameters.

## 1. Introduction

Lithium manganese oxides, especially  $\text{LiMn}_2\text{O}_4$ , are well known for their ability to intercalate or deintercalate lithium ions.<sup>[1]</sup> Based on the reversible lithium intercalation, electrical conductivity, and low cost of manganese,  $\text{LiMn}_2\text{O}_4$  with spinel structure has become a popular cathode material in lithium ion batteries.<sup>[2]</sup> The typical synthesis of spinel  $\text{LiMn}_2\text{O}_4$  is achieved by a solid-state reaction in air at temperatures above 750 °C, from various oxides or carbonates.<sup>[3,4]</sup> Coarse-grained materials are obtained in this way. To enhance the electrochemical performance many efforts were carried out to produce nanocrystalline materials to increase the active surface area and decrease the diffusion path lengths.<sup>[5]</sup> Fine grained or nanocrystalline material can be obtained by lowering the annealing temperature to prevent excessive crystal growth. This may be achieved by dissolving the appropriate metal acetates and complexation agents like citric acid or tartaric acid in ethanol to form a homogeneous precursor powder after drying of the solution.<sup>[6,7]</sup> Alternatively, metal nitrates and polyvinyl alcohol or ethylene glycol are dissolved in distilled water to obtain a homogeneous precursor powder after drying.<sup>[8,9]</sup> The disadvantage of these

preparation methods is the requirement to use large amounts of solvents and complexation agents, making them less attractive in terms of an environmentally friendly production process.

Mechanochemical approaches are well suited to generate products with small crystallite size and high defect concentration, while being environmentally friendly because the use of solvents and high sintering temperatures can often be avoided.<sup>[10]</sup> However, only a few mechanochemical processes to form  $\text{LiMn}_2\text{O}_4$  without thermal annealing have been reported so far. A heat treatment usually cures the structure changes that were introduced during the milling process, therefore longtime stability of the prepared phases, for example under the conditions in a lithium ion battery are limited. In the known mechanochemical syntheses the effects of the milling process on crystal structure and microstructure have seldom been considered. A Rietveld refinement model to accommodate the X-ray diffraction peak shapes of mechanochemically processed  $\text{LiMn}_2\text{O}_4$  has not been proposed yet. In the past, Kosova et al. have obtained  $\text{LiMn}_2\text{O}_4$  by grinding a mixture of  $\text{Li}_2\text{CO}_3$  and  $\text{MnO}_2$  in an AGO-2 planetary ball mill.<sup>[11]</sup> Patterns with broad reflections were obtained, but no interpretation in terms of crystallite size or strain was reported in this study and the ideal cubic structure was assumed. Choi et al. have obtained  $\text{LiMn}_2\text{O}_4$  by treating  $\text{Li}_2\text{O}$  and  $\text{MnO}_2$  in a Spex 8000 shaker mill.<sup>[12]</sup> No lattice parameters were reported, but crystallite size and strain have been evaluated via a Williamson hall plot by single line fitting. A strong contribution to the reflection broadening by strain was proposed, suggesting a high degree of disorder in the structure. Crystallographic structure changes were not considered in this investigation. Disordered cation sites have also been indicated by  $^7\text{Li}$  solid-state NMR of  $\text{LiMn}_2\text{O}_4$  from a mechanochemical

[a] Saarland University,  
Inorganic Solid-State Chemistry,  
Campus C4 1, 4. OG, 66123 Saarbrücken, Germany  
E-mail: guido.kickelbick@uni-saarland.de

Supporting information and ORCID(s) from the author(s) for this article are available on the WWW under <https://doi.org/10.1002/ejic.201900946>.

© 2019 The Authors. Published by Wiley-VCH Verlag GmbH & Co. KGaA. This is an open access article under the terms of the Creative Commons Attribution-NonCommercial License, which permits use, distribution and reproduction in any medium, provided the original work is properly cited and is not used for commercial purposes.

synthesis from  $\text{LiOH}$  or  $\text{Li}_2\text{CO}_3$  with  $\text{MnO}_2$ .<sup>[13]</sup> A severe broadening of reflections occurs similarly by milling  $\text{LiMn}_2\text{O}_4$  from a solid-state reaction.<sup>[14]</sup> The ideal cubic spinel structure was assumed, and the reflections were fitted independently to estimate the ratio of crystallite size and strain broadening. In a different work, a Rietveld refinement based on the cubic spinel structure was conducted.<sup>[15]</sup> Considerable misfits are present due to an anisotropic broadening of the reflections, which is hardly recognizable by single peak fitting. Strain and crystallite size of milled  $\text{LiMn}_2\text{O}_4$  cannot be evaluated satisfactorily in a Rietveld refinement based on the ideal cubic spinel structure.

The idealized structure of stoichiometric  $\text{LiMn}_2\text{O}_4$  is the cubic spinel structure with space group  $Fd\bar{3}m$ . The structure is formed by a cubic close packing of oxygen atoms on the  $32e$  site. Li cations occupy 1/8 of the tetrahedral voids on the  $8a$  site. Mn(III) and Mn(IV) cations occupy 1/2 of the octahedral voids on the  $16d$  site.<sup>[3]</sup> The Jahn–Teller distortion of Mn(III) is compensated by the statistical distribution of Mn(III) and Mn(IV) cations. A structure representation is given in Figure 1.

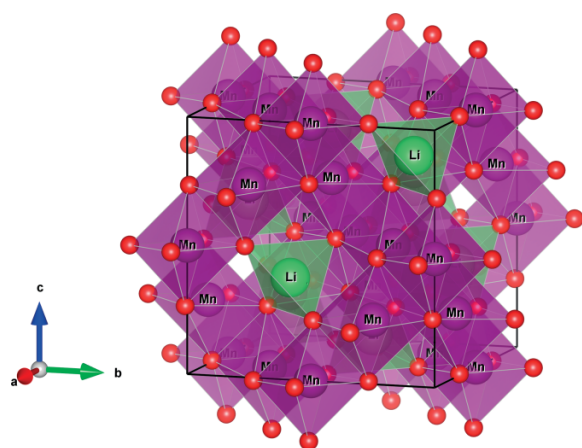


Figure 1. Idealized crystal structure of spinel  $\text{LiMn}_2\text{O}_4$ . Image generated with VESTA.<sup>[16]</sup>

Cubic spinel  $\text{LiMn}_2\text{O}_4$  is the typical phase used in battery applications.<sup>[1,2,5]</sup> However, beside the cubic spinel, orthorhombic, and tetragonal structures are also known. Below  $10^\circ\text{C}$ , a splitting of the spinel reflections is observed, indicating a lowering of the symmetry. A phase transition to an orthorhombic low temperature phase, with a cell volume nearly identical to the cubic structure, is encountered.<sup>[17]</sup> Neutron powder diffraction data have been refined with an orthorhombic structure based on a  $3 \times 3 \times 1$  super cell of cubic spinel, to describe the cation distribution more accurately.<sup>[18]</sup> The models of ideal cubic spinel at room temperature and the orthorhombic structure below  $10^\circ\text{C}$  have also been confirmed by single-crystal X-ray diffraction.<sup>[19]</sup> A combined approach of Rietveld refinement and pair distribution function refinement for neutron diffraction data of  $\text{LiMn}_2\text{O}_4$  reveals that the orthorhombic structure is already present at room temperature in the form of a short-range ordering.<sup>[20]</sup> Cooling of the sample induces the expected transformation to an orthorhombic state with a long-range ordering. The orthorhombic structure has also been stabilized applying

pressures of 2 to 3 GPa at room temperature and up to 415 K.<sup>[21]</sup> The tetragonal structure of  $\text{LiMn}_2\text{O}_4$  is either obtained by lithium intercalation (forming  $\text{Li}_{1+x}\text{Mn}_2\text{O}_4$ ) or by oxygen deficiencies or a surplus of manganese.<sup>[22,23]</sup> In both cases, the concentration of Mn(III) is high enough for the Jahn–Teller effect of Mn(III) to induce a  $c/a$  splitting and subsequently a tetragonal symmetry.

No structure models have been proposed so far to properly describe the changes in the patterns of milled  $\text{LiMn}_2\text{O}_4$  in a Rietveld refinement. The goal of our study is to evaluate the milling induced crystallographic structure changes and microstructure changes in  $\text{LiMn}_2\text{O}_4$ . To prevent a decomposition of  $\text{LiMn}_2\text{O}_4$  in the milling process, phenylphosphonic acid is added as surface functionalization agent. By considering an orthorhombic symmetry and cation disorder, the peak shapes that are dominated by strain can be fitted with a multi-fraction model.<sup>[24,25]</sup> A broad distribution of different states, even with changes in the symmetry between orthorhombic, tetragonal and cubic, can be described in this way. Three different states in the samples are defined and the thermal stability of these states is evaluated via in situ high temperature PXRD measurements.

## 2. Results and Discussion

Milling of coarse-grained  $\text{LiMn}_2\text{O}_4$  prepared in a high temperature solid-state reaction (ssr-LMO) should lead to a reduction of the crystallite size. However, a decomposition of the spinel phase can be observed at harsher milling conditions (Figure 2). New reflections, matching the pattern of  $\text{Mn}_2\text{O}_3$  are formed. This is accompanied by an uneven and wave-like background indicating the formation of amorphous and unknown poorly crystalline phases. The decomposition is observed at a high milling speed (600 rpm) or prolonged milling times of more than 6 h at medium milling speed (400 rpm).

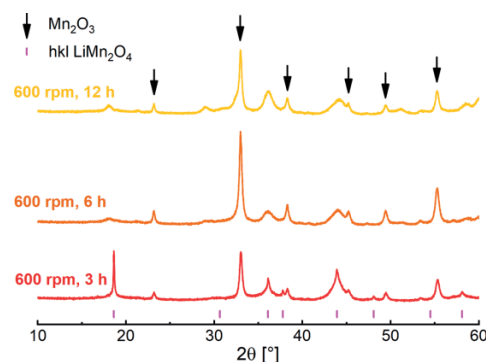


Figure 2. Powder X-ray diffraction patterns of  $\text{LiMn}_2\text{O}_4$  milled for 3, 6 and 12 h at 600 rpm. Arrows indicate reflections of  $\text{Mn}_2\text{O}_3$ . The lines indicate the hkl's of spinel  $\text{LiMn}_2\text{O}_4$ .

We investigated whether the decomposition can be avoided if a surface capping agent is added, such as phenylphosphonic acid (PPA). In previous studies we were able to show that in situ surface-functionalization during milling has beneficial effects on the phase stabilization.<sup>[26–28]</sup> The addition of PPA in the mill-

ing process retains the original reflection pattern even at higher milling speeds and longer milling times, without the formation of clearly visible amounts of  $\text{Mn}_2\text{O}_3$  or an amorphous phase. Therefore, only the results obtained by milling *ssr*-LMO with PPA (consecutively referred to as ball milled LMO or *bm*-LMO) are discussed in the following sections. Since PPA forms covalent bonds with the surface of  $\text{LiMn}_2\text{O}_4$  in the milling process it is assumed that PPA acts as not only a dispersing agent, but also that the in-situ surface functionalization itself plays an integral role in retaining the spinel structure. The formation of a covalent bonds between a phosphonic acid and a metal oxide can be detected by infrared (IR) spectroscopy and has already been established in literature.<sup>[26–28]</sup> To form a stabilizing surface functionalization, the amount of PPA should be as high as possible. A homogeneous powder was formed up to 10 wt.-% of PPA. Higher amounts lead to cementing of the powder in the grinding jar. The IR spectra of the milling products of  $\text{LiMn}_2\text{O}_4$  with 10 wt.-% PPA at 400 rpm are shown in Figure 3. The IR spectra of 200 and 600 rpm milled  $\text{LiMn}_2\text{O}_4$ -PPA mixture are presented in the supporting information (Figure SI 1 and Figure SI 2) and exhibit comparable features.

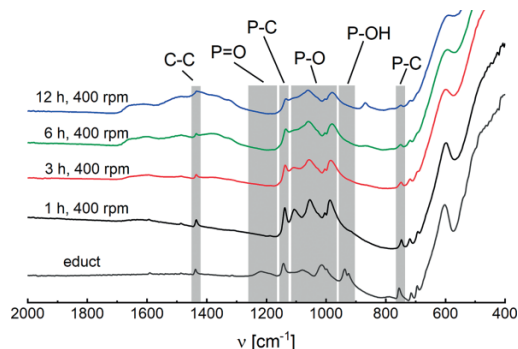


Figure 3. FT-IR spectra of  $\text{LiMn}_2\text{O}_4$  with PPA before (educt) and after milling at 400 rpm for different milling times.

The assignment of the IR bands was carried out according to the published data of Guerrero et al. and Botelho do Rego et al.<sup>[29,30]</sup> The characteristic bands of the phosphorus oxygen vibrations are found in the range between 900 and 1200  $\text{cm}^{-1}$  and reveal whether the phosphonic acid is covalently attached to the surface or not. Generally, surface functionalization of metal oxides takes place due to the condensation reaction of P-OH and P=O groups of the phosphonic acid group with free M=O and M-OH groups on the metal oxide surface.<sup>[29]</sup> After 1 h milling time at 400 rpm a small peak of the P-OH vibration located in the range of 740 to 760  $\text{cm}^{-1}$  can still be detected, indicating no full condensation of the phosphonates with the surface. After 3 h the signal has completely vanished. Additionally, the distinct signal of the P=O double bond, visible at 1160 to 1260  $\text{cm}^{-1}$  in the unmilled starting material mixture, disappears completely after 1 h of milling. Since no further changes between 900 and 1200  $\text{cm}^{-1}$  occur applying longer milling times, the surface functionalization is completed after approximately 3 h at a milling speed of 400 rpm. At 200 rpm the functionalization is completed only after 12 h milling time. At

600 rpm the functionalization is already completed after 1 h milling time. The surface functionalization is therefore dependent on both, milling time and milling speed. In contrast to the P-O vibrations, the C-C and P-C vibrations are less affected. Prolonged milling leads to a slight decrease in intensity of the C-C and P-C vibrations, indicating a partial decomposition of the phenyl groups. The emerging broad signal between 1300 and 1700  $\text{cm}^{-1}$  matches the typical signal observed for metal carbonates.<sup>[31]</sup> Since no crystalline carbonate species like  $\text{Li}_2\text{CO}_3$  or  $\text{MnCO}_3$  were visible in the PXRD patterns, it is assumed that only small amounts of a carbonate species are formed on the surface of the product. Since the appearance of the carbonate signal coincides with the decrease of the phenyl group signals, it is possible that the carbonate formation is the product of the phenyl group decomposition. The uptake of carbon dioxide from surrounding air cannot be excluded, however.

Scanning electron microscopy (SEM) images of *ssr*-LMO milled with PPA at 200, 400 and 600 rpm for 12 h reveal the formation of small particles (Figure 4). The particle size of *ssr*-LMO is in the range of several microns. The milled products on the other hand reveal particles much smaller than 1  $\mu\text{m}$ , which form larger agglomerates. The surface area of the milled products may still be assumed to be much larger than the surface area of *ssr*-LMO.

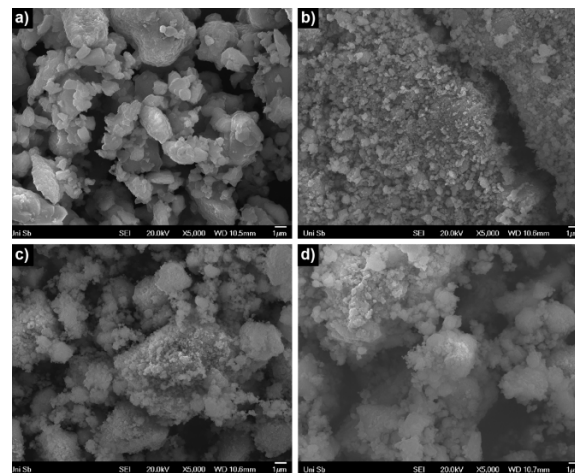


Figure 4. SEM images of  $\text{LiMn}_2\text{O}_4$  after (a) solid-state reaction, (b) milling with PPA at 200 rpm for 12 h, (c) milling with PPA at 400 rpm for 12 h, and (d) milling with PPA at 600 rpm for 12 h. Factor of magnification: 5000.

After milling *ssr*-LMO with PPA in a high energy ball mill, three product states were differentiated via PXRD (Figure 5). Milling at a low milling speed of 200 rpm for up to 6 h produces a coarse-grained fraction with sharp reflections on top of broad reflections corresponding to a fine-grained fraction. The low milling speed may lead to inhomogeneities in the milling process. It is assumed that there are not enough ball impact events in the given milling time to affect every powder particle. A longer milling time of 12 h compensates this and leads to a product, which does not reveal sharp reflections anymore. This marks the first state of the milling products, referred to as **state A**. A very dominant strain effect leads to an anisotropic reflec-

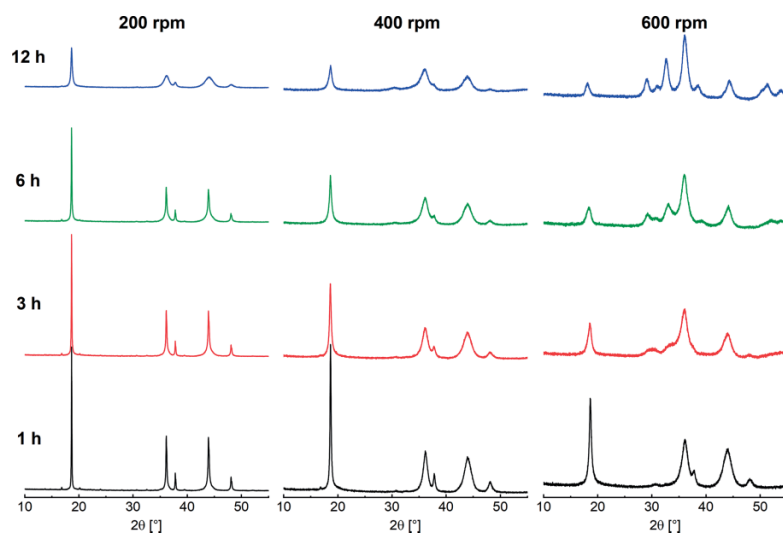


Figure 5. Overview of the powder patterns of  $\text{LiMn}_2\text{O}_4$  with PPA after milling at 200, 400 and 600 rpm for 1, 3, 6, and 12 h, respectively.

tion broadening, like it has already been mentioned by Kang et al. and Kamarulzaman et al.<sup>[14,15]</sup> This state extends to the products obtained from a milling speed of 400 rpm up to a milling time of 3 h. Further milling initiates the second observed state, in which the reflection intensities start to change, indicating an additional variation of the atomic positions. This state is referred to as **state B**. The third state, referred to as **state C**, is characterized by a clear change in symmetry to a tetragonal state with an elongated *c* axis. This transformation is already indicated after milling at 400 rpm for 12 h and becomes very prominent at a milling speed of 600 rpm, visible by the formation of new reflections around  $30^\circ 2\theta$ . A nearly complete transformation is observed after prolonged milling at 600 rpm.

## 2.1. Product States after Milling

### 2.1.1. State A: Anisotropic Reflection Broadening

The typical phase transformation of *ssr*-LMO to the orthorhombic low temperature phase is not present in *bm*-LMO. A com-

parison of low temperature in situ XRD patterns of *ssr*-LMO and *bm*-LMO is shown in Figure 6. Upon cooling, the splitting of the (311) reflection of *ssr*-LMO can be observed. The PXRD patterns of *bm*-LMO, in comparison, show no changes. The absence of a phase transformation is also confirmed by DSC measurements (Figure 6). In the DSC curve of *ssr*-LMO the expected signal corresponding to the phase transformation to the orthorhombic phase is visible at  $7^\circ\text{C}$ . The DSC curve of *bm*-LMO however reveals no signals.

Since in situ low temperature XRD and DSC measurements have demonstrated the absence of a phase transformation, a Rietveld refinement with an orthorhombic structure may be more adequate. To verify this, different structure models were investigated and compared (Figure 7). The fit quality was based on a comparison of the *weighted profile R-factors* ( $R_{wp}$ ) and, as an additional criterion, the *goodness of fit values* (*GOF*). The *GOF* is calculated from the ratio of the *weighted profile R-factor* ( $R_{wp}$ ) and the *expected R-factor* ( $R_{exp}$ ).<sup>[32]</sup>

The first refinement was conducted based on the ideal spinel structure and is shown in Figure 7a. As expected, a severe misfit

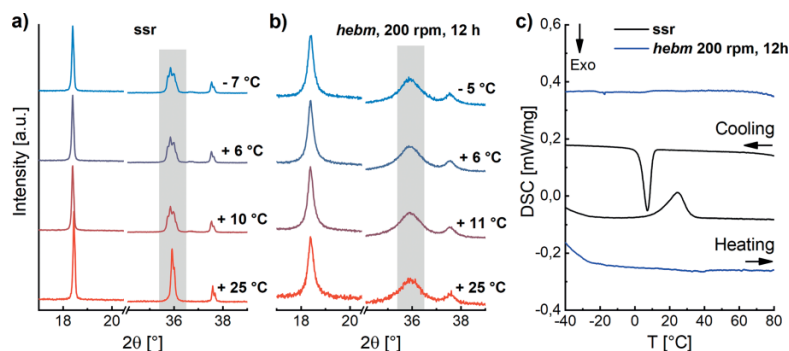


Figure 6. Occurrence and absence of the low temperature phase transition in un-milled (*ssr*) and milled (*hebm*, 200 rpm, 12 h)  $\text{LiMn}_2\text{O}_4$  respectively, as seen via low temperature in situ XRD and DSC measurements. (a) In situ XRD of un-milled (*ssr*)  $\text{LiMn}_2\text{O}_4$ , (b) in situ XRD of milled  $\text{LiMn}_2\text{O}_4$ , and (c) DSC curves of un-milled (black) and milled (blue)  $\text{LiMn}_2\text{O}_4$ .

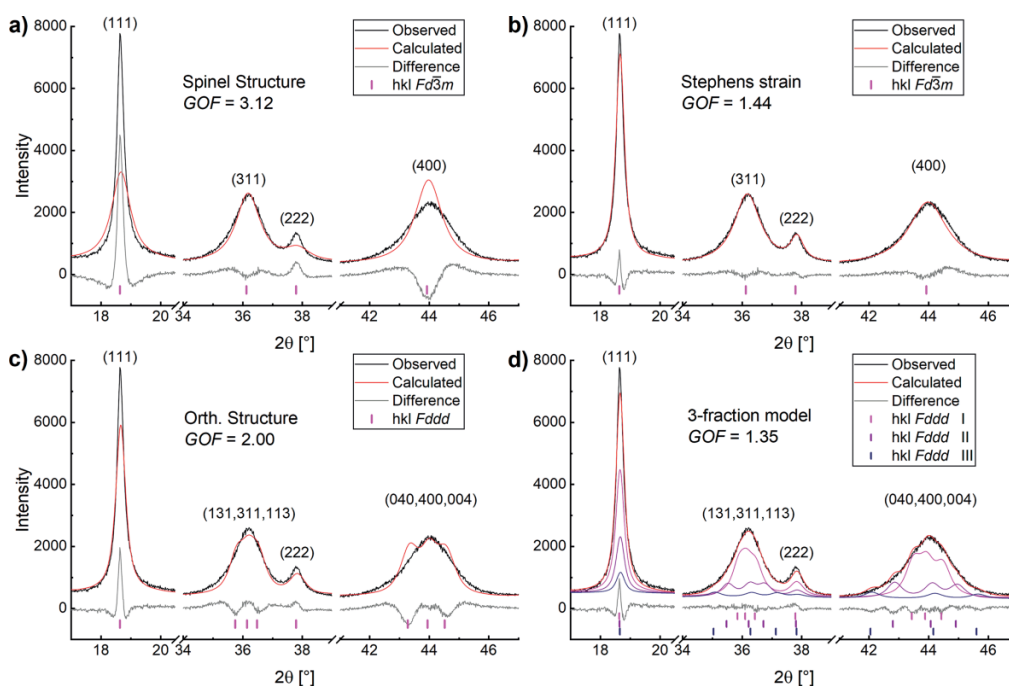


Figure 7. Rietveld refinements of milled  $\text{LiMn}_2\text{O}_4$  (200 rpm, 12 h) with (a) spinel structure, (b) spinel structure with Stephens strain model (as implemented in TOPAS 5), (c) orthorhombic structure, and (d) three-fraction model with orthorhombic structure.

is observed especially in the case of the (111) reflection. The misfit of the refinement is reflected by a high  $R_{wp}$  of 12.65 % and GOF of 3.12. The anisotropic broadening of the reflections can be better described by use of the Stephens strain model with cubic symmetry, as implemented in TOPAS 5.<sup>[33]</sup> This leads to a highly improved description of the line-shape, with an  $R_{wp}$  of 5.86 % and a GOF of 1.44 (Figure 7b). The Stephens model is based on the variation of lattice parameters, but it is difficult to derive this variation directly. To simulate this distribution more easily, a refinement of several independent lattice parameters is necessary. Therefore, the refinement was based on a pseudo cubic spinel structure with three independent lattice parameters, which is achieved by changing the space group of the spinel structure from  $Fd\bar{3}m$  to  $Fddd$ . Since the space group  $Fddd$  of the orthorhombic low temperature structure is a subgroup of  $I4_1/amd$ , which again is a subgroup of the space group  $Fd\bar{3}m$ , the atomic positions and initial lattice parameters were kept the same as in the spinel structure. This simple orthorhombic model now allows to simultaneously refine pseudo cubic, pseudo tetragonal and orthorhombic cells, which are directly comparable to each other.

It has already been shown by Hayakawa et al. that a refinement of the orthorhombic low temperature phase of  $\text{LiMn}_2\text{O}_4$  with a cell of similar volume as the spinel structure, yields a reasonable fit of X-ray diffraction data.<sup>[17]</sup> Additionally, the simple orthorhombic structure model leads to a lower number of parameters compared to the established  $Fddd$   $3 \times 3 \times 1$  superstructure, and therefore to a more stable refinement. This observation is confirmed by refinements of our in situ low temperature measurements of *ssr*-LMO. A refinement with the full

orthorhombic  $3 \times 3 \times 1$  superstructure model yields an  $R_{wp}$  of 7.23 % and a GOF of 1.29. A refinement with the simple orthorhombic model yields an  $R_{wp}$  of 8.45 % and a GOF of 1.50. The slight loss in fit quality is acceptable, since a faster and much more stable refinement is achieved.

Figure 7c shows a refinement based on the simple orthorhombic structure model. An improved fit compared to the ideal cubic spinel structure model in Figure 7a is achieved, however there are still significant misfits expressed by an  $R_{wp}$  of 8.11 % and a GOF of 2.00. Since the tailing of the (311) and (400) reflection group is still not accurately described a more nuanced variation of the lattice parameters is necessary. A multi-fraction model to describe the fluctuation of lattice parameters has already been described for a series of chlorovanadato-apatites and sodium vanadates.<sup>[24,25]</sup> To introduce additional increments, a refinement with three fractions of the proposed simple orthorhombic structure model is conducted. The nine generated lattice parameters are refined independently while the microstructural parameters (crystallite size and strain broadening) and atomic positions are constrained to be the same value for all fractions. This approach prevents an overparameterization of the refinement, while allowing to directly visualize the distribution of the lattice parameters. Additionally, this model allows to fit asymmetric reflections, since the median lattice parameters of the fractions are independent of each other. The result of the refinement is shown in Figure 7d and yields the best fit of the four refinement methods, with an  $R_{wp}$  of 5.49 % and a GOF of 1.35. The quality of the fit may be even further increased by applying an eleven-fraction model with equidistant fractions, simulating a probability distribution of

different lattice parameter sets.<sup>[25]</sup> Using this approach an  $R_{wp}$  of 5.14 %, a GOF of 1.27, and a much smoother peak profile can be obtained. However, this model does not allow the refinement of changes in the symmetry and the refinement speed is much lower. Therefore, we applied the three-fraction model with the simple orthorhombic structure and independent lattice parameters in our further studies.

The distribution of the lattice parameters obtained from the three-fraction model with the simple orthorhombic structure is shown in Figure 8. The lattice parameters range in total from 7.950(2) Å to 8.590(2) Å, with the weight of these parameters being 10 % (Fraction III). The weighted mean value is found to be 8.242 Å, which is quite close to the lattice parameter of ideal cubic spinel  $\text{LiMn}_2\text{O}_4$  of 8.245 Å applied as starting material in the milling process. The refined crystallite size  $\langle L \rangle$  is 35(1) nm.

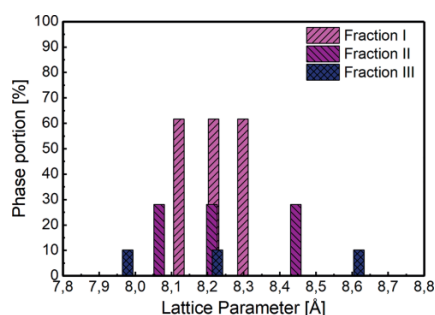


Figure 8. Distribution of lattice parameter from Rietveld refinement with three fractions of orthorhombic  $\text{LiMn}_2\text{O}_4$  with space group  $Fddd$ .

### 2.1.2. State B: Intensity Variation

As already mentioned, prolonged milling at 400 rpm induces an additional change of the relative reflection intensities. This is most probably caused by a change in the cation distribution. A cation disorder in mechanochemically synthesized  $\text{LiMn}_2\text{O}_4$  has already been proposed by Kosova et al. by  $^7\text{Li}$  solid-state NMR measurements.<sup>[13]</sup> To refine the cation distribution, the site occupation factors (*sof*) of the lithium and manganese positions were constrained to yield a stoichiometric composition of the sample, while the oxygen *sof* was kept constant. One additional manganese atom was defined at the lithium 8a site and one additional lithium atom at the manganese 16d site. To provide more clarity, the sites of the cations filling the tetrahedral or octahedral voids of the (distorted) cubic close packed oxygen layers are named  $\text{Li}_{\text{tet}}$  and  $\text{Mn}_{\text{oct}}$  in the following discussion. One *sof* was refined as a free parameter and the *sofs* of the remaining three atoms are constrained to ensure a constant electron density. The dependence of the *sofs* of the lithium and manganese sites is summarized in Table 1.

Table 1. Constraint to refine a combined *sof* of the lithium and manganese sites.

Site	WP	Atom	<i>sof</i>
$\text{Li}_{\text{tet}}$	8a	$\text{Li}^+$	$x$
		$\text{Mn}^{3.5+}$	$= 1 - x$
$\text{Mn}_{\text{oct}}$	16d	$\text{Mn}^{3.5+}$	$= 1/2 \cdot (1 + x)$
		$\text{Li}^+$	$= 1/2 \cdot (1 - x)$

The change of the relative intensities is very dominant in the sample milled at 400 rpm for 12 h (bm-LMO-400-12). The

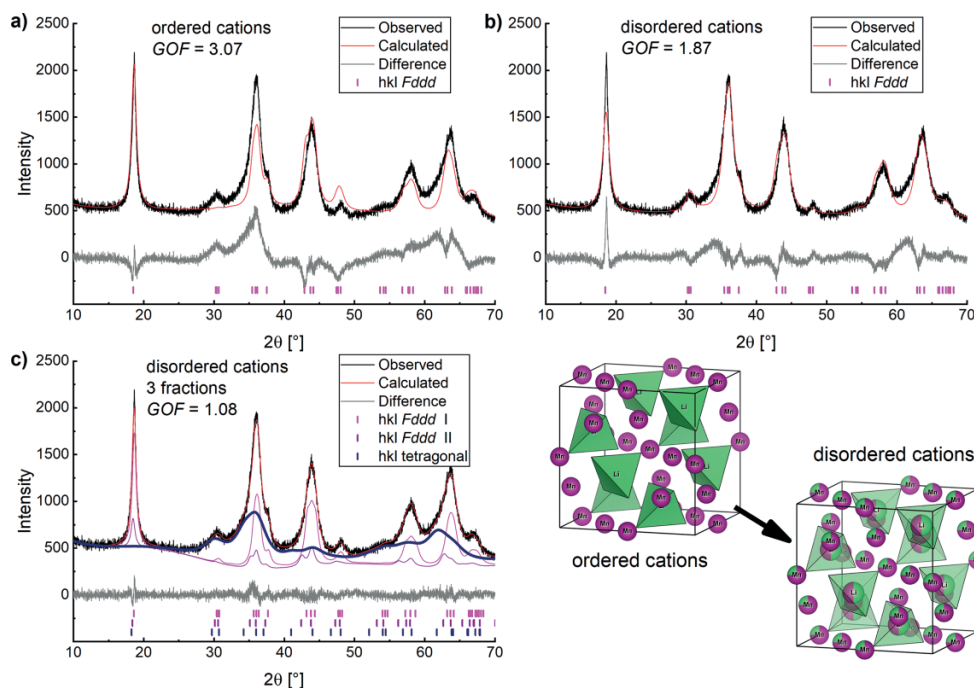


Figure 9. Rietveld refinements of bm-LMO-400-12 (milled  $\text{LiMn}_2\text{O}_4$ , 400 rpm, 12 h) with (a) single fraction orthorhombic structure, (b) disordered cation distribution, and (c) three-fraction model with disordered cation distribution. The structure illustration shows the cation disordering. Structure representations generated with VESTA.<sup>[16]</sup>

Table 2. Structure model to refine two constrained orthorhombic (I+II) and a tetragonal fraction (III), both with disordered cation distributions.

Frac.	Site	WP	x	y	z	Atom	sof	B <sub>iso</sub>
I+II	Li_tet1	8a	1/8	1/8	1/8	Li <sup>+</sup>	0.87(1)	1.5(1)
						Mn <sup>3.5+</sup>	0.13(1)	1.5(1)
	Mn_oct1	16d	1/2	1/2	1/2	Mn <sup>3.5+</sup>	0.93(1)	1.5(1)
						Li <sup>+</sup>	0.07(1)	1.5(1)
	O1	32e	0.2642(3)	0.2642(3)	0.2642(3)	O <sup>2-</sup>	1	1.3(1)
III	Li_tet2	8a	1/8	1/8	1/8	Li <sup>+</sup>	0.25(1)	1.5(1)
						Mn <sup>3.5+</sup>	0.75(1)	1.5(1)
	Mn_oct2	16d	1/2	1/2	1/2	Mn <sup>3.5+</sup>	0.62(1)	1.5(1)
						Li <sup>+</sup>	0.38(1)	1.5(1)
	O2	32e	0.241(1)	0.241(1)	0.241(1)	O <sup>2-</sup>	1	1.3(1)

differences in the refinements with and without a cation disorder is presented in Figure 9. A refinement with a single fraction of the simple orthorhombic model with an ideal spinel cation distribution ( $x = 0$ ) is shown in Figure 9a. While the intensity of the first reflection is calculated accurately, the intensities of the following reflections are severely mismatched. A refinement with a single fraction of the simple orthorhombic model with a cation disorder within the scope of the proposed constraint is shown in Figure 9b. The relative intensities of the reflections are described more accurately by this model. In Figure 9c a refinement with the three-fraction model is shown. In contrast to the milling products at 400 rpm with up to 6 h milling time, only two of the fractions show lattice parameters that are still close to the cubic spinel after 12 h milling time. The third fraction exhibits two lattice parameters being nearly identical ( $a = b = 8.219(3)$  Å) and a third being much longer ( $c = 8.796(8)$  Å). It may be assumed that a new phase with tetragonal symmetry is forming. To accommodate this, the microstructure and cation distribution of fraction III was refined independently from fraction I and II. A weight portion of 58 % is refined for the pseudo tetragonal fraction III, while fraction I and II account for 33 % and 9 %, respectively. The refined crystallite size  $\langle L \rangle$  of fraction I and II is 11.2(2) nm. To highlight the portion of the pseudo tetragonal fraction III, the line was plotted thicker. Since the reflections are extremely broad it may be assumed that very small domains with tetragonal symmetry are formed. The refined crystallite size  $\langle L \rangle$  of fraction III is 3.3(1) nm.

The resulting cation distribution of the refinement with the revised three-fraction model is shown in Table 2. The constrained fractions I and II are still close to the cation distribution of the normal spinel and exhibit a disorder of more than 25 %. The now independent and tetragonal fraction III on the other hand shows a cation distribution more similar to an inverse spinel structure, with the 8a site being occupied mostly by manganese.

### 2.1.3. State C: Phase Transformation

After milling LiMn<sub>2</sub>O<sub>4</sub> with PPA at 600 rpm for 12 h (bm-LMO-600-12) the proposed pseudo tetragonal state has formed with sharper reflections (Figure 10). A phase portion of 87 % is refined. The crystallite size is determined to be 7.1(2) nm. The remains of fraction I and II accommodate the shape of residual reflections intensities that may still arise from the presence of small portions of LiMn<sub>2</sub>O<sub>4</sub> with orthorhombic symmetry or pseudo tetragonal symmetry with a less distinct splitting. The

pseudo tetragonal main phase exhibits a reflection broadening mostly dominated by the crystallite size. The strain contribution is quite low and no anisotropic broadening of the reflections was detected. The complete refinement parameters of the tetragonal phase are summarized in the supporting information in Table S1 1.

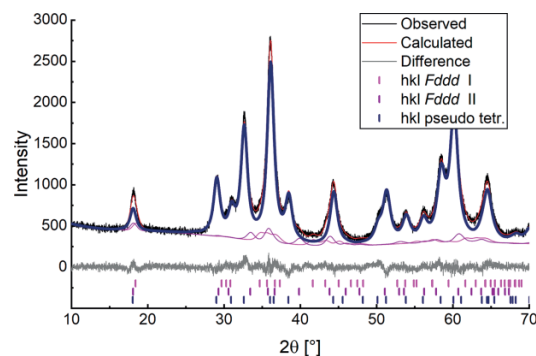


Figure 10. Rietveld refinement of bm-LMO-600-12 (milled LiMn<sub>2</sub>O<sub>4</sub>, 600 rpm, 12 h) with a three-fraction model with disordered cation distribution.

The reflection pattern of the formed phase is very similar to that of tetragonal Hausmannite Mn<sub>3</sub>O<sub>4</sub> with space group  $I4_1/amd$ . To exclude the possibility that pure Mn<sub>3</sub>O<sub>4</sub> has formed, the lattice parameters, lattice ratios, and cell volumes of both phases can be compared. The Mn<sub>3</sub>O<sub>4</sub> structure is a tetragonal distorted spinel structure and directly related to the cubic spinel structure via the symmetry reduction from the space group  $Fd\bar{3}m$  to  $I4_1/amd$ . The spinel *aristo* structure (and the proposed simple orthorhombic *Fddd* structure model) can be represented as  $\sqrt{2}x\sqrt{2}x1$  superstructure of the tetragonal  $I4_1/amd$  structure. The lattice parameters are summarized in Table 3.

Table 3. Lattice parameters of bm-LMO-600-12 compared to the lattice parameters of a Mn<sub>3</sub>O<sub>4</sub> reference sample from a solid-state reaction (ssr).

Phase	<i>a</i> [Å]	<i>c</i> [Å]	<i>c/a</i>	<i>V</i> [Å <sup>3</sup> ]
bm-LMO-600-12	5.7777(5) $\cdot\sqrt{2}$	9.3652(8)	1.621	312.6(1)
ssr-Mn <sub>3</sub> O <sub>4</sub>	5.76237(2)	9.47011(3)	1.643	314.45(1)

It can be seen that sample bm-LMO-600-12 exhibits a lower cell volume than Mn<sub>3</sub>O<sub>4</sub>. The *a* lattice parameter of the milled product is longer, while the *c* axis is much shorter. Since the tetragonal splitting of Mn<sub>3</sub>O<sub>4</sub> is caused by the Jahn-Teller distortion of the Mn(III) cations, a less pronounced splitting suggests

a lower Mn(III) content in the bm-LMO-600-12 sample. It is assumed that this difference is caused by the lithium content. A refinement of the constrained *sof* indicates that 30 % of lithium is located in the tetrahedral voids and 70 % in the octahedral voids. This observation is again an indication for a lower Mn(III) content, since Mn(III) is located in the octahedral voids and therefore substituted by lithium. A tetrahedral coordination of Mn(III) is very unlikely. This is however based on the assumption of an unchanged  $\text{LiMn}_2\text{O}_4$  stoichiometry. The lithium content may be lower than 1 but is most certainly higher than 0 based on the refined lattice parameters and *sof*. A co-refinement of X-ray and neutron powder data, which will be published elsewhere, yields a lithium content of approximately 0.6 (i.e.  $\text{Li}_{0.6}\text{Mn}_{2.4}\text{O}_4$ ).

## 2.2. Thermal Stability

The thermal stability of the three proposed product states is evaluated via in situ high temperature PXRD experiments. The products obtained from milling at 200, 400, and 600 rpm for 12 h were selected as representative samples. The sample milled at 200 rpm (bm-LMO-200-12) is dominated by the anisotropic reflection broadening. The sample milled at 400 rpm (bm-LMO-400-12) is additionally affected by intensity changes, correlated to the cation disorder. The sample milled at 600 rpm (bm-LMO-600-12) represents the state of the transformation to the tetragonal phase. A heat map of the in situ XRD data of the bm-LMO-200-12 sample is shown in Figure 11. The heat maps of the samples bm-LMO-400-12 and bm-LMO-600-12 are shown in the supporting information Figure SI 3 and Figure SI 4, respectively.

The heat map of bm-LMO-200-12 reveals only gradual changes of the pattern up to a temperature of 300 °C. From 300 °C new reflections start to emerge up to about 450 °C, where the former main reflections have nearly vanished. A change back to the initial reflection pattern can be observed with increasing temperature. At 600 °C a pattern with sharper reflections than the milled product is obtained. Additional reflections are visible, indicating the formation of a side phase. The samples milled at 400 and 600 rpm behave similarly, though the change of the initial pattern and the formation of new reflections is observed at lower temperature with increasing milling speed. Rietveld refinement with the proposed three-fraction model with the simple orthorhombic structure was applied to all recorded patterns to follow the thermal induced changes in the patterns. This allows a simultaneous refinement of anisotropic reflection broadening, cation distribution and formation of phases with pseudo cubic, pseudo tetragonal and orthorhombic symmetry. The collected results, in the form of phase portions and lattice parameters for the three fractions, are summarized in Figure 12, Figure 13, and Figure 14 for the products milled at 200, 400 and 600 rpm, respectively.

For sample bm-LMO-200-12, no significant changes of the lattice parameters or the phase portions of the three fractions are visible up to a temperature of 200 °C. Only an expectable thermal expansion of the lattice can be interpreted. The crystallite  $\langle L \rangle$  remains around 33 nm in this temperature range. At 250 °C, the crystallite size increases to 51(1) nm. Additionally, two nearly identical lattice parameters are refined for fraction III. To adjust the refinement, these were constrained to be equal and the microstructure of fraction III was refined independently from fraction I and II. Since the third lattice parameters be-

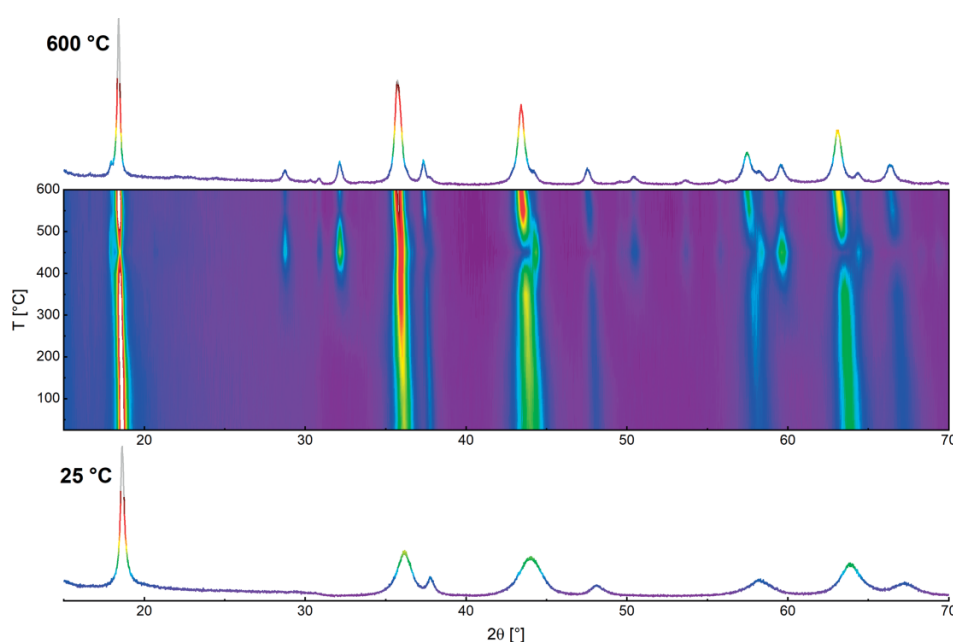


Figure 11. In situ XRD measurements of  $\text{LiMn}_2\text{O}_4$  after milling with PPA at 200 rpm for 12 h. The lower pattern was recorded before heating and the upper pattern was recorded at 600 °C.

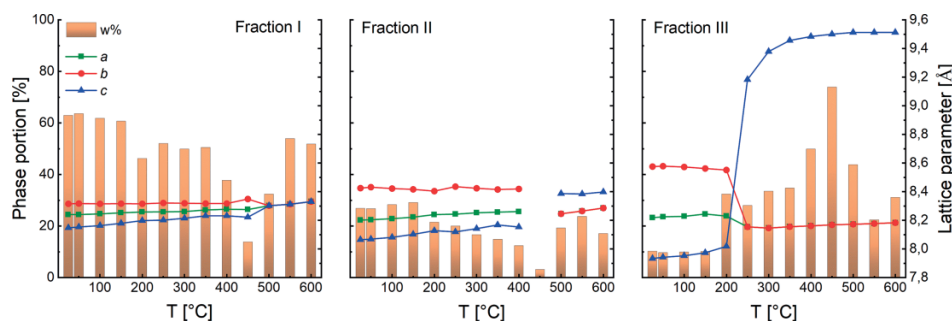


Figure 12. Phase portions (orange bars) and lattice parameters (green, red and blue lines) from Rietveld refinement of the in situ XRD measurements with the three-fraction model.  $\text{LiMn}_2\text{O}_4$  milled at **200 rpm** for 12 h.

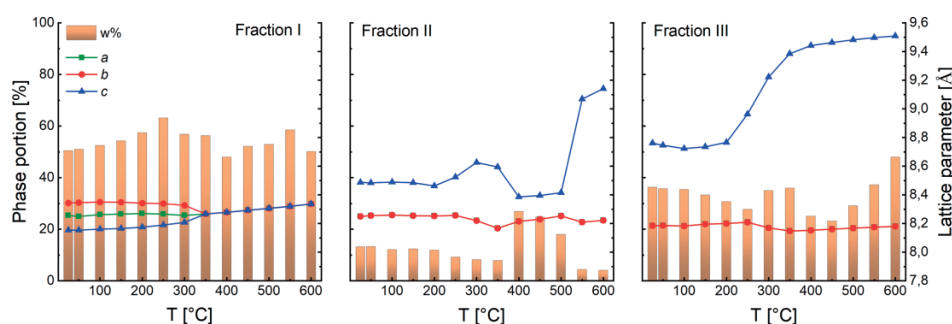


Figure 13. Phase portions (orange bars) and lattice parameters (green, red and blue lines) from Rietveld refinement of the in situ XRD measurements with the three-fraction model.  $\text{LiMn}_2\text{O}_4$  milled at **400 rpm** for 12 h.

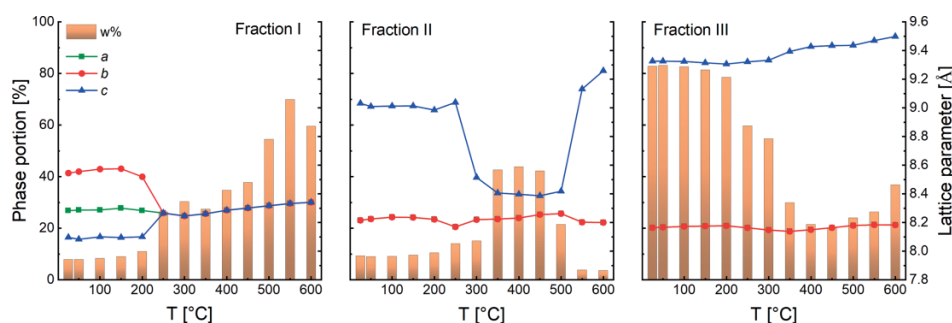


Figure 14. Phase portions (orange bars) and lattice parameters (green, red and blue lines) from Rietveld refinement of the in situ XRD measurements with the three-fraction model.  $\text{LiMn}_2\text{O}_4$  milled at **600 rpm** for 12 h.

comes much longer, it may be assumed that a tetragonal phase appears that is similar to the phase formed after milling at 600 rpm for 12 h. The crystallite size of the tetragonal fraction III is refined to 2.6(2) nm. The phase portion and crystallite size of the tetragonal phase increase rapidly with increasing temperature until a maximum is reached at 450 °C. A portion of 73 % and a crystallite size of 20(1) nm is refined. In contrast, the crystallite size of fraction I and II decreases slightly to 41(1) nm. The phase portion of fraction II is very low at this point. Therefore, a reliable refinement of the lattice parameters was not possible. The orthorhombic splitting of the lattice parameters of fraction I becomes larger, probably to compensate the low amount of fraction II. Additionally, new reflections correspond-

ing to the lithium rich phase  $\text{Li}_2\text{MnO}_3$  can be refined with a phase portion of about 10 %. This indicates a segregation of the initially single-phase product. The formation of  $\text{Li}_2\text{MnO}_3$  has also been observed by in situ high temperature XRD of cubic spinel  $\text{LiMn}_2\text{O}_4$  to temperatures above 900 °C.<sup>[34]</sup> To exclude the formation of pure tetragonal  $\text{Mn}_3\text{O}_4$  as fraction III, cell parameters of a  $\text{Mn}_3\text{O}_4$  reference sample were refined over the complete temperature range of the in situ XRD measurements. Pure  $\text{Mn}_3\text{O}_4$  reveals a volume constantly about  $2 \text{ \AA}^3$  larger than that of fraction III. This indicates that the formed tetragonal phase at least partly contains lithium. However, the lithium content is probably lower than in  $\text{LiMn}_2\text{O}_4$ . The overall cell volume of fraction III is much larger than of fraction I and II, which may be

based on a higher Mn(III) content. Further heating to 500 °C induces a decrease of the phase portion of fraction III and an increase of fraction I and II. It is assumed that the probable lithium poor fraction III reacts with  $\text{Li}_2\text{MnO}_3$  as the phase portion of the latter decreases significantly and vanishes completely in the next heating step. Since the splitting of the lattice parameters of fraction I decreases significantly, the three parameters were constrained to refine a cubic state. Fraction II now too exhibits two nearly identical lattice parameters and presumably compensates the still slightly anisotropic broadened reflections of the spinel pattern. The last heating steps up to 600 °C reveal no changes of lattice parameters except for the thermal expansion. The final crystallite sizes are 78(1) nm for fraction I and II and 30(1) nm for fraction III.

The changes in phase composition of the sample bm-LMO-400–12 (Figure 13) show a different behavior than sample bm-LMO-200–12. For sample bm-LMO-400–12 the microstructural parameters of fraction I and II are constrained, while fraction III is refined independently from the start. Additionally, fraction II and III are refined with tetragonal symmetry over the complete temperature range (lattice parameter  $a$  and  $b$  constrained).

The crystallite size of fraction I and II remains around 10 nm over the complete temperature range up to 600 °C. A final crystallite size of 13(1) nm is refined. The crystallite size of fraction III is 3.3(2) nm and increases to 27(1) nm at 600 °C. The transformation to cubic  $\text{LiMn}_2\text{O}_4$  is found to occur at 350 °C. As soon as fraction I is refined with a cubic constraint of the lattice parameters, the tetragonal splitting of fraction II is decreased significantly in both samples. This is comparable to sample bm-LMO-200–12, since fraction II compensates the still slightly anisotropic reflection broadening of the cubic reflection pattern. Additionally, the phase portion of fraction II increases significantly in this way. Contrary to sample bm-LMO-200–12, no reflections of the lithium rich phase  $\text{Li}_2\text{MnO}_3$  are observed for sample bm-LMO-400–12. Sample bm-LMO-600–12 (Figure 14) behaves very similar to sample bm-LMO-400–12. The same refinement constraints as described for sample bm-LMO-400–12 have been applied.

The crystallite size of fraction I+II and III is 7 nm in the beginning and increases to 18 and 20 nm respectively at 600 °C. The transformation to cubic  $\text{LiMn}_2\text{O}_4$  is found to occur at an even lower temperature of 250 °C for sample bm-LMO-600–12. Overall, at 600 °C, all samples from 200 to 400 and 600 rpm milling speed show a consistent composition. The phase portion of the pseudo tetragonal fraction III is between 35 and 40 % and the phase portion of fraction II is very low. The lattice parameters of the pseudo tetragonal fraction III and the pseudo cubic fraction I is similar for each sample.

### 3. Conclusion

Phenylphosphonic acid functionalized nanocrystalline  $\text{LiMn}_2\text{O}_4$  has been produced by dry milling of coarse-grained  $\text{LiMn}_2\text{O}_4$  from a solid-state reaction with the respective phosphonic acid. The X-ray diffraction (XRD) patterns of the products are dominated by anisotropic reflection broadening, intensity changes,

and formation of new reflections. A concise and versatile Rietveld refinement model to accommodate the XRD peak shapes has been proposed. The model is able to simultaneously describe the features of the patterns that are caused by a distribution of lattice parameters, cation disorder and formation of phases with orthorhombic, tetragonal and cubic symmetry. The thermal induced changes of the XRD patterns can also be described with this model.

## 4. Experimental Section

### 4.1. Materials

$\text{Li}_2\text{CO}_3$  (Merck, Darmstadt, Germany, 99 %),  $\text{MnCO}_3$  (Alfa Aesar GmbH, Karlsruhe, Germany, 99.9 %),  $\text{Mn}_2\text{O}_3$  (ChemPur, Karlsruhe, Germany, 99.9 %), phenylphosphonic acid (Sigma-Aldrich Chemie GmbH, Steinheim, Germany, 98 %), 2-propanol (Biesterfeld Spezialchemie, Hamburg, Germany, 97 %) and  $n$ -pentane (Sigma Aldrich, Steinheim, Germany, 99 %) were used as received. All precursor solids have been characterized by PXRD before use.

### 4.2. Sample Preparation

Spinel  $\text{LiMn}_2\text{O}_4$  was synthesized via standard solid-state reaction from  $\text{Li}_2\text{CO}_3$  and  $\text{Mn}_2\text{O}_3$ .<sup>[4]</sup> Stoichiometric amounts of the starting materials were homogenized by wet milling with  $n$ -pentane in an agate jar (volume of 50 mL) with 10 milling balls (diameter of 10 mm) of the same material. The powder mixture was milled at 400 rpm for 30 min. The mixture was dried in air and heated to 800 °C for 8 h in a platinum crucible.  $\text{Mn}_3\text{O}_4$  reference material with the Hausmannite structure was synthesized by heating  $\text{MnCO}_3$  in a platinum crucible to 1100 °C in air.<sup>[35]</sup> To prevent the formation of  $\text{Mn}_2\text{O}_3$  the sample was quenched by removing the crucible from the hot furnace.

High energy ball milling was conducted with a planetary ball mill, type PM100 (Retsch, Germany). A grinding jar (volume of 50 mL) made of yttrium stabilized zirconia and 200 milling balls (diameter of 5 mm) of the same material were used. Approximately 3 g of starting powder were used, corresponding to a ball to powder weight ratio of 27:1. In-situ surface functionalization was achieved by adding 10 wt.-% phenylphosphonic acid. In the case of pure  $\text{LiMn}_2\text{O}_4$ , 200  $\mu\text{L}$  of 2-propanol were added as dispersing agent to prevent cementing of the powder. The rotational speed of the mill was set to 200, 400 or 600 rpm.

### 4.3. Characterization

Powder X-ray diffraction (PXRD) patterns were recorded on a Bruker D8 Advance diffractometer (Bruker, Karlsruhe, Germany) in  $\theta$ - $\theta$  geometry (goniometer radius 280 mm) with  $\text{Cu-K}\alpha$  radiation ( $\lambda = 154.0596$  pm, 40 kV, 40 mA). A 12  $\mu\text{m}$  Ni foil was used to reduce  $\text{K}\beta$  radiation. A variable divergence slit was mounted at the primary beam side (irradiated sample area of  $10 \times 7$  mm). A LYNXEYE 1D detector was used at the secondary beam side. The background caused by white radiation and sample fluorescence was reduced by limiting the energy range of the detection.

Standard measurements were carried out in a  $2\theta$  range of 7 to 120° with a step size of 0.013° and a total scan time of 2 h. In situ low temperature XRD was realized by using a self-constructed sample holder with thermoelectric cooling via Peltier device. Measurements were carried out under air in a  $2\theta$  range of 7 to 145° with a step size of 0.013° and a total scan time of 1 h. In situ high temperature XRD was realized by using an Anton Paar X-ray reaction chamber XRK900 (Anton Paar GmbH, Graz, Austria). Measurements were car-

ried out under a vacuum of 0.02 mbar in a  $2\theta$  range of 7 to 110° with a step size of 0.013° and a total scan time of 1 or 2 h. The temperature was varied in 25 or 50 K steps with a heating rate of 10 K/min up to a temperature of 600 °C.

Interpretation of the XRD data was achieved via the Rietveld method using TOPAS 5.<sup>[36–38]</sup> Crystallographic structure and microstructure were refined, while instrumental line broadening was included in a fundamental parameters approach.<sup>[39]</sup> The mean crystallite size  $\langle L \rangle$  was calculated at the mean volume weighted column height derived from the integral breadth. The background of standard measurements was fitted by a Chebyshev polynomial function of 15<sup>th</sup> degree. The background of in situ high temperature measurements was fitted by a  $1/x$ -function together with a Chebyshev polynomial function of 5<sup>th</sup> degree and two additional hat functions to correct the specific background profile present in all measurements. Crystal structure data were obtained from the crystallography open database (COD) and the inorganic crystal structure database (ICSD).<sup>[40,41]</sup>

FT-IR spectra were recorded on a Bruker Vertex 70 IR spectrometer (Bruker, Karlsruhe, Germany) in attenuated total reflection mode under ambient conditions. Spectra were recorded from 4000 to 400  $\text{cm}^{-1}$  with a resolution of 4  $\text{cm}^{-1}$  and 40 scans per spectrum.

Dynamic scanning calorimetry (DSC) was conducted with a Netzsch Phoenix 204 F1 (NETZSCH-Gerätebau GmbH, Selb, Germany). Measurements were carried out in aluminum crucibles under pure nitrogen and in a temperature range from –50 °C to 100 °C with a heating rate of 10 K/min.

## Acknowledgments

We would like to thank Christina Odenwald for recording the SEM photographs.

**Keywords:** Solid-state reactions · Phase transitions · Reactive milling · Rietveld refinement · Structure elucidation

- [1] M. M. Thackeray, *J. Am. Ceram. Soc.* **2004**, *82*, 3347–3354.
- [2] C. Daniel, D. Mohanty, J. Li, D. L. Wood, *AIP Conf. Proc.* **2014**, *1597*, 26–43.
- [3] D. G. Wickham, W. J. Croft, *J. Phys. Chem. Solids* **1958**, *7*, 351–360.
- [4] M. M. Thackeray, W. I. F. David, P. G. Bruce, J. B. Goodenough, *Mater. Res. Bull.* **1983**, *18*, 461–472.
- [5] N. Nitta, F. Wu, J. T. Lee, G. Yushin, *Mater. Today* **2015**, *18*, 252–264.
- [6] Y.-M. Hon, K.-Z. Fung, M.-H. Hon, *J. Ceram. Soc. Jpn.* **2000**, *108*, 462–468.
- [7] Y. Hon, S. Lin, K. Fung, M. Hon, *J. Eur. Ceram. Soc.* **2002**, *22*, 653–660.
- [8] C. H. Lu, S. K. Saha, *J. Sol-Gel Sci. Technol.* **2001**, *20*, 27–34.
- [9] X. Li, F. Cheng, B. Guo, J. Chen, *J. Phys. Chem. B* **2005**, *109*, 14017–14024.
- [10] S. L. James, C. J. Adams, C. Bolm, D. Braga, P. Collier, T. Frii, F. Grepioni, K. D. M. Harris, G. Hyett, W. Jones, et al., *Chem. Soc. Rev.* **2012**, *41*, 413–447.
- [11] N. V. Kosova, N. F. Uvarov, E. T. Devyatkina, E. G. Avvakumov, *Solid State Ionics* **2000**, *135*, 107–114.
- [12] H.-J. Choi, K.-M. Lee, G.-H. Kim, J.-G. Lee, *J. Am. Ceram. Soc.* **2001**, *84*, 242–244.
- [13] N. V. Kosova, E. T. Devyatkina, S. G. Kozlova, *J. Power Sources* **2001**, *97–98*, 406–411.
- [14] S.-H. Kang, J. B. Goodenough, L. K. Rabenberg, *Chem. Mater.* **2001**, *13*, 1758–1764.
- [15] N. Kamarulzaman, R. Yusoff, N. Kamarudin, N. H. Shaari, N. A. Abdul Aziz, M. A. Bustam, N. Blagojevic, M. Elcombe, M. Blackford, M. Avdeev, et al., *J. Power Sources* **2009**, *188*, 274–280.
- [16] K. Momma, F. Izumi, *J. Appl. Crystallogr.* **2011**, *44*, 1272–1276.
- [17] H. Hayakawa, T. Takada, H. Enoki, E. Akiba, *J. Mater. Sci. Lett.* **1998**, *17*, 811–812.
- [18] V. Massarotti, D. Capsoni, M. Bini, P. Scardi, M. Leoni, V. Baron, H. Berg, *J. Appl. Crystallogr.* **1999**, *32*, 1186–1189.
- [19] J. Akimoto, Y. Takahashi, Y. Gotoh, S. Mizuta, *Chem. Mater.* **2000**, *12*, 3246–3248.
- [20] K. Kodama, N. Igawa, S. I. Shamoto, K. Ikeda, H. Oshita, N. Kaneko, T. Otomo, K. Suzuya, *J. Phys. Soc. Jpn.* **2013**, *82*, 1–6.
- [21] A. Paolone, A. Sacchetti, P. Postorino, R. Cantelli, A. Congeduti, G. Rouse, C. Masquelier, *Solid State Ionics* **2005**, *176*, 635–639.
- [22] W. I. F. David, M. M. Thackeray, L. A. De Picciotto, J. B. Goodenough, *J. Solid State Chem.* **1987**, *67*, 316–323.
- [23] P. Strobel, F. Le Cras, L. Seguin, M. Anne, J. M. Tarascon, *J. Solid State Chem.* **1998**, *135*, 132–139.
- [24] H. P. Beck, M. Douiheche, R. Haberkorn, H. Kohlmann, *Solid State Sci.* **2006**, *8*, 64–70.
- [25] R. Haberkorn, J. Bauer, G. Kickelbick, *Z. Anorg. Allg. Chem.* **2014**, *640*, 3197–3202.
- [26] A. Fischer, C. Ney, G. Kickelbick, *Eur. J. Inorg. Chem.* **2013**, *2013*, 5701–5707.
- [27] A. Betke, G. Kickelbick, *New J. Chem.* **2014**, *38*, 1264–1270.
- [28] A. Betke, G. Kickelbick, *Inorganics* **2014**, *2*, 410.
- [29] G. Guerrero, P. H. Mutin, A. Vioux, *Chem. Mater.* **2001**, *13*, 4367–4373.
- [30] A. M. Botelho do Rego, A. M. Ferraria, J. El Beghdadi, F. Debontridder, P. Brogueira, R. Naaman, M. Rei Vilar, *Langmuir* **2005**, *21*, 8765–8773.
- [31] M. D. Lane, P. R. Christensen, *J. Geophys. Res. Planets* **1997**, *102*, 25581–25592.
- [32] B. H. Toby, *Powder Diffr.* **2006**, *21*, 67–70.
- [33] P. W. Stephens, *J. Appl. Crystallogr.* **1999**, *32*, 281–289.
- [34] M. M. Thackeray, M. F. Mansuetto, D. W. Dees, D. R. Vissers, *Mater. Res. Bull.* **1996**, *31*, 133–140.
- [35] R. Perthel, H. Jahn, *Phys. status solidi* **1964**, *5*, 563–568.
- [36] H. M. Rietveld, *Acta Crystallogr.* **1967**, *22*, 151–152.
- [37] H. M. Rietveld, *J. Appl. Crystallogr.* **1969**, *2*, 65–71.
- [38] *Topas 5*, Bruker AXS, Karlsruhe, Ger. **2014**.
- [39] R. W. Cheary, A. A. Coelho, J. P. Cline, *J. Res. Natl. Inst. Stand. Technol.* **2004**, *109*, 1–25.
- [40] S. Gražulis, D. Chateigner, R. T. Downs, A. F. T. Yokochi, M. Quirós, L. Lutterotti, E. Manakova, J. Butkus, P. Moeck, A. Le Bail, *J. Appl. Crystallogr.* **2009**, *42*, 726–729.
- [41] A. Belsky, M. Hellenbrandt, V. L. Karen, P. Luksch, *Acta Crystallogr., Sect. B Struct. Sci.* **2002**, *58*, 364–369.

Received: September 2, 2019



## Supporting Information

### **Reactive Milling Induced Structure Changes in Phenylphosphonic Acid Functionalized $\text{LiMn}_2\text{O}_4$ Nanocrystals – Synthesis, Rietveld Refinement, and Thermal Stability**

Dennis Becker, Robert Haberkorn, and Guido Kickelbick\*

[ejic201900946-sup-0001-SupMat.pdf](#)

- FT-IR spectra of  $\text{LiMn}_2\text{O}_4$  after milling with PPA at 200 and 600 rpm.
- Refined structure parameters of (pseudo)tetragonal  $\text{LiMn}_2\text{O}_4$  obtained after milling at 600 rpm.
- 2D plots of in situ XRD measurements of  $\text{LiMn}_2\text{O}_4$  after milling with PPA at 400 and 600 rpm.

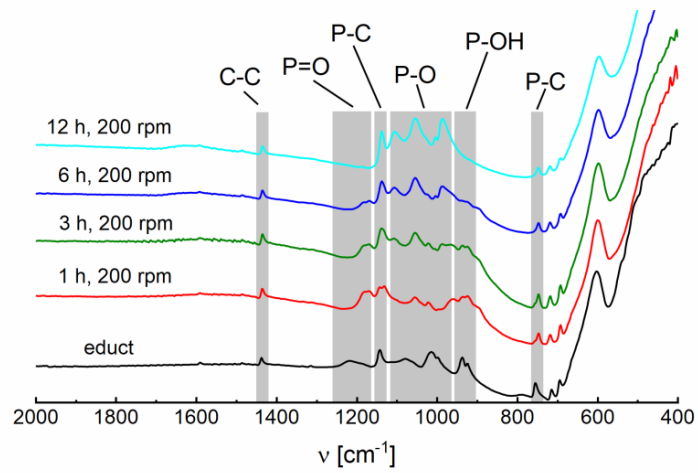


Figure SI 1: FT-IR spectra of  $\text{LiMn}_2\text{O}_4$  with PPA before (educt) and after milling at 200 rpm for different milling times.

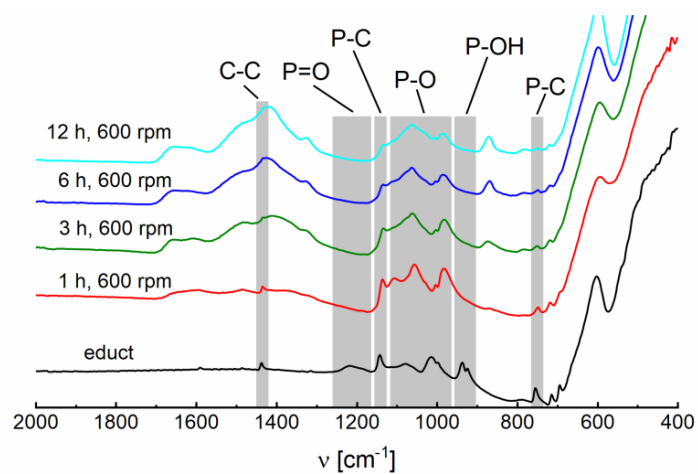


Figure SI 2: FT-IR spectra of  $\text{LiMn}_2\text{O}_4$  with PPA before (educt) and after milling at 600 rpm for different milling times.

## 8 Reactive Milling Induced Structure Changes in Phenylphosphonic acid Functionalized $\text{LiMn}_2\text{O}_4$ Nanocrystals – Synthesis, Rietveld refinement and Thermal Stability

Table SI 1: Refined structure parameters of the tetragonal fraction III obtained after milling  $\text{LiMn}_2\text{O}_4$  with PPA at 600 rpm for 12 h. Global refinement parameters: number of independent parameters = 41,  $R_{wp} = 4.90\%$ ,  $R_{exp} = 4.09\%$ ,  $GOF = 1.20$ . WP= Wyckoff position, sof = site occupation factor.

SG	Fddd 2							
$R_{Bragg}$	1.22%							
Wt% Rietveld	86.7(5)							
Cell Mass	1446.518							
Cell Volume [ $\text{\AA}^3$ ]	625.3(1)							
$a$ [ $\text{\AA}$ ]	8.1708(5)							
$b$ [ $\text{\AA}$ ]	= $a$							
$c$ [ $\text{\AA}$ ]	9.3652(8)							
Crystallite Size $L_{vol-IB}$ [nm]	7.1(1)							
Strain $\varepsilon_0$	0.0009(1)							
Lin. Abs. Coeff. [ $\text{cm}^{-1}$ ]	644.7(1)							
Crystal Density [ $\text{g/cm}^3$ ]	3.842(1)							
Frac.	Site	WP	$x$	$y$	$z$	Atom	sof	$B_{iso}$
III	Li_tet2	8a	1/8	1/8	1/8	Li <sup>+</sup>	0.31(1)	1.16(4)
						Mn <sup>3.5+</sup>	0.69(1)	1.16(4)
	Mn_oct2	16d	1/2	1/2	1/2	Mn <sup>3.5+</sup>	0.65(1)	1.16(4)
						Li <sup>+</sup>	0.35(1)	1.16(4)
	O2	32e	0.2594(2)	0.2594(2)	0.2594(2)	O <sup>2-</sup>	1	3.91(6)

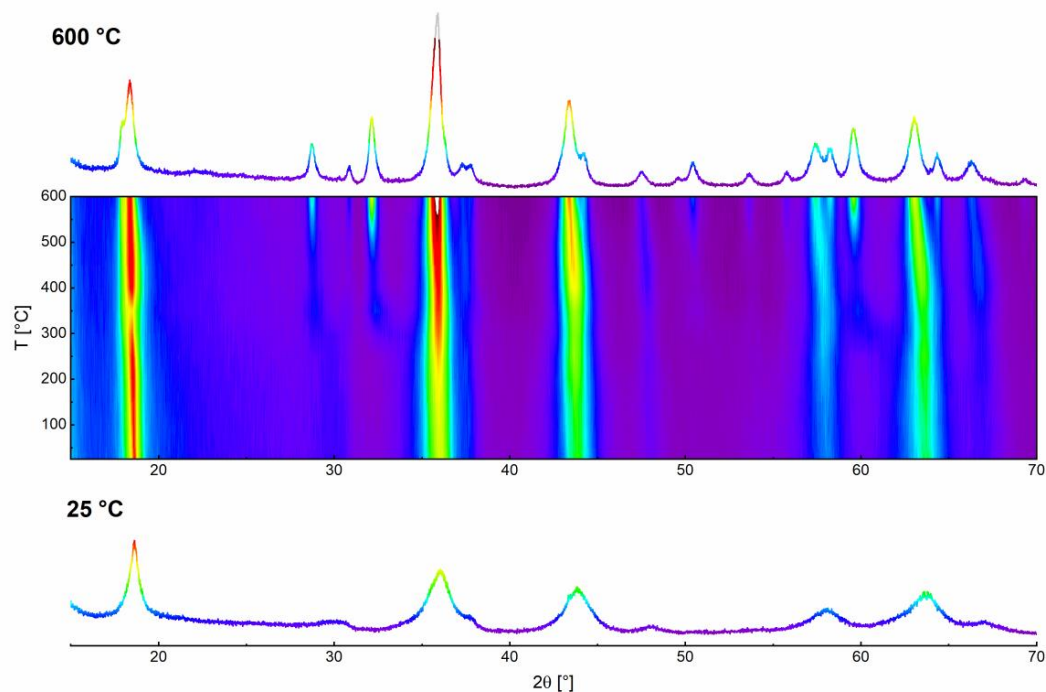


Figure SI 3: In situ XRD measurements of  $\text{LiMn}_2\text{O}_4$  after milling with PPA at 400 rpm for 12 h. Lower pattern was recorded before heating; upper pattern was recorded at 600 °C.

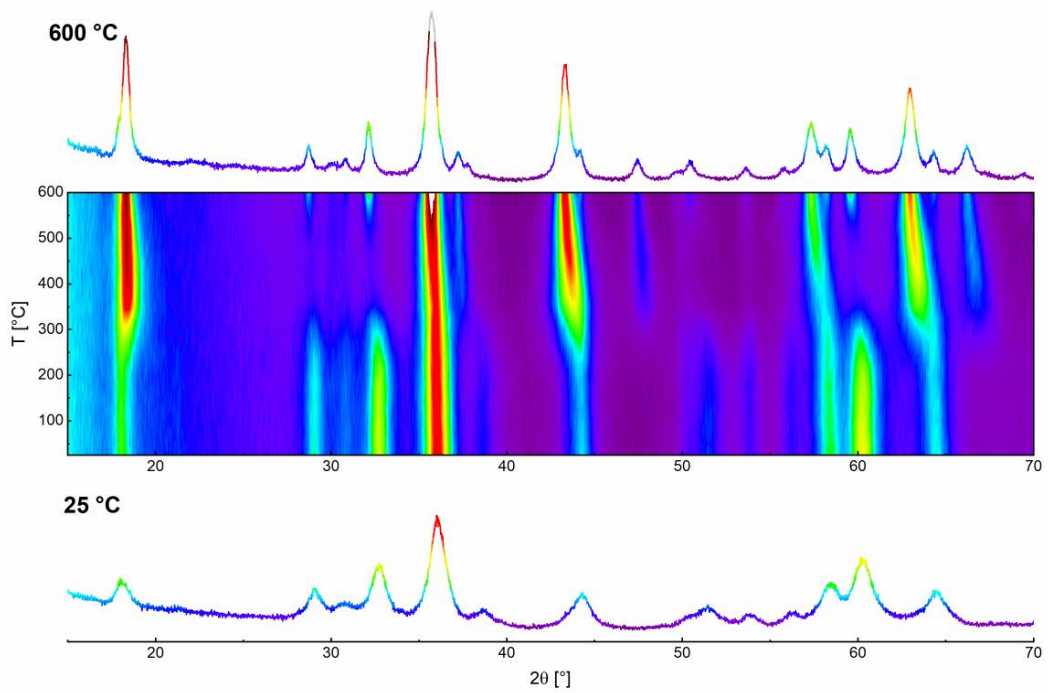


Figure SI 4: In situ XRD measurements of  $\text{LiMn}_2\text{O}_4$  after milling with PPA at 600 rpm for 12 h. Lower pattern was recorded before heating; upper pattern was recorded at  $600\text{ }^\circ\text{C}$ .



## 9 Summary and Outlook

Mechanochemical syntheses have been developed to produce nanocrystalline cubic  $\alpha$ - $\text{Li}_2\text{TiO}_3$  and  $\text{Mn}_3\text{O}_4$  from simple, monovalent oxides. The optimal synthesis parameters in terms of grinding tool materials, milling speed, and milling time have been deduced. The phase composition and structures of the phases have been investigated via PXRD and Rietveld refinements.

Mechanochemical induced phase transformations have been observed by milling of monoclinic  $\beta$ - $\text{Li}_2\text{TiO}_3$ , spinel  $\text{Li}_4\text{Ti}_5\text{O}_{12}$  and spinel  $\text{LiMn}_2\text{O}_4$ . The deployed lithium metal oxides have been prepared from  $\text{Li}_2\text{CO}_3$  and anatase  $\text{TiO}_2$  or  $\text{Mn}_2\text{O}_3$  via simple solid-state reactions. The educts have been ground by hand in an agate mortar and subsequently heated in platinum crucibles at 800 to 900 °C for eight hours. The phases and structure changes that appear after mechanochemical treatment have been investigated via PXRD and Rietveld refinements and in the case of lithium titanium oxides also via  $^6\text{Li}$  solid-state NMR measurements.

### Lithium Titanium Oxides

Cubic  $\alpha$ - $\text{Li}_2\text{TiO}_3$  is formed by milling of  $\text{LiOH}$  and rutile  $\text{TiO}_2$  in a high energy planetary ball mill. Milling experiments with anatase have revealed that the phase transformation of anatase  $\text{TiO}_2$  to the high pressure polymorph and subsequently to rutile takes place before or at the same time as the reaction with  $\text{LiOH}$  to  $\text{Li}_2\text{TiO}_3$ , effectively limiting the reaction rate. It has also been shown that the reaction proceeds faster if WC grinding tools are used instead of  $\text{ZrO}_2$ . This is most probably based on the higher density of WC. Milling speed and milling time were varied to obtain a milling map. The limiting factor for the reaction was the milling speed, since an increased milling time did not produce higher portions of the product phase at lower rotational speeds. The overall amount of produced  $\alpha$ - $\text{Li}_2\text{TiO}_3$  was limited to ca. 70% because the formation of an amorphous phase took place. Crystalline  $\text{Li}_2\text{CO}_3$  occurred as a side product since remaining  $\text{LiOH}$  reacted with  $\text{CO}_2$  from air. It has been shown by coupled TG-IR measurements that the amorphous phase is most likely only composed of  $\text{TiO}_2$ . The observed mass loss matches the mass of  $\text{Li}_2\text{CO}_3$ . The IR spectra of the gas flow are dominated by  $\text{CO}_2$ . Future investigations will have to show if the reaction may be conducted quantitatively by varying the used educts or increasing milling time or speed even further. The former may be achieved by using  $\text{Li}_2\text{O}$  or  $\text{LiOOH}$ , the latter by using a more powerful high energy ball mill.

Milling of monoclinic  $\beta$ - $\text{Li}_2\text{TiO}_3$  in a high energy planetary ball mill leads to a transformation to  $\alpha$ - $\text{Li}_2\text{TiO}_3$  with NaCl structure. Similar to the mechanochemical synthesis, the transformation proceeds faster by using WC tools. The use of  $\text{ZrO}_2$  tools leads to the formation of high amounts of  $\text{Li}_2\text{CO}_3$  and an amorphous background. A nearly complete transformation is already achievable by milling at 600 rpm for only one hour. Milling of spinel  $\text{Li}_4\text{Ti}_5\text{O}_{12}$  also leads to a partial transformation to  $\alpha$ - $\text{Li}_2\text{TiO}_3$ . Prolonged milling however induces a decomposition to  $\text{Li}_2\text{CO}_3$  and an amorphous phase.  $^6\text{Li}$  MAS NMR measurements have shown that a tetrahedral and octahedral coordination environment is found for lithium in the milled products. Lithium in  $\text{Li}_2\text{CO}_3$  is tetrahedrally coordinated, however, a fitting of the NMR spectra with Voigt functions reveals that the area relations of tetrahedral to octahedral coordination do not match the refined  $\text{Li}_2\text{CO}_3$  content from the Rietveld refinement. It has been assumed that the milling process induces a disorder in the form of an occupation of interstitial sites. The structure model for the Rietveld refinement has been expanded to also include a (constrained) occupation of tetrahedral gaps, improving the fit. The effects of milling onto structure of monoclinic  $\beta$ - $\text{Li}_2\text{TiO}_3$  and spinel  $\text{Li}_4\text{Ti}_5\text{O}_{12}$  have also been probed via impedance spectroscopy measurements. It has been found that short milling times increase the conductivity by several orders of magnitude. In contrast, longer milling times reduce the conductivity again. Further combined PXRD and NMR investigations, especially in the region of shorter milling times, may help to understand the process of the phase transformation in more detail. It is not clear whether the occupation of tetrahedral gaps is the cause of the transformation or an effect of it.

## Lithium Manganese Oxides

Nanocrystalline hausmannite  $\text{Mn}_3\text{O}_4$  can be produced by a mechanochemical reaction of  $\text{MnO}$  and  $\text{Mn}_2\text{O}_3$ . In contrast to the mechanochemical synthesis of cubic  $\alpha$ - $\text{Li}_2\text{TiO}_3$ ,  $\text{Mn}_3\text{O}_4$  can be formed quantitatively and without the presence of a larger amount of an amorphous phase. Similar to the synthesis of  $\text{Li}_2\text{TiO}_3$ , milling speed and time have been systematically varied to obtain a milling map.  $\text{Mn}_3\text{O}_4$  is formed even at low rotational speeds and short grinding times, however, a full conversion is only achievable at long milling times and high milling speeds. The mechanochemically formed  $\text{Mn}_3\text{O}_4$  reveals the same lattice parameters as a product formed by a solid-state reaction. The crystallite size is in the range of 14 nm, making the material potentially very interesting for battery applications. The lithium intercalation capability has been screened by chemical lithium intercalation. After one hour at room temperature the nanocrystalline  $\text{Mn}_3\text{O}_4$  reacts with  $\text{BuLi}$  in dry hexane, forming 50% of  $\text{Li}_x\text{Mn}_3\text{O}_4$  with  $x$  close to one. Coarse grained  $\text{Mn}_3\text{O}_4$  from a solid-state reaction does not undergo any reaction at the same conditions. This easy to prepare nanocrystalline material may be well suited to be the base for further investigations as lithium intercalation material. It may be assumed that many more nanocrystalline metal oxides can be prepared by similar mechanochemical methods,

---

allowing to produce nanocrystalline metal oxides that may otherwise be unobtainable or too difficult to prepare.

Milling of pure  $\text{LiMn}_2\text{O}_4$  at harsher conditions results in a decomposition to  $\text{Mn}_2\text{O}_3$  and an amorphous phase. This can be avoided by the addition of 10 wt% phenylphosphonic acid. The phosphonic acid groups form covalent P-O-Mn bonds in the milling process, functionalizing the surface of the formed  $\text{LiMn}_2\text{O}_4$  nanocrystals. This in situ surface functionalization is able to prevent the aforementioned decomposition. The functionalization can be observed by IR spectroscopy measurements. The characteristic P=O double bond and P-OH vibrations are clearly discernible in the raw educt. After the milling process one broad vibration band is observed, indicating a continuum of different bonding states. A complete functionalization is achievable by long milling times at low rotational speeds or already after short milling times if higher rotational speeds are applied. Milling induced in situ surface functionalization of metal oxides has already been established in literature as a simple method to stabilize specific phases. Here it has been shown that the functionalization is also a versatile tool to prevent the decomposition of a phase.

Milling of spinel  $\text{LiMn}_2\text{O}_4$  with phenylphosphonic acid as stabilizer induces several transformation effects. At milder milling conditions an anisotropic reflection broadening is observed and no new reflections are formed. DSC measurements have revealed that the expected low temperature phase transformation to the orthorhombic structure is not present in the milled product. In contrast, coarse grained  $\text{LiMn}_2\text{O}_4$  from a solid-state reaction shows the expected transformation at around 7 °C. As a result, a simple orthorhombic structure has been used to refine the pattern of milled  $\text{LiMn}_2\text{O}_4$ , allowing to treat the anisotropic broadening based on a distribution of lattice parameters. This simple orthorhombic structure has been directly derived from the cubic spinel structure by keeping the atomic positions and refining three independent lattice parameters. To gain a distribution with smaller increments, three fractions of the orthorhombic structure with constrained microstructure and independent lattice parameters have been constructed. Milling of  $\text{LiMn}_2\text{O}_4$  at harsher conditions induces a change of the relative reflection intensities, correlated to the cation occupation. In the ideal spinel structure of  $\text{LiMn}_2\text{O}_4$  all lithium atoms are located on one eighth of the tetrahedra gaps and the manganese atoms on one half of the octahedra gaps. It has been assumed that the milling process induces an occupation comparable to that of a disordered spinel. The structure model has been extended by a constrained refinement of the cation occupation to accommodate the intensity changes. Further milling also induces a transformation to a tetragonal state, similar to the hausmannite  $\text{Mn}_3\text{O}_4$  structure. This phase can also be fitted by the proposed structure model, since two of the lattice parameters adapt the same value, while the third is strongly elongated compared to the initial parameter. It has been assumed that a partial reduction of  $\text{LiMn}_2\text{O}_4$  takes place. The strong Jahn-Teller effect of the formed Mn(III) might cause the strong splitting of the lattice parameters and subsequently be responsible for the tetragonal symmetry. In situ high temperature PXRD measurements have shown that cubic spinel  $\text{LiMn}_2\text{O}_4$  is reformed again in all samples. The transformation temperature

however is highly dependent on the pretreatment, or the structure state which is present in the sample. The orthorhombic  $\text{LiMn}_2\text{O}_4$  obtained by mild milling transforms back to the spinel structure at 500 °C. If the disordered cation state is present a transformation is already evident at 350 °C and the tetragonal state transforms at 250 °C. Since all these changes can be described with the proposed three fraction model, it may be assumed that many milling induced structure changes can be modeled by such Rietveld refinement models. Further investigations may show how such a model performs for different compounds with spinel structure or for different structure types overall.